5-2024

Unraveling the Physics of Quasar Jets Using HST Polarimetry

Devon Clautice
Florida Institute of Technology, dclautice2012@my.fit.edu

Unraveling the Physics of Quasar Jets Using HST Polarimetry

by

Devon Clautice

Master of Science
Space Sciences
Florida Institute of Technology
2016

Bachelor of Science
Physics
University of Central Florida
2010

A dissertation
submitted to the College of Engineering and Science
at Florida Institute of Technology
in partial fulfillment of the requirements
for the degree of

Doctor of Philosophy
in
Space Sciences

Melbourne, Florida
May, 2024

We the undersigned committee
hereby approve the attached dissertation

Unraveling the Physics of Quasar Jets Using HST Polarimetry by Devon Clautice

---

Eric Perlman, Ph.D.
Professor
Aerospace, Physics and Space Sciences
Major Advisor

Roberto Peverati, Ph.D.
Associate Professor
Chemistry and Chemical Engineering

Jean Carlos Perez, Ph.D.
Associate Professor
Aerospace, Physics and Space Sciences

Donald Warren, Ph.D.
Assistant Professor
Aerospace, Physics and Space Sciences

Ratneshwar Jha, Ph.D.
Professor and Department Head
Aerospace, Physics and Space Sciences

Abstract

Title:

Unraveling the Physics of Quasar Jets Using HST Polarimetry

Author:

Devon Clautice

Major Advisor:

Eric Perlman, Ph.D.

We present a multiwavelength study of three high-power FR II (quasar) jets – 3C 273, PKS 0637-752, and 1150+497 – with an emphasis on new high-quality Hubble Space Telescope (*HST*) optical polarimetry and *Chandra* X-ray Observatory imaging. Relativistic jets from active galactic nuclei transport energy and mass from the supermassive black hole's accretion region out to Megaparsec-scale lobes, with effects that feedback into galaxy formation and cluster energetics. We build on recent work which has called into question our fundamental understanding of FR II jet physics, and suggest that highly-efficient particle acceleration must be taking place *in situ* within regions of these large-scale jets, many kiloparsecs away from the central engine. Multiple independent methods of probing the emission of these jets suggest a synchrotron origin for the observed X-ray flux in many cases. We detect significant optical linear polarization in all bright jet knots in our sample, which coincides with the synchrotron prediction. Three of the polarized knots in the 3C 273 are shown to exhibit a second

spectral component of the SED which connects the polarized optical flux to the X-ray flux, lending strong evidence for efficient particle acceleration in these regions resulting in a synchrotron origin for the observed X-rays. All three jets show morphology that is consistent with a spine-sheath structure.

Table of Contents

List of Figures

List of Tables

Abbreviations

ACIS	**A**dvanced **C**CD **I**maging **S**pectrometer
ACS	**A**dvanced **C**amera for **S**urveys
AGN	**A**ctive **G**alactic **N**ucleus/**N**uclei
AIPS	**A**stronomical **I**mage **P**rocessing **S**ystem
CASA	**C**ommon **A**stronomy **S**oftware **A**pplications
CCD	**C**harge **C**oupled **D**evice
CIAO	**C**handra **I**nteractive **A**nalysis of **O**bservations
CTE	**C**harge **T**ransfer **E**fficiency
DN	**D**ata **N**umber
EC/CMB	**E**xternal inverse-**C**ompton Scattering of the **C**osmic **M**icrowave **B**ackground
FITS	**F**lexible **I**mage **T**ransport **S**ystem
FR I/II	**F**anaroff-**R**iley Class **I/II**
HST	**H**ubble **S**pace **T**elescope
IRAF	**I**mage **R**eduction and **A**nalysis **F**acility
NICMOS	**N**ear **I**nfrared **C**amera and **M**ulti-**O**bject **S**pectrometer
PSF	**P**oint **S**pread **F**unction
SED	**S**pectral **E**nergy **D**istribution
SSC	**S**ynchrotron **S**elf-**C**ompton
VLA	**V**ery **L**arge **A**rray
VLBI	**V**ery **L**ong **B**aseline **I**nterferometry
WCS	**W**orld **C**oordinate **S**ystem
WFC3	**W**ide **F**ield **C**amera **3**

Acknowledgements

I wish to thank my parents, Russ and Gloria Clautice, without whom this would not be possible. I wish also to thank Dr. Eric Perlman for being my advisor. And lastly, I wish to thank my friends for their help and support.

These results are based on observations made by the Chandra X-ray Observatory and Hubble Space Telescope. We acknowledge support for this work by the National Aeronautics and Space Administration (NASA) through STScI grants HSTGO-14696.001-A, HSTGO-13764.001-A, and HSTGO-11138.001-A. We also acknowledge support from the National Science Foundation under grant AST-1715607.

Dedication

This dissertation is dedicated to my parents, Russell and Gloria Clautice.

Chapter 1

AGN Jets and Jet Physics

1.1 Introduction

Active galactic nuclei (AGN) are small regions at the core of some galaxies that are characterized by extremely high energy output. Nearly every galaxy is thought to have a supermassive black hole at its core (Boettcher et al., 2012) − a black hole with mass on the order of millions or even billions of solar masses. At any time, the vast majority of these supermassive black holes are quiescent, however a small percentage ($\sim 1\%$) are able to accrete enough matter that they begin to outshine the stars and other sources of electromagnetic radiation in their galaxy. Of this small number of "active" galaxies, about 10% are seen to form relativistic jets (Kellermann et al., 1989) − very powerful and highly-collimated outflows that can emit electromagnetic radiation over a wide range of wavelengths, from radio through gamma rays.

The typical lifetime over which a galaxy experiences its active phase is thought to be $\sim 10^7 - 10^8$ years (Boettcher et al., 2012). Active phases are thought to be caused by the forcing of additional matter into the core region, typically due to an interaction or collision between galaxies.

This dissertation is a multiwavelength study of three high-power quasar jets, with an emphasis on new high-SNR *HST* optical polarimetry and *Chandra* X-ray imaging. These jets all have emission regions where the X-ray flux cannot be connected to the low-energy radio emission by a single power-law. A growing body of evidence suggests the presence of efficient *in situ* particle acceleration within the emission regions of these large scale FR II jets. Though there now exists several independent methods to study the nature of this high-energy spectral component, optical polarimetry remains a unique and powerful tool to study the structure of magnetic fields within these particle-accelerating regions. It also provides an unambiguous diagnostic, where synchrotron emission is expected to be significantly polarized while up-scattered IC/CMB emission is expected to be unpolarized.

A preliminary version of some of the work presented in this dissertation was previously published in Perlman et al. (2020). Portions of the text in this dissertation were also used in my Master's thesis entitled "The Kinematics and X-ray Emission Mechanism of the Large-Scale Jet of 3C 111," where observational or analytical techniques overlap.

1.2 Relativistic Jets from AGN

The first observation of an AGN jet was from the galaxy M87 in 1918 (Curtis, 1918), described as "a curious straight ray." Over the following decades and thanks to improvements in telescope technology, radio jets were detected in more and more galaxies. These jets are thought to be propelled by the supermassive black hole in a way that is not well-understood (Meier, 2011) (discussed in §1.4). Whatever the exact mechanism, the jets are propelled at tremendous speeds (nearly the speed of light, c) outward from the core and are able to carry energy and momentum out to distances of a Megaparsec

or more. These sources are among the most energetic phenomena in the Universe, with a typical jet radiative power of $10^{42} - 10^{47}$ erg s^{-1} (Blandford et al., 2019).

Early ground-based optical observations were able to detect optical emission in a handful of these jets, but it was not until *HST* came online in 1990 that the true extent of optical jet emission was first seen. Likewise for X-ray observations, it was only once *Chandra* was launched in 1999 that X-ray emission became observable with high-resolution imaging. *Chandra*'s first calibration observation was of the quasar PKS 0637−752, which turned out to have a bright X-ray jet flowing from its core (Schwartz et al., 2000).

Chandra has allowed for easier detection of optical jets as well, since optical knots can be difficult to detect without knowing they are there due to the presence of many background sources. To date, at least 150 X-ray jets have been identified[1] while ~ 45 jets have confirmed optical emission (Boettcher et al., 2012, p. 155).

Lister & Marscher (1997) estimate that there must be a parent population of $\gtrsim$10 million jets in the observable Universe, though due to relativistic effects (discussed in §1.6), not all of them are detectable.

AGN jets can be broken down into categories based on observational differences. One such classification is the Fanaroff-Riley (FR) scheme − FR I and FR II (Fanaroff & Riley, 1974), shown in Figure 1.1. FR I jets are less powerful than FR II jets, with the division happening at $L_{1.4\ \mathrm{GHz}} \sim 5 \times 10^{25}$ W Hz^{-1}, and have several distinctions that will be highlighted in §1.5. Depending on their orientation and bulk velocity, either one or both of the approaching and receding jets will be seen.

---

[1] `http://hea-www.harvard.edu/XJET/`

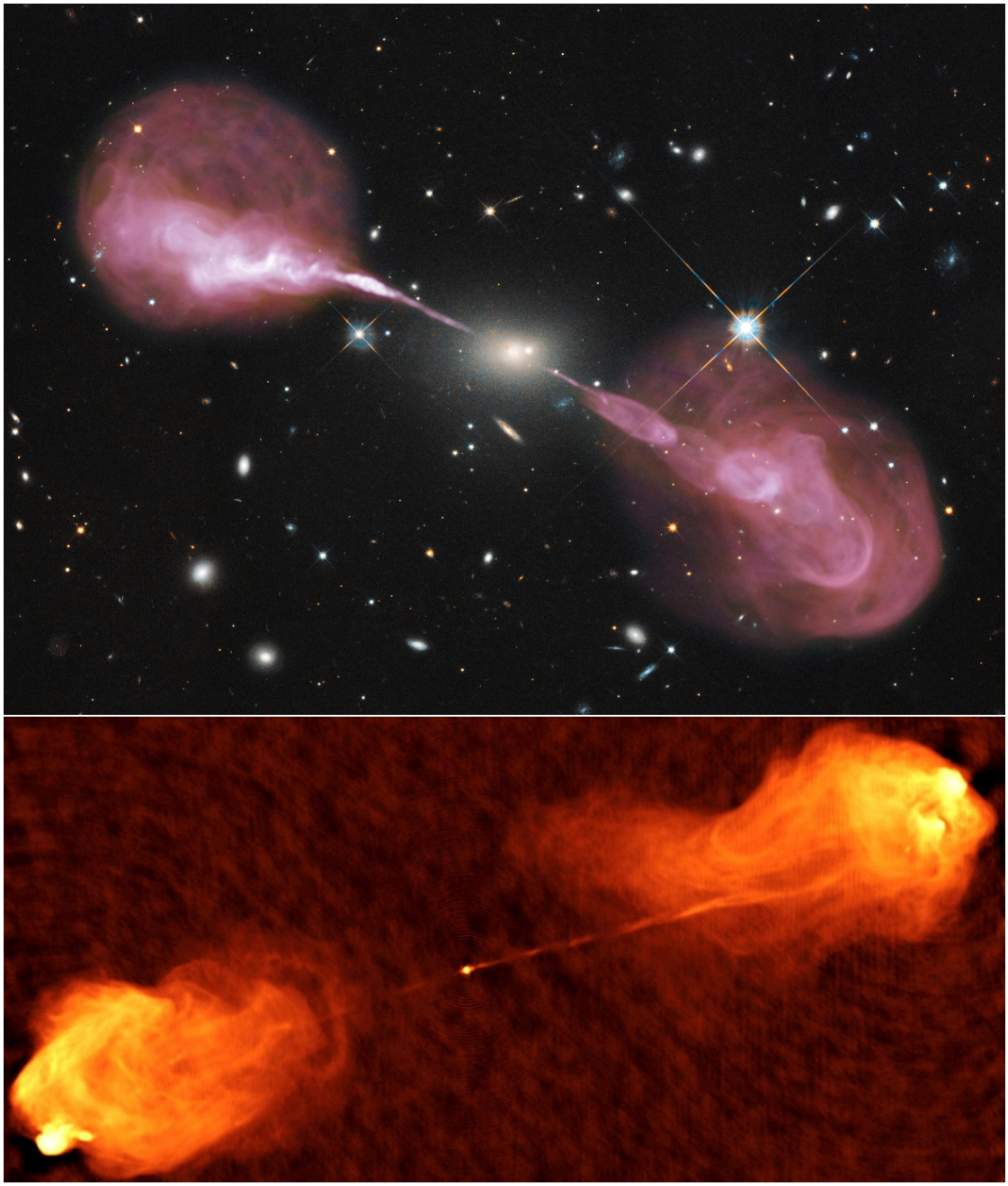

Figure 1.1: A visual example of FR I and II jets. *Top*: Radio (pink) and infrared composite image of the FR I jet of Hercules A. *Bottom*: Radio image of the FR II jet of Cygnus A. Note the presence of bright hotspots in the FR II case, where the still-relativistic jets collide with the intergalactic medium. Source: NRAO.

1.3 Disk Accretion

The process by which matter falls into such a black hole is known as accretion. The matter supply can come from either the interstellar medium (ISM) or from stars that become tidally disrupted near the black hole. Infalling matter will have a nonzero angular momentum; the centrifugal force caused by the rotation around the black hole causes the matter to form into a disk or torus structure (Figure 1.2).

To continue falling in, the matter in the accretion disk must somehow lose some of its angular momentum. Theoretically, friction caused by the molecular viscosity of the accreting "fluid" can allow for angular momentum to be transferred outward along the disk, allowing matter on the interior of the disk to fall further in. However, this friction is too small to be the main mechanism of angular momentum transfer in the disk. It was postulated by Shakura & Sunyaev (1973) that a source of hydrodynamic turbulence could be responsible for increasing the viscosity of the fluid, thereby increasing the angular momentum transfer and allowing matter in the inner accretion disk to continue falling into the black hole. Balbus & Hawley (1991) showed that the presence of even a very weak magnetic field can induce such a turbulence, leading to an instability in the disk. This effect is known as the magnetorotational instability (MRI) and is thought to be important in many astrophysical systems which involve accretion disks, such as X-ray binaries (e.g., Krtička et al. 2015).

The nature of the magnetic fields present in accretion disks is still an open question, though it is largely agreed that they play an important role. It is possible that such disks exhibit a dynamo effect that generates its own magnetic field, or that the magnetic field present in the ISM is dragged along with the infalling matter as it spirals into a disk.

An accretion disk can be either "thin" or "thick" depending on how efficiently the

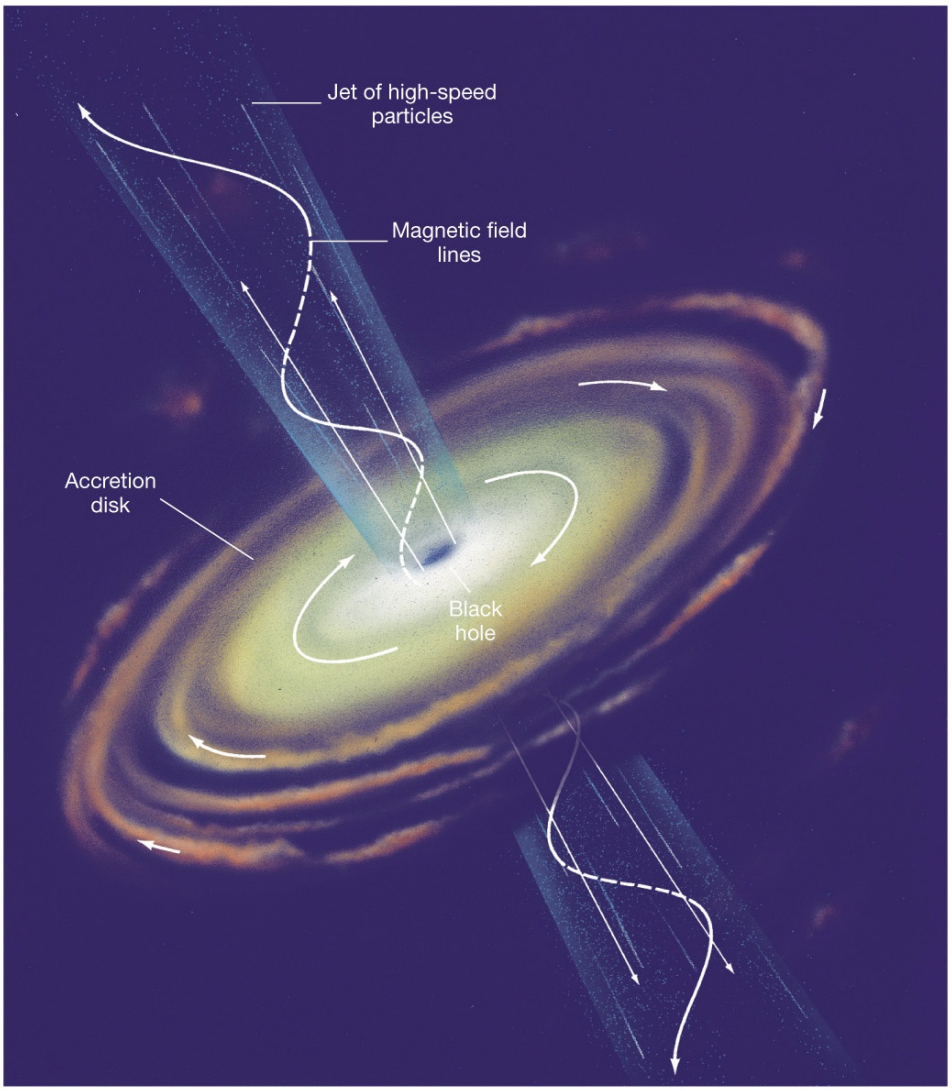

Figure 1.2: Illustration of an AGN that is launching a relativistic jet. Credit: Pearson Education, Inc.

disk matter is being cooled (e.g., Shakura & Sunyaev 1973, Narayan & Quataert 2005). If the radiative cooling of the plasma is very efficient, the disk will be geometrically thin; otherwise, it will be thick or torus-shaped. In general, a higher mass accretion rate leads to an increase in disk thickness. The Eddington luminosity (or Eddington limit) is the theoretical maximum luminosity possible, when the gravitational force

inward is equal to the radiation pressure outward; this occurs at the corresponding Eddington (mass) accretion rate (Boettcher et al., 2012). When the mass accretion rate exceeds this critical value, the radiation pressure increases above the Eddington limit (becoming so-called super-Eddington). The increased radiation pressure serves to overpower the inward gravitational force and has a net effect of slowing the rate of accretion. This self-regulating process serves to keep the mass accretion rate at or below the Eddington rate except for relatively short periods.

The fraction of jetted AGN has been observed to increase with cosmological redshift (e.g., Jiang et al. 2007). This is thought to be due to the nature of the black-hole-accretion-disk systems that are capable of launching jets, though the possibilities are largely speculative. One such possibility is that a spinning (Kerr) black hole is required to launch a jet, and that the spin must be close to maximal (e.g., Meier 1999). Prograde accretion can increase the spin of a black hole to its maximum in a timescale of $\sim M/\dot{M}$ (Tout & Pringle, 1996), while retrograde accretion decreases black hole spin on an even shorter timescale (Moderski et al., 1998). Given that accretion can randomly be prograde or retrograde, this would lead to an overall effect where, over time, most black holes become slow rotators and incapable of launching jets. Black hole mergers (likely during galactic mergers) could also spin up the black hole, and such mergers are thought to be much more common in the early Universe.

Another intriguing possibility is that jets can only be launched from retrograde accretion disk systems, as described in Wilson & Colbert (1995). Accretion disk systems are thought to have a "plunging region" where material that falls within the last stable circular orbit will quickly fall into the accreting black hole. Depending on the density of matter in this plunging region at any given time, a large magnetic flux can accumulate. This effect is thought to be strongest for a retrograde disk, and would give such a disk the strongest possible magnetic flux with which to launch a jet (discussed further

in §1.4). Over time, retrograde disk accretion will spin down its black hole until it becomes prograde. This could explain the rarity of jetted AGN, requiring a rare event such as a galactic merger to cause retrograde accretion on a prograde supermassive black hole system. This model is supported by the observation of several supermassive black holes exhibiting rapid prograde spin but no jets (e.g., Brenneman & Reynolds 2006).

1.4 Jet Formation

It is thought that the supermassive black hole and its associated accretion disk are responsible for accelerating a jet outward from the core. Very Long Baseline Interferometry (VLBI) observations of M87 have traced the jet to very near the black hole nucleus (Krichbaum et al., 2006; Lu et al., 2023) and observations by the Event Horizon Telescope Collaboration have imaged and resolved the SMBH−accretion-disk system (Event Horizon Telescope Collaboration et al., 2019, 2021). Figure 1.3 shows the inner regions of the two-sided jets of Cygnus A using VLBI.

The gravitational potential energy of the infalling matter and the spinning black hole are the only obvious sources of power present that could serve as an engine for the jet. Also important are the strong magnetic fields produced by the accretion disk. It is not known whether the accretion disk can generate its own magnetic field *in situ* via magnetic dynamo or whether gas from the ISM carries the magnetic fields as it accretes. The exact nature of jet launching is still an open and complex question (e.g., Koide & Arai 2008; Punsly & Coroniti 1990a,b).

The two predominant models for relativistic jet launching are those of Blandford & Payne (1982) and Blandford & Znajek (1977). Both models rely on magnetic launching via the MHD Penrose process. The chief difference between them lies in the energy

reservoir used to launch the jet.

The model of Blandford & Znajek (1977) relies on the extraction of energy and angular momentum from the black hole itself, with magnetic flux from the accretion disk being "squeezed" into the black hole's ergosphere. A Kerr black hole in the presence of a magnetic field will generate an electric field through general relativistic effects, allowing energy from the black hole to be extracted. In this model, it is primarily electrons and positrons (generated through pair production in the black hole's magnetosphere) which are launched initially, with protons being added from magnetic field lines that intersect the accretion disk or later on externally. The magnetic fields which are anchored in the accretion disk are rapidly rotating around to form a helical shape that serves to tightly collimate the jet (as in Figure 1.2). This is generally accepted to be the "easiest" (in terms of energy efficiency) method for a jet to be launched at ultra-relativistic speed. This model relies on the black hole magnetosphere to be "open" − open field lines allowing for the transfer of angular momentum from the black hole to infinity − as opposed to "closed," where closed field lines can only transfer angular momentum to the accretion disk. "Open" magnetospheres are associated with both rapid prograde black holes and with retrograde black holes. For this mechanism, retrograde black holes are thought to launch the most powerful jets (e.g., Meier 2011).

The model of Blandford & Payne (1982) relies on the presence of magnetic field lines anchored in the disk that are being rapidly dragged to form a helical shape. Perturbations within the disk accelerate matter away from the disk and along the field lines (like beads on a string). The acceleration and collimation of the jet in this model is achieved by the magnetic field energy (Poynting flux) being converted into bulk kinetic energy and the presence of an external medium. This process is more efficient for non-relativistic jets than for relativistic ones, and does not require a spinning black hole.

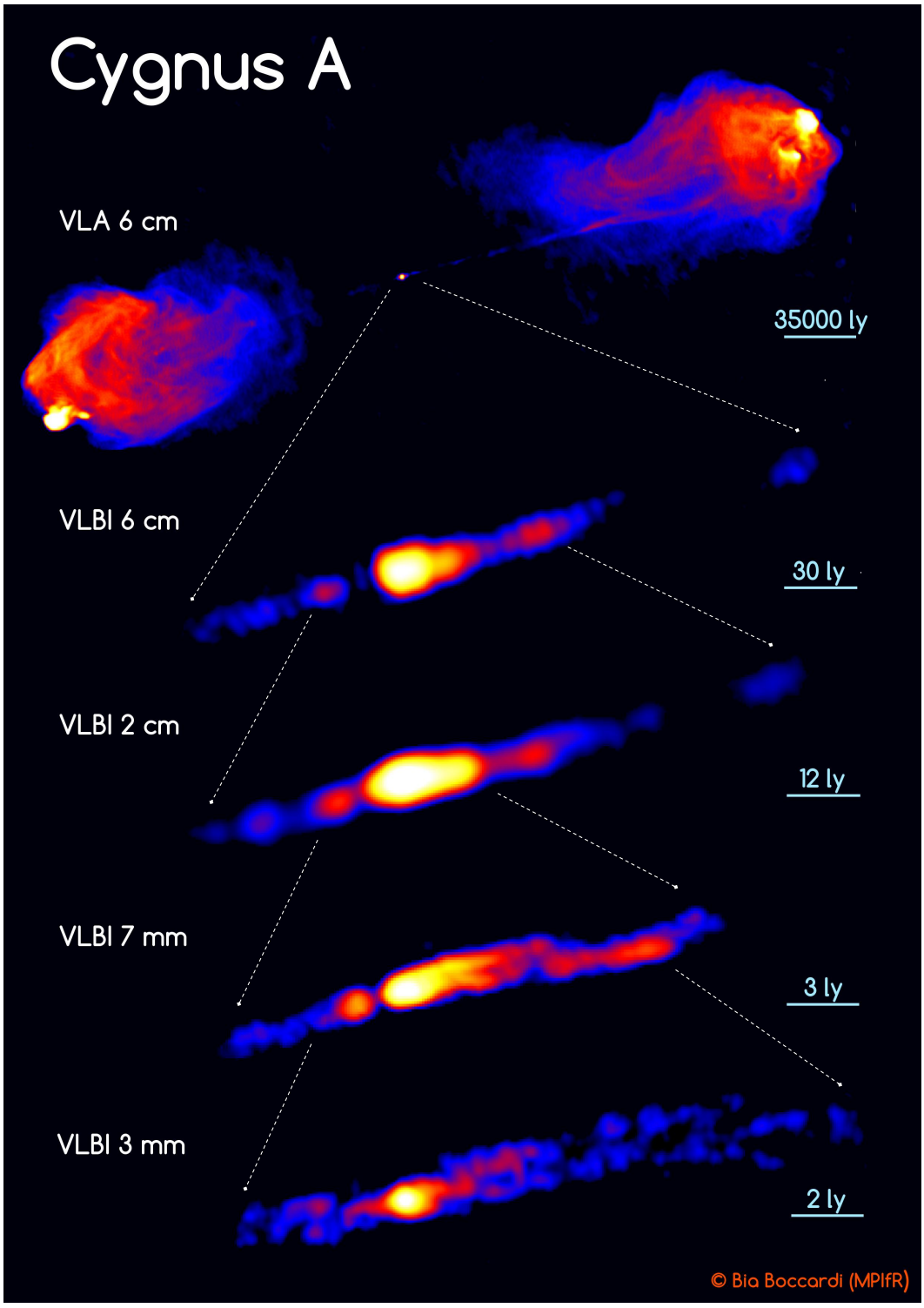

Figure 1.3: The two-sided jets of Cygnus A shown from the pc scale to the kpc scale. Despite being an FR II source, the large viewing angles of the jets allow both to be seen. Taken from Boccardi et al. (2017).

It is possible that both mechanisms work to launch jets that follow the spine-sheath model (discussed in §1.5), where the central spine is powered by the ergosphere and the outer sheath is ejected from the accretion disk (Xie et al., 2012). Figure 1.4 shows a schematic of the main regions of a magnetically-launched AGN jet.

1.5 Structure and Composition

Once the jet is accelerated away from the core, the first structure that is observed comes in the form of blobs of radiating plasma called "knots." Shocks and magnetic reconnection phenomena within the jet are thought to accelerate electrons to relativistic speeds, which then emit electromagnetic radiation in various wavelengths and produce the observed knots (Boettcher et al., 2012). It is these locally-accelerated electrons that produce the emission observed in the IR-optical wavelengths by way of synchrotron and inverse-Compton emission (see §1.7). Knots can be seen on the smallest and largest scales. On the pc scale, a stationary recollimation shock can occur where the pressure of the external medium serves to collimate the jet.

FR I jets exhibit decreasing brightness at greater distances from the core, with the jet terminating in large plumes (Blandford et al., 2019). An FR II jet terminates at a very bright region called a "hotspot" which is surrounded by a large radio lobe. As the jet pushes through the much slower intergalactic medium (IGM), shocks form which accelerate electrons to relativistic speeds and create a bright hotspot; material is pushed away in the collision which form the lobes. Recent work using relativistic magnetohydrodynamic (MHD) simulations point to a kink instability being responsible for the FR dichotomy (Tchekhovskoy & Bromberg, 2016; Mukherjee et al., 2020). Jets above a certain critical power are able to stably push through the ISM in the galaxy's core and terminate at hotspots (FR II), while jets below this critical power become

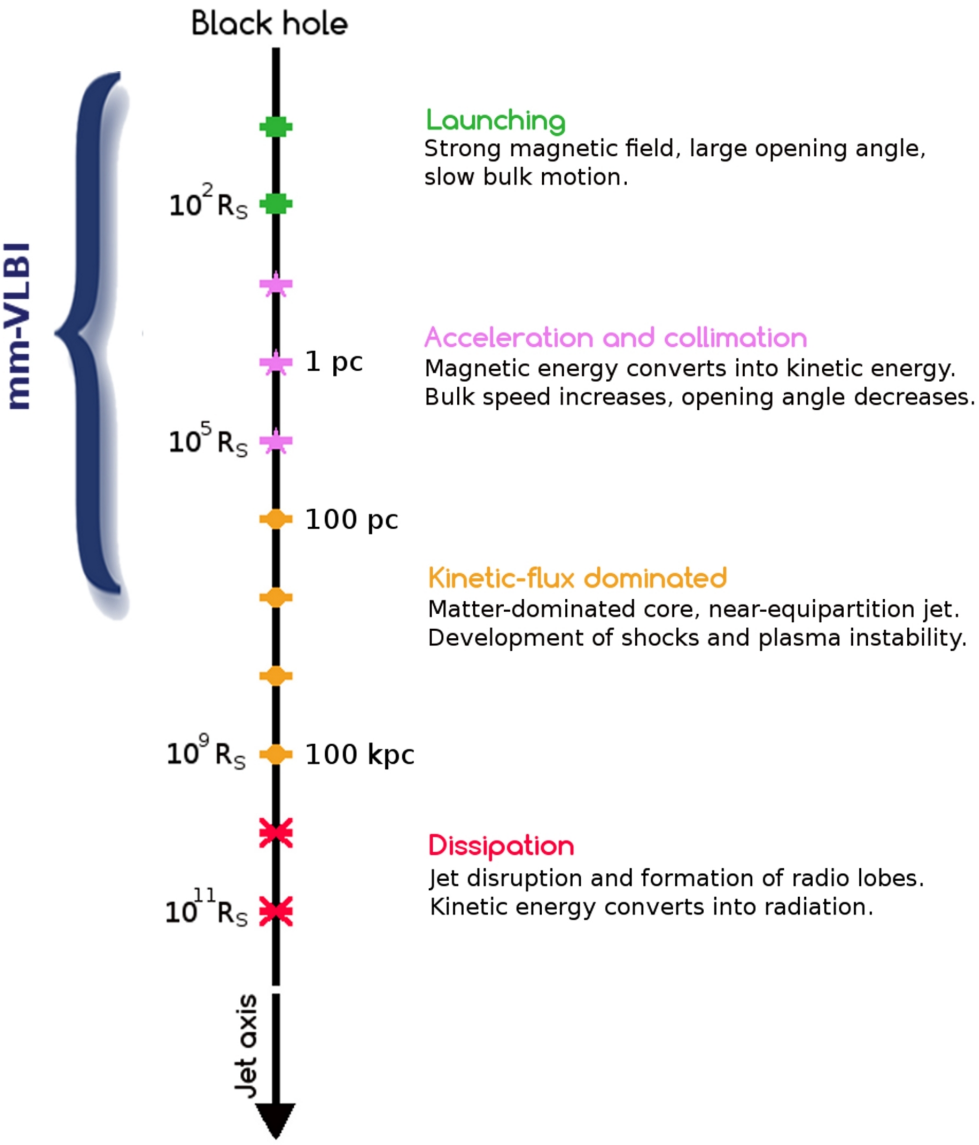

Figure 1.4: Schematic of the main regions of a magnetically-launched AGN jet according to current theory, with distance from central engine going downward. Note that the distance scales involved will depend on the particular jet. Taken from Boccardi et al. (2017).

unstable and lose their integrity, resulting in large plumes of hot plasma (FR I). Thus, these simulation studies find it likely that the relation between the jet's power and the ISM density of the host galaxy dictates which type of jet it will be.

The composition of relativistic jets is largely unknown, though there are several constraints on what it must be (e.g., Georganopoulos et al. 2005, Sikora et al. 2020). Firstly is the fact that jets extend over such massive scales, which rules out high-energy electrons as being the main source of energy transportation − such electrons would lose their energy long before reaching the hotspot (Harris & Krawczynski, 2007). In knots and hotspots, energy is transferred from the bulk composition of the jet into a population of the plasma; the emission that we observe from jets is due to the relativistic electrons that have been accelerated in these regions.

The possible candidates for the carrier of the bulk energy of the jet are thought to be: cold electrons/positrons, cold or hot protons, and Poynting flux (energy carried by electromagnetic fields) (e.g., Perucho & Martí 2007). While attempts have been made to determine which of these is dominant in jets, the ionized nature of the jet's composition makes it difficult to determine (Georganopoulos et al., 2005) − each attempt is fraught with assumptions and arguments that are contentious.

1.5.1 Spine-Sheath Model

There is still a large gap in our understanding of how jets can remain highly collimated on the kpc scale. One popular explanation is the "spine-sheath" model (Sol et al., 1989), where the structure of a jet has two components: a central spine that is relativistic and an outer sheath that is moving slower. A spine-sheath jet is thought to be stabilized from effects that would otherwise disrupt the collimation of the jet over large scales.

Figure 1.5 shows a basic schematic of a spine-sheath structure within a jet, though it is important to note that there are many proposed spine-sheath models with varying

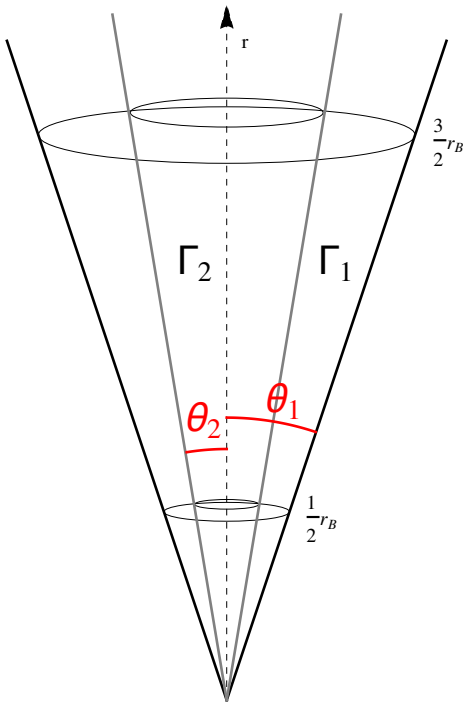

Figure 1.5: Schematic of a spine-sheath jet structure, where the inner spine is expected to be moving faster than the outer sheath (i.e. $\Gamma_2 > \Gamma_1$). Figure from Sikora et al. (2016).

details (such as where within the jet the particle acceleration takes place).

Radio observations of many jets, both FR I and FR II, have exhibited limb-brightening on the pc scale, with a stark example being given by VLBI observations of the M87 jet (Kovalev et al., 2007; Kim et al., 2018). The jet of BL Lac object Markarian 501 provides another significant example of limb-brightening of the radio jet emission (Giroletti et al., 2008). One possible explanation for the observed radio limb-brightening is due to a highly relativistic spine from which emission is de-boosted to a much higher degree than the sheath emission. Kim et al. (2018) calculated the necessary speed of the pc-scale spine of the M87 jet to be $\Gamma_{\rm spine} \sim 13 - 17$ for a viewing angle of 18°. They find such a large bulk Lorentz factor to be unlikely at such a small distance from the core ($70 - 140$ $R_{\rm sch}$), well before the recollimation shock re-

gion. Instead, they favor a model where the spine and sheath exhibit not just velocity differences, but also possible differences in the jet composition and/or magnetic field strength, possibly owing to different launching points for each layer (with the material from the spine coming from the SMBH ergosphere and the sheath material coming from the inner accretion disk).

M87 also provides strong evidence for the spine-sheath structure in FR I jets on the large scale. Perlman et al. (2001) mapped the optical spectral index and radio-to-optical spectral index along the entire length of the M87 jet and compared it to the observed optical flux. They found a strong anti-correlation between optical spectral index and optical flux, and later in Perlman & Wilson (2005) favor a model of continuous injection of particles into the particle acceleration zones within the spine where the magnetic field is chaotic, whereas the sheath has a more uniform magnetic field. The three dimensional nature of a stratified jet makes it difficult to determine which layer from which we are seeing emission at a given wavelength, though in such a model it is expected that we would see optical and/or X-ray knots that are narrower than their radio counterparts. This has been observed in many jets including M87, most recently in Avachat et al. (2016).

The jet of 3C 273 also has been shown to have X-ray knots that are narrower than in the radio (Marchenko et al., 2017). Figure 1.6 shows the deconvolved *Chandra* X-ray flux of the jet overlaid with that of the 8.4 GHz VLA radio image. Particularly in the region of the jet between Knots B2 and H3, the X-ray jet is shown to be significantly narrower than in the radio. This has been interpreted as evidence of a spine-sheath model where particle acceleration is taking place in a chaotic spine region, just as discussed for M87. Another possibility is that the particle acceleration is taking place along a shear boundary between the spine and sheath layers (i.e. along the surface area of the spine/sheath boundary layer).

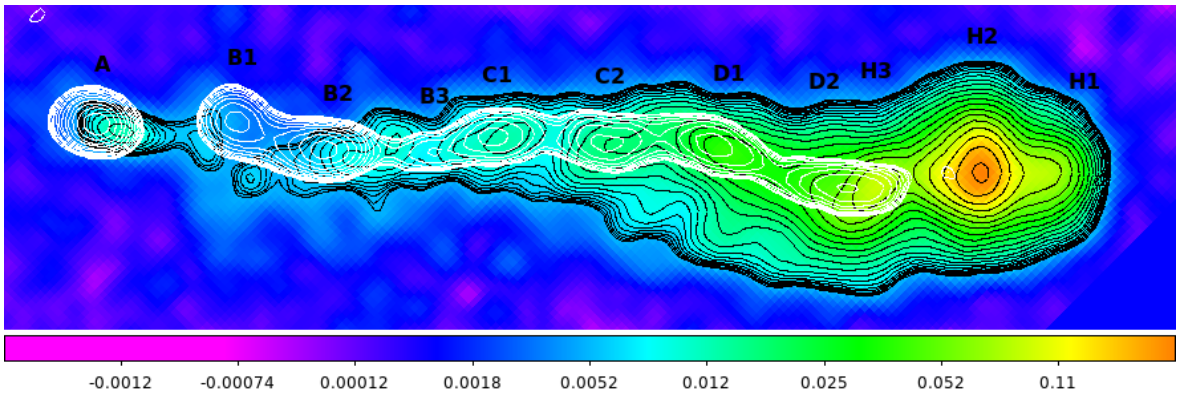

Figure 1.6: 8.4 GHz VLA (radio) color image and black contours of the 3C 273 jet, with *Chandra* X-ray contours overlaid in white. The X-ray flux has been deconvolved using the *Chandra* PSF in an attempt to show the true size of the X-ray jet. One possible interpretation is that the radio emission is emitted from the sheath and spine, while the much narrower X-ray emission is emitted from the spine or possibly from a shear layer between the spine and sheath. Figure from Marchenko et al. (2017).

1.6 Relativistic Effects

AGN jets can have bulk Lorentz factors of $\Gamma > 10$ on the parsec scale (Lister et al., 2009, 2019) and can remain relativistic out to their kiloparsec-scale hotspots (Longair & Riley, 1979). Special relativity is thus important on both the small and large scales. On the parsec scale, this can cause jet knots to appear to move faster than the speed of light. On the large (kpc) scale, on which this project is focused, many relativistic effects are important.

1.6.1 Beaming and Boosting

Foremost is the effect of relativistic beaming. A region of the jet that is moving at relativistic speeds, assuming it emits photons isotropically in its rest frame, will have half of all the photons produced beamed into a narrow cone of opening angle $\theta = 1/\Gamma$ in the observer's reference frame (Figure 1.7). This has a large effect on the observed flux of the emitting region, making it very dependent on the angle between the jet's

propagation and the observer's line of sight. For an approaching jet moving at speed v, this has the effect of increasing the observed flux and frequency of the photons. A receding jet is likewise de-boosted and less easy to detect. An emitted photon's energy will be boosted as

$$E^{\rm rec} = \delta E^{\rm em}, \tag{1.1}$$

where ""rec" (received) denotes the stationary observer's frame, "em" (emitted) denotes the comoving frame of the emission region, and the Doppler factor is

$$\delta \equiv \frac{1}{\Gamma(1 - \beta_\Gamma \cos\theta)}. \tag{1.2}$$

Here, the bulk Lorentz factor $\Gamma = 1/\sqrt{1-\beta_\Gamma^2}$, $\beta_\Gamma = v/c$, and θ is the viewing angle – the angle between the jet and the line-of-sight of the observer in the observer's reference frame. Since the photon energy is related to its frequency by $E_{\rm ph} = h\nu$, it follows that the frequency is similarly boosted, such that $\nu^{\rm rec} = \delta\nu^{\rm em}$. Since the inverse of frequency is a time interval, it is also apparent that $\Delta t^{\rm rec} = \delta^{-1}\Delta t^{\rm em}$.

The effects of Doppler boosting compound when considering the energy flux. When comparing emission at $\nu^{\rm em}$ in the "em" frame and $\nu^{\rm rec}$ in the "rec" frame, the energy flux is boosted by a factor of δ^3, as follows from:

$$F^{\rm rec}_{\nu^{\rm rec}} = F^{\rm em}_{\nu^{\rm em}} \frac{\nu^{\rm rec}}{\nu^{\rm em}} \frac{{\rm d}\nu^{\rm em}}{{\rm d}\nu^{\rm rec}} \frac{{\rm d}\Omega^{\rm em}}{{\rm d}\Omega^{\rm rec}} \frac{{\rm dt}^{\rm em}}{{\rm dt}^{\rm rec}} = F^{\rm em}_{\nu^{\rm em}}(\delta^2)(\delta), \tag{1.3}$$

following cancellation of the ν terms (e.g., Boettcher et al. 2012).

However, when comparing the flux emitted at $\nu^{\rm rec}$ in both frames, we have

$$F^{\rm rec}_{\nu^{\rm rec}} = F^{\rm em}_{\nu^{\rm rec}} \delta^{3+\alpha}, \tag{1.4}$$

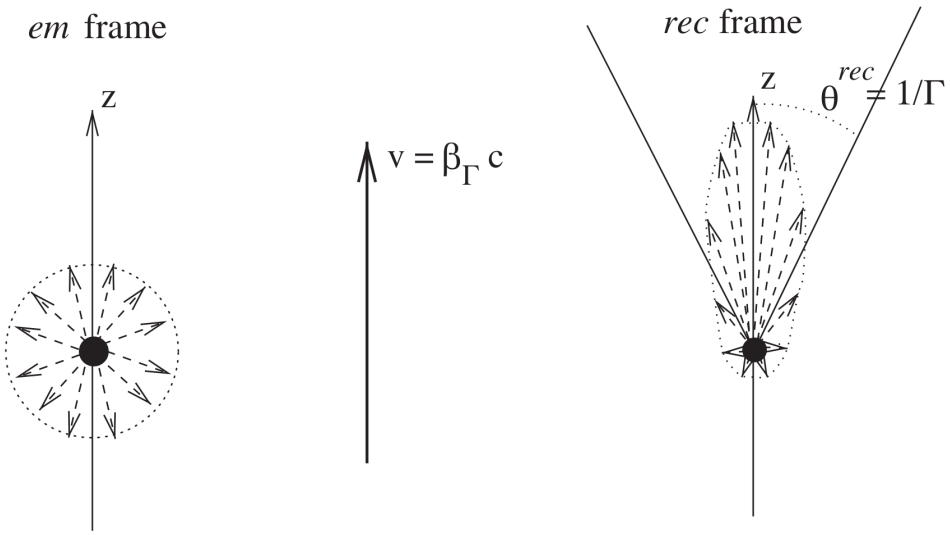

Figure 1.7: Light emitted isotropically in the comoving ("em") frame of the emission region is beamed in the direction of relativistic motion in the observer's ("rec") frame. From Boettcher et al. (2012).

where α is the spectral index. This is illustrated in Figure 1.8.

Importantly, the effects of Doppler boosting do not alter the spectral index α of a power law ($F_\nu \propto \nu^{-\alpha}$). These effects, combined with others such as length contraction and time dilation, make it so that jet properties vary greatly with the viewing angle to the observer.

1.6.2 Superluminal Motion

Another peculiar effect of the relativistic motion of jets is the appearance, in some cases, of superluminal motion − that the proper motion of jet material is faster than the speed of light. Very high-resolution radio observations (e.g., VLBI) on the parsec scale allow for the tracking of jet knots over time. These knots can sometimes be moving with apparent speeds as high as $\beta_{\perp,app} \sim 50$ (Lister et al., 2009, 2019). This is due to the fact that we observe the projection of a jet onto the 2D plane of the sky

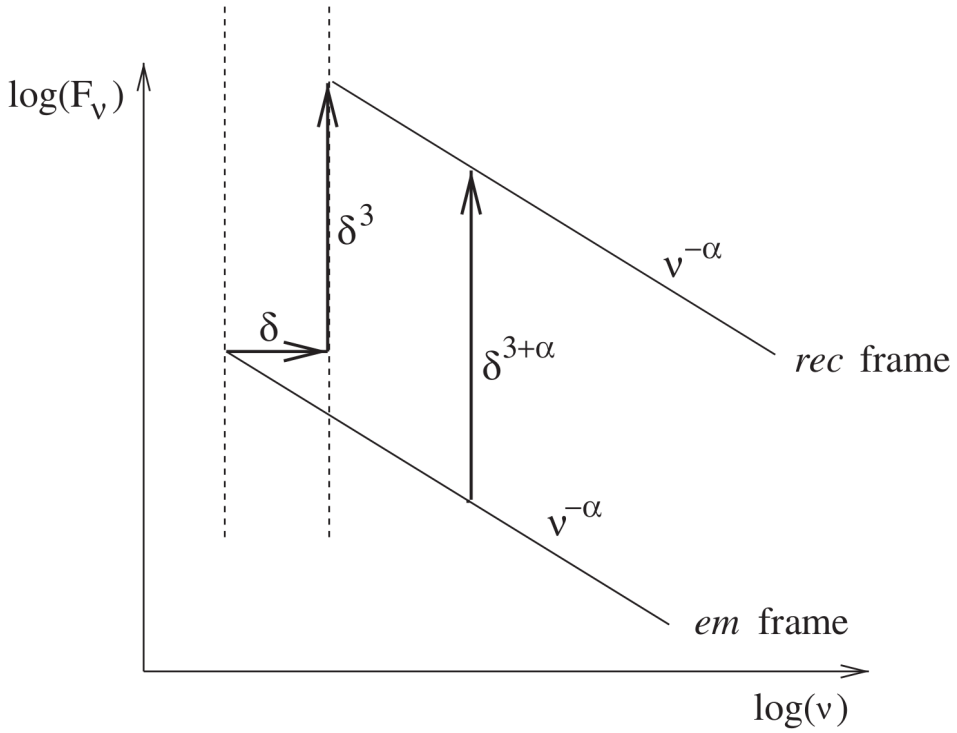

Figure 1.8: Illustration of the effects of relativistic Doppler boosting on a power law spectrum. From Boettcher et al. (2012).

(Rees, 1966). This effect is important because it allows one to constrain both the bulk Lorentz factor of the jet and the viewing angle.

In practice, it is the apparent motion (parameter μ), typically in units of milliarcseconds (mas) per year, that is measured directly from the proper motion of a parsec-scale jet component. From this, the apparent speed of the component $\beta_{\perp,\mathrm{app}}$ can be found by knowing the angular size distance $D_\mathrm{A} = D_\mathrm{L}/(1+z)^2$, where D_L is the luminosity distance[2] to the AGN and z is its cosmological redshift, such that $\beta_{\perp,\mathrm{app}} = \mu D_\mathrm{A}/c$. The redshift (and therefore the luminosity distance) of an AGN can usually be measured

[2] `http://www.astro.ucla.edu/~wright/cosmo_02.htm`

using the Doppler shift of emission lines ($z = \nu_{\rm em}/\nu_{\rm obs} - 1$).

Figure 1.9(a) shows a schematic of the geometry of a jet emission region at two separate times of observation. In the rest frame of the AGN, the knot has moved length $l = v\Delta t$ in a time interval Δt. This translates to a projected distance of $s = l \sin\theta = v\Delta t \sin\theta$. The light emitted from the knot at point A (closer to the AGN) will necessarily take longer to reach the observer than light emitted at point B, due to having to travel an added distance of $x = l\cos\theta$. Taking this into account, the observed time interval between points A and B becomes $\Delta t_{\rm obs} = \Delta t - x/c = \Delta t(1 - \beta_\Gamma \cos\theta)$ rather than simply Δt. The apparent velocity of the knot is then

$$\beta_{\perp,\rm app} = \frac{s}{c\Delta t_{\rm obs}} = \frac{\beta_\Gamma \sin\theta}{(1 - \beta_\Gamma \cos\theta)}. \tag{1.5}$$

For a given value of Γ, this relation can be used to determine the angle at which the apparent velocity is maximized – this superluminal angle is where $\cos\theta_{\rm sl} = \beta_\Gamma$. At this angle, $\sin\theta_{\rm sl} = \sqrt{1 - \cos^2\theta_{\rm sl}} = \sqrt{1 - \beta_\Gamma^2} = 1/\Gamma$. Therefore,

$$\beta_{\perp,\rm app}(\theta_{\rm sl}) = \frac{\beta_\Gamma}{\Gamma(1 - \beta_\Gamma^2)} = \Gamma\beta_\Gamma = \sqrt{\Gamma^2 - 1}, \tag{1.6}$$

showing the maximum apparent velocity possible for a given value of Γ. This can then be used to constrain Γ based on the observed apparent velocity, such that

$$\Gamma \geq \sqrt{\beta_{\perp,\rm app}^2 + 1}. \tag{1.7}$$

A maximum value for the viewing angle $\theta_{\rm max}$ can be found using (1.5) by taking the limit where $\Gamma \to \infty$ and $\beta_\Gamma \to 1$, resulting in $\beta_{\perp,\rm app}^{\rm max}(\theta) = \sin\theta/(1 - \cos\theta)$. Rearranging

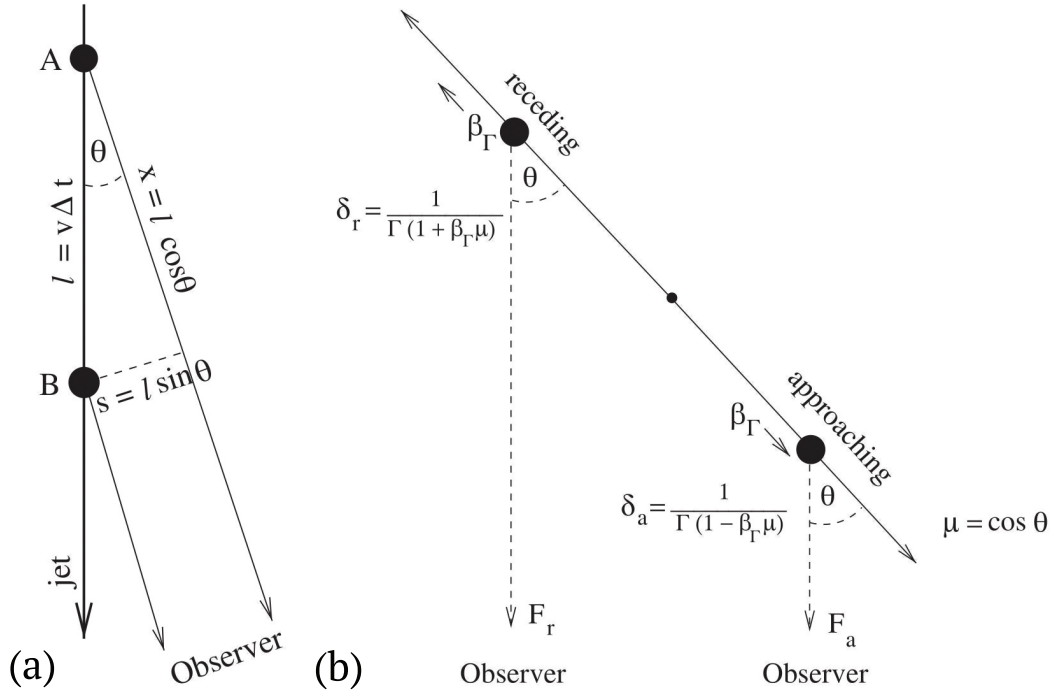

Figure 1.9: (a) Geometry of a jet knot which leads to apparent superluminal motion. (b) Geometry of a two-sided jet. Adapted from Boettcher et al. (2012).

this and using the observed apparent velocity gives

$$\cos\,\theta_{\rm max} = \frac{\beta_{\perp,\rm app}^2 - 1}{\beta_{\perp,\rm app}^2 + 1}. \tag{1.8}$$

Thus, the observed apparent superluminal velocity serves as a powerful tool for constraining the jet's bulk Lorentz factor and viewing angle.

The MOJAVE project has observed the apparent speed of hundreds of jets on the parsec scale using VLBI (Lister et al., 2009; Homan et al., 2015; Lister et al., 2019). They show that the majority of observed features within the first $\sim$ 100 pc are superluminal and accelerating. The maximum observed speed of $\sim 50c$ implies that jets can be highly relativistic on the parsec scale. In the case of the quasar jet 3C 273, they observe a maximum speed of $\sim 15c$. Observations of large-scale jets on

kiloparsec scales have shown less relativistic speeds – in the case of 3C 273, a recent proper motion study showed an apparent speed of $\lesssim 1c$, corresponding to $\Gamma < 2.9$ assuming the jet either maintains the same speed or decelerates downstream from the first bright optical knot (Meyer et al., 2016). Some powerful FR II jets have been shown to be relativistic out to their terminal hotspots, with bulk Lorentz factors of $\Gamma \sim 2 - 3$ (Georganopoulos & Kazanas, 2003). Thus it seems apparent that quasar jets decelerate somewhere between the pc and kpc scale, and then maintain a mildly relativistic speed thereafter.

1.6.3 Two-Sided Jets

In some cases, both the jet and counter-jet are detected emanating from an AGN (Figure 1.9b). This is usually when the viewing angle is relatively large, such that the counter-jet is not de-boosted enough to put its flux below the detection limit of our instruments. The flux ratio between components in the jet and counter-jet can be used to constrain the velocity and viewing angle of the jet. Doing so, however, relies on the assumptions that the components in each side of the jet are emitting the same luminosity isotropically as each other, that each component is moving at the same velocity, and that the jet and counter-jet are 180° apart. This method can be applied even on large scales, where apparent motion is not superluminal or even detected, including all the way out to the hotspots. However, the reliability of the necessary assumptions decreases at large distances where many kpc-scale jets exhibit significant bends. Additionally, the light emitted by the receding component may take many thousands of years longer to reach the observer than light from the approaching component, and so the stage of the development that we observe in each may not be the same.

Due to the high amount of beaming associated with many FR II jets (as discussed in

§1.6.1), it is common for only the approaching jet to be detectable, or for the receding jet to appear much fainter. Figure 1.3 shows the two-sided jets of Cygnus A. Despite being a high-powered FR II source, the large viewing angle allows both jets to be visible to us. The viewing angle of each jet is estimated to be $\sim 50^\circ - 85^\circ$ (Bartel et al., 1995; Boccardi et al., 2017).

As shown in (1.4), we can use the Doppler factor to determine the amount by which the emitted flux is boosted in the receiving frame. Assuming the flux of the two jet/counter-jet components are equal to F_0, it follows that

$$F_{\mathrm{a,r}} = F_0 \delta_{\mathrm{a,r}}^{3+\alpha}, \tag{1.9}$$

where the "a" and "r" subscripts denote the approaching and receding jet components, respectively. The Doppler factor for each of the components, accounting for the assumed 180° difference in viewing angle, can be expressed as

$$\delta_{\mathrm{a,r}} = \frac{1}{\Gamma(1 \mp \beta_\Gamma \cos\theta)} \tag{1.10}$$

where θ is the viewing angle between the approaching jet and the line-of-sight. The negative and positive signs account for solutions for the approaching and receding jets, respectively. Using these equations to take the flux ratio of the approaching and receding components yields

$$\frac{F_{\mathrm{a}}}{F_{\mathrm{r}}} = \left(\frac{1 + \beta_\Gamma \cos\theta}{1 - \beta_\Gamma \cos\theta}\right)^{3+\alpha}. \tag{1.11}$$

Here the factor of $\delta^{3+\alpha}$ applies for a spherical component moving at relativistic speeds. When considering the hospot flux ratios, a factor of $\delta^{2+\alpha}$ would be used (for a steady state or slow-moving structure). The extra factor of δ comes from the relativistic time

compression. This choice is common when considering hotspots as they are more likely to be slow-moving rather than ultra-relativistic (e.g., Hardcastle et al. 2016).

Another diagnostic that can be used on two-sided jets is that of the arm-length ratio. The distance between the AGN core and the hotspots of the jet and counter-jet, after accounting for the light-travel time difference between the two hotspots, can be used to roughly determine the hotspot advance velocity − the speed at which the hotspots are plowing through the IGM (Ryle & Longair, 1967; Blundell & Alexander, 1994). While this is not a direct diagnostic of the jet's speed, it can be used to roughly constrain a minimum velocity for the jet before decelerating when interacting strongly with the IGM. One would expect the approaching jet to have a larger apparent length than the receding jet provided the viewing angle is sufficiently less than 90°, as it is seen at a later stage of development due to it being closer. The derivation is equivalent to that of the observed time interval in the case of superluminal motion in a jet, but now applied both for approaching and receding jets, such that

$$\Delta t_{\rm obs}^{\rm a,r} = \Delta t(1 \pm \beta_\Gamma \cos\theta). \tag{1.12}$$

The arm-length ratio can then be found by

$$\frac{l_{\rm a}}{l_{\rm r}} = \frac{c\Delta t_{\rm obs}^{\rm a}}{c\Delta t_{\rm obs}^{\rm r}} = \left(\frac{1+\beta_\Gamma \cos\theta}{1-\beta_\Gamma \cos\theta}\right). \tag{1.13}$$

Typical values for the arm length ratio are $\lesssim 1.5$, though they can be larger (e.g., Konar et al. 2008).

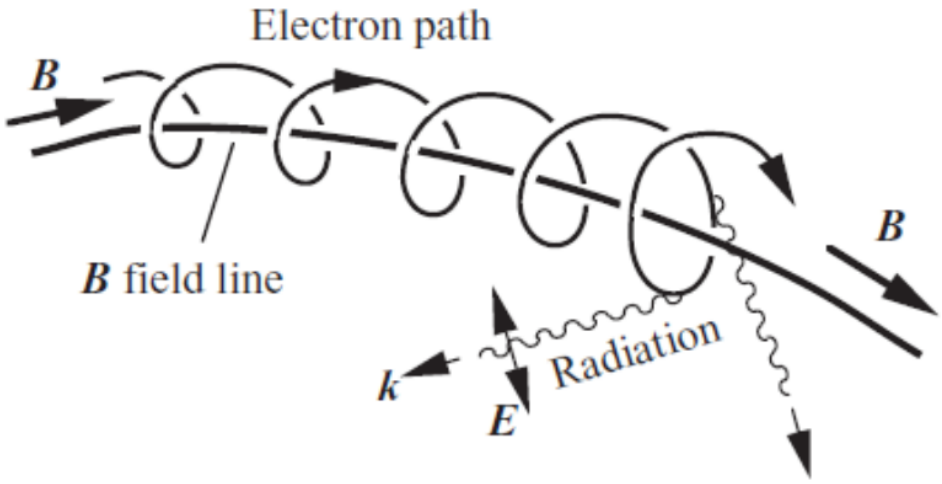

Figure 1.10: Synchrotron radiation produced as an electron spirals along a magnetic field line. From Bradt (2014).

1.7 Non-thermal Radiative Processes

The primary mechanism for electromagnetic radiation in jets is that of synchrotron radiation, however the presence of relativistic electrons in a photon field guarantees that inverse-Compton scattering will occur. Due to the relatively low particle densities in jets ($n \lesssim 10^3$ cm^{-3}), other effects due to particle collisions (e.g., Bremsstrahlung, Coulomb scattering, pair annihilation) are not thought to be important. In this section, Greek letters will correspond to properties of individual particles rather than to the bulk properties of the jet.

1.7.1 Synchrotron Radiation

A charged particle, such as an electron, will emit electromagnetic radiation as it is accelerated in a spiral trajectory by a magnetic field (Figures 1.10 and 1.11). When the particle is moving at relativistic speeds, this is known as synchrotron emission. This process is ubiquitous in nature and present throughout jets. A single particle will

emit a synchrotron spectrum that is strongly peaked near the critical frequency

$$\nu_{\rm c} = \left(\frac{3qB}{4\pi mc}\right)\gamma^2, \tag{1.14}$$

where q is the charge of the particle, B is the magnetic field strength, m is the mass of the particle and the Lorentz factor $\gamma = E/(mc^2)$, with E being the particle's energy. The total emitted power, over all frequencies, is

$$P_{\rm syn} = -\frac{dE}{dt} = \frac{2}{3}r_{\rm e}^2 c\beta_\perp^2\gamma^2 B^2. \tag{1.15}$$

(e.g., Rybicki & Lightman 1979). For an isotropic distribution of particles each with speed β, we can then average over all pitch angles α, where the pitch angle is the angle between the field and velocity, so that

$$< \beta_\perp^2 >= \frac{\beta^2}{4\pi}\int \sin^2\alpha \; d\Omega = \frac{2}{3}\beta^2. \tag{1.16}$$

Plugging this in gives us the total power as

$$P_{\rm syn} = \left(\frac{2}{3}\right)^2 r_{\rm e}^2 c\beta^2\gamma^2 B^2, \tag{1.17}$$

or

$$P_{\rm syn} = \frac{4}{3}\sigma_{\rm T} c\beta^2\gamma^2 u_{\rm B}. \tag{1.18}$$

Here, $\sigma_{\rm T} = 8\pi r_{\rm e}^2/3$ is the Thomson cross section and $u_{\rm B} = B^2/(8\pi)$ is the magnetic energy density.

An important note is that since $r_{\rm e} = e^2/(mc^2)$, we have $P_{\rm syn} \propto m^{-2} \Rightarrow dE/dt \propto -m^{-2}$. Thus, the energy-loss rate is strongly dependent on the mass of the particle. For a proton to suffer the same energy-loss rate as an electron with Lorentz factor $\gamma_{\rm e}$,

its Lorentz factor would need to be $\gamma_{\rm p} \approx (1836)^2 \gamma_{\rm e}$, and its energy would need to be larger by a factor of $(1836)^3$. Therefore, electrons are much more efficient radiators than are protons, with a larger power output and consequently a much shorter radiative lifetime.

A particle distribution $n(\gamma)$ can be defined by

$$n(\gamma) = n_0 \gamma^{-p}, \tag{1.19}$$

where $n(\gamma)$ is the number of particles per unit volume in a Lorentz factor interval $[\gamma, \gamma + d\gamma]$, and p is the power law index of the distribution. The particle energy distribution can be expressed as

$$N(E)dE = CE^{-p}dE \tag{1.20}$$

for an energy range $E_1 < E < E_2$. The power law index p of the particle spectrum is related to the power law index of the photon spectrum by

$$P_{\rm tot}(\nu) = \int \left(-\frac{dE}{dt}\right) N(E)dE \propto \nu^{-(p-1)/2}, \tag{1.21}$$

such that the spectral index $\alpha_{\rm syn}$ is related to the particle distribution index p by

$$\alpha_{\rm syn} = \frac{p-1}{2}. \tag{1.22}$$

The synchrotron emission coefficient, for a given particle distribution $n(\gamma)$, can be stated as

$$j_\nu = \frac{1}{4\pi} \int_1^\infty d\gamma \; n(\gamma) \; P_\nu(\gamma). \tag{1.23}$$

In the observer's frame, accounting for all the various relativistic aberrations, the

radiative power per unit frequency of synchrotron emission from a particle will be

$$P_{\rm syn}(x) = \frac{\sqrt{3}q^3 B}{mc^2} \sin\,\alpha\; F(x), \tag{1.24}$$

where $x = \frac{\nu}{\nu_{\rm c}}$. Rybicki & Lightman (1979) provides a full derivation, however the proportionality of $F(x)$ can be simplified to

$$F(x) \propto \begin{cases} x^{1/3} & \text{for } x \ll 1 \\ x^{1/2} e^{-x} & \text{for } x \gg 1 \end{cases} \tag{1.25}$$

(e.g., Boettcher et al. 2012).

1.7.2 Inverse-Compton Scattering

Inverse-Compton scattering is an interaction between a relativistic particle and a photon in which the particle imparts some of its energy into the photon, increasing its energy/frequency. Within an emission region of the jet, multiple scatterings of a given photon are very unlikely due to the small optical depth, $\tau_{\rm C} = nR\sigma_{\rm T} \lesssim 10^{-5}$ (Boettcher et al., 2012).

An important part of inverse-Compton scattering is the Compton cross-section. Depending on the energy of the photon relative to that of the scattering electron, the cross section can change significantly, such that

$$\sigma_{\rm C}(\epsilon') \approx \begin{cases} \sigma_{\rm T}\left(1 - 2\epsilon' + \frac{26}{5}\epsilon'\right) & \text{for } \epsilon' \ll 1 \\ \frac{3}{8}\frac{\sigma_{\rm T}}{\epsilon'}\left(\ln[2\epsilon'] + \frac{1}{2}\right) & \text{for } \epsilon' \gg 1. \end{cases} \tag{1.26}$$

Here, $\epsilon \equiv h\nu/(m_{\rm e}c^2)$ is the energy of the photon in units of the electron's rest-mass energy (before scattering), the primed superscript indicates the quantity is being mea-

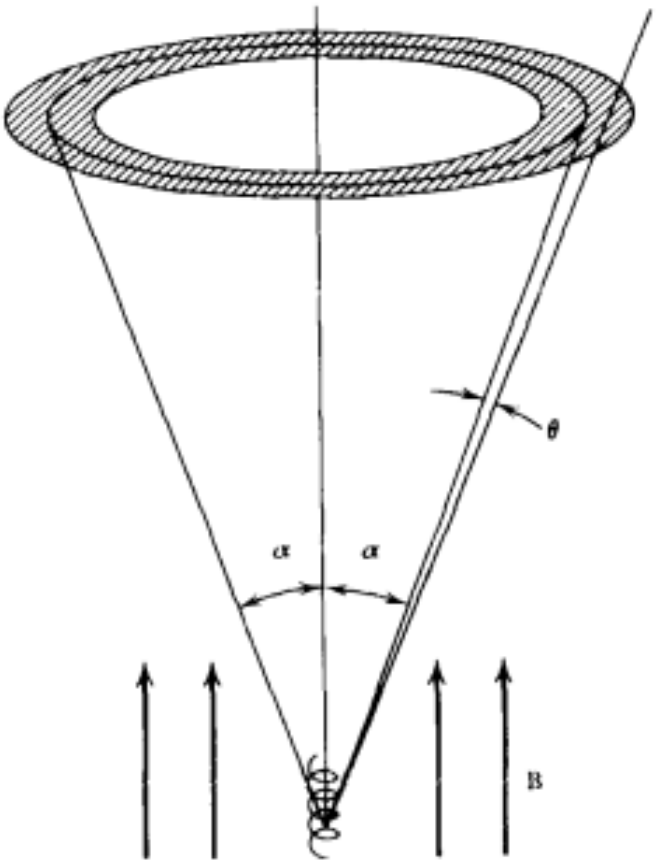

Figure 1.11: Schematic of synchrotron emission from a particle with pitch angle α, with radiation confined to the shaded solid angle region. Taken from Rybicki & Lightman 1979.

sured in the electron's rest frame before scattering (Figure 1.12). The Compton cross-section matches well the Thomson cross-section for small values of $\epsilon' \ll 1$, where the photon energy is far below that of the electron's rest-mass energy; this is called the Thomson regime. Photons scattered in this regime have a scattered photon energy ϵ'_s nearly equal to the incident photon energy ϵ', or $\epsilon'_s \approx \epsilon'$. In the Lab frame, however, the scattered photon energy will be $\epsilon_s \sim \gamma^2 \epsilon$, which represents an energy transfer from the electron to the proton. When the electron is highly relativistic ($\gamma \gg 1$), the energy the photon receives can be very large, capable even of boosting CMB photons from

microwaves to X-rays or Gamma rays.

The limit where $\epsilon' \gg 1$ is known as the Klein-Nishina limit, and is the regime in which the energy transfer from the photon to the electron can be significant.

The total Compton power is given by

$$P_{\rm Comp} = \frac{4}{3}\sigma_{\rm T} c \beta^2 \gamma^2 u_{\rm rad}, \tag{1.27}$$

where $u_{\rm rad}$ is the energy density of the radiation field. This equation for Compton power is nearly identical to that of the synchrotron power (1.18). This is because both processes are fundamentally the same type of interaction, between that of a photon and a charged particle.

In the case of synchrotron self-Compton (SSC), where synchrotron-emitted photons are Compton scattered by their own seed electron population, it follows that

$$\frac{P_{\rm Comp}}{P_{\rm syn}} = \frac{u_{\rm rad}}{u_{\rm B}}. \tag{1.28}$$

1.8 Particle Acceleration

The radiative lifetime of a particle is such that $\tau \propto \nu^{-1/2}$ (e.g., Boettcher et al. 2012), so that all but the lowest energy electrons will lose their energy long before reaching the hotspot many kpc away from the central engine (Harris & Krawczynski, 2007). *In situ* particle acceleration is necessary to explain the observed emission in jet knots and hotspots.

There are many possible ways in which particle acceleration can occur in jet knots. Diffusive shock acceleration (first-order Fermi acceleration) is one such process in which the particles can be accelerated either by an interaction with the external ISM or, more

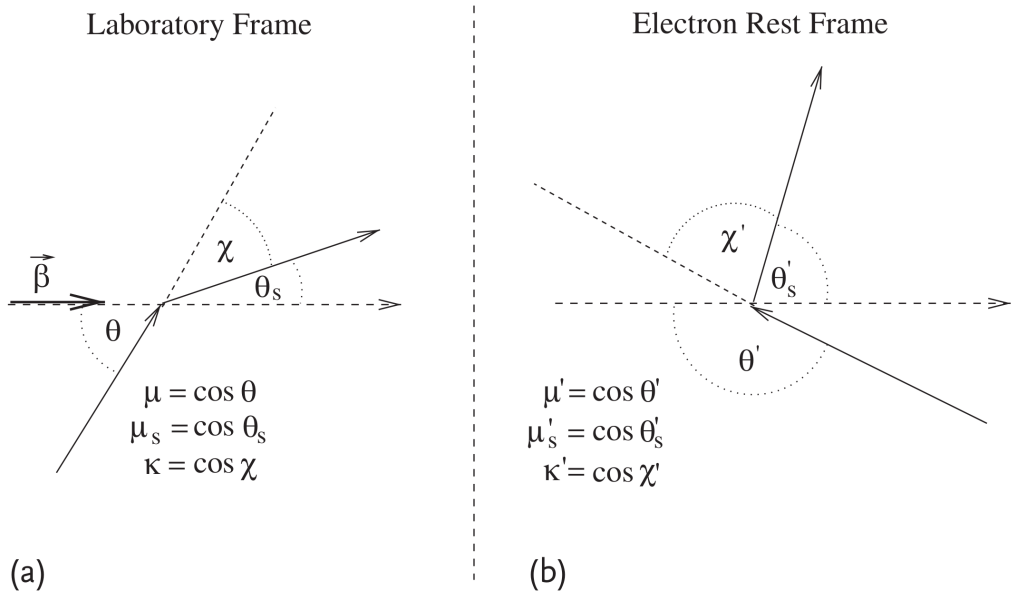

Figure 1.12: Compton scattering geometry for (a) the Lab frame and (b) the electron's rest frame. From Boettcher et al. (2012).

favorably, by particles interacting back-and-forth across a shock boundary. However, it is though that efficient first-order Fermi acceleration cannot take place when the shocks are relativistic, which is thought to be common in the case of FR II jets (Sironi et al., 2015). Relativistic first-order Fermi acceleration is thought to be less efficient due to an anisotropic distribution of particles caused by the high particle velocities relative to that of the shock, limiting the number of Fermi cycles a particle will experience. This is subject to the tuning of parameters (e.g., some assumptions discussed in Lemoine et al. 2006) and has been much less studied than the non-relativistic case.

Shock regions involve not just the acceleration of particles, but also the compression of magnetic field lines which can transfer kinetic energy from the bulk plasma into the magnetic field.

Magnetic reconnection is increasingly thought to play a large role in jet particle acceleration (Zweibel & Yamada, 2009). In a plasma where conditions are such that the

magnetic field lines are not "frozen in" (even temporarily), and provided the magnetic field is strong enough, the field lines can change their topology in such a way that magnetic field energy is then converted into bulk kinetic energy resulting in a burst of particle acceleration. In general, this is thought to be a very efficient method of particle acceleration. However, magnetic reconnection is only expected to take place when the magnetic field energy density exceeds that of the particle energy density. This has the advantage of explaining how a Poynting flux-dominated jet, when launched, can later come to be in equipartition between magnetic field energy and bulk kinetic energy in an efficient way (Sironi et al., 2015).

Chapter 2

Radiative and Emission Processes in Jets

2.1 Jet Emission Mechanisms

In many jets, the observed emission from radio up to optical wavelengths is well-explained by synchrotron radiation from the relativistic particles that make up the jet, because of the strong linear polarization of the emissions (e.g., Perlman et al. 1999) and because the power-law spectra can be smoothly connected between radio and optical wavelengths (e.g., Perlman et al. 2001). This guarantees the presence of X-ray emission at a minimum, well-defined level via the synchrotron self-Compton (SSC) and other inverse-Compton processes.

The first observations with *Chandra* detected excess X-ray flux in the jet of PKS 0637−752 that could not be explained by a single power-law from radio to X-ray (Schwartz et al., 2000). The difference in FR I and FR II SEDs can be seen in Figure 2.1.

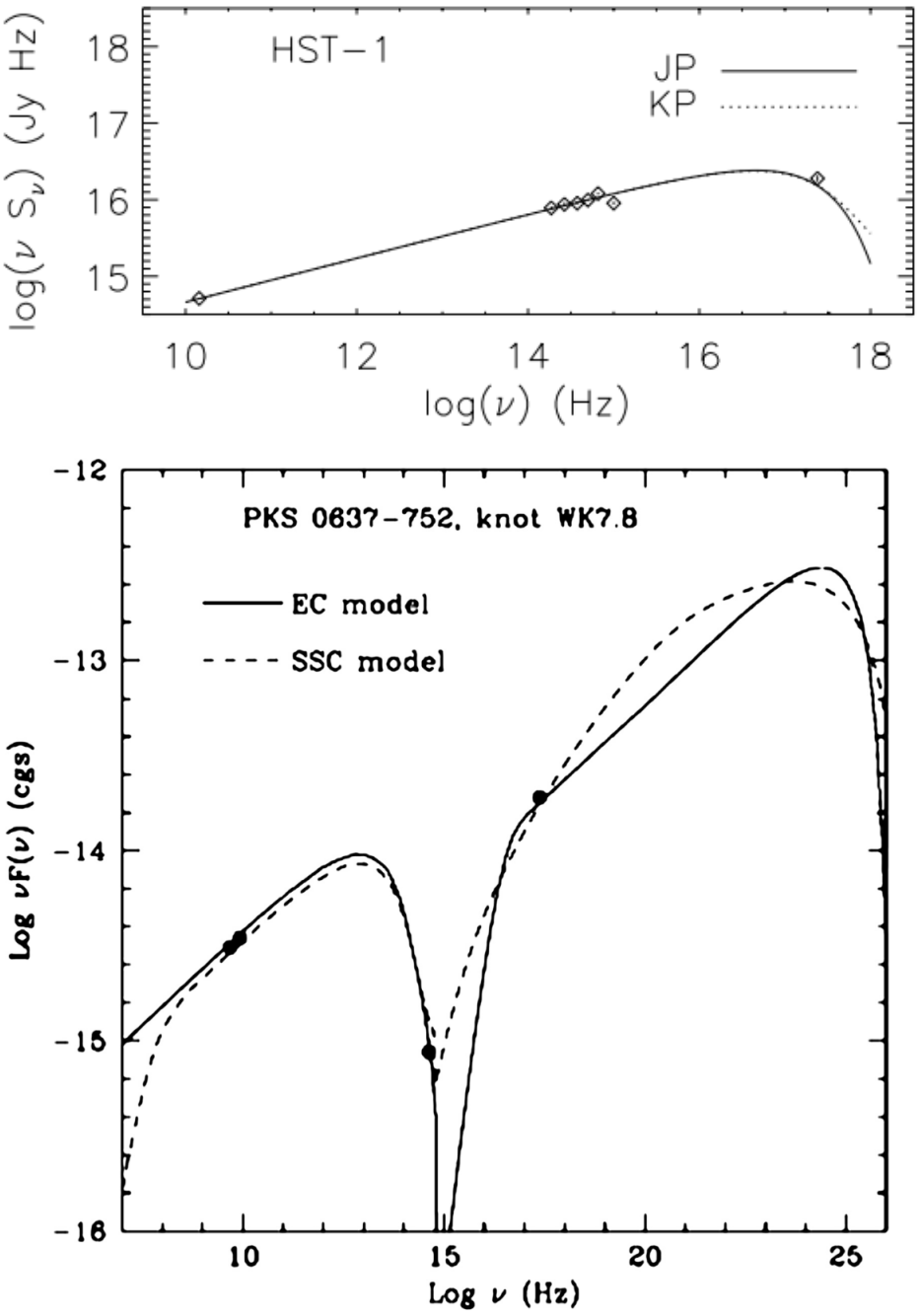

Figure 2.1: Comparison of the broadband SED of FR I vs FR II jets. *Top*: (FR I) SED and model fit for the HST-1 region of the M87 jet. The spectrum from radio to X-ray can be fit by a single power-law distribution. Adapted from Marshall et al. (2002). *Bottom*: (FR II) SED and models fit to the WK7.8 knot of the PKS 0637−752 jet. The model fitting requires two separate components, as the radio-optical component cannot be extrapolated to the observed bright X-ray flux. From Tavecchio et al. (2000).

Tavecchio et al. (2000) first made the case that the necessary second emission component was due to inverse-Compton scattering of Cosmic Microwave Background (CMB) photons by the relativistic electrons in these jets. Over the next decade, the so-called IC/CMB (or EC/CMB) mechanism was the dominant explanation for the detected X-ray flux in FR II jets.

For the case of low-power FR I jets, the observed X-ray emission has been shown to be connected to the same spectral energy distribution (SED) that is responsible for the radio through optical emission (e.g., Hardcastle et al. 2001). While particle acceleration is necessary to explain the observed X-ray flux in bright FR I jet regions, it is likely not as extreme as the particle acceleration in the case of FR II jet regions.

For the more powerful FR II (quasar) jets, in all cases the observed X-ray flux is higher than that predicted by the extrapolated SED from radio through optical – higher than the predicted synchrotron self-Compton (SSC) flux by a factor of 10 or more when equipartition is assumed (Worrall, 2009; Marshall et al., 2005). Figure 2.1 shows an example where SSC can be fit to the observed fluxes, however this requires a jet that is far out of equipartition (discussed in Tavecchio et al. 2000) and thus having very different kinematics from the IC/CMB explanation.

The CMB is unique as a seed photon field because its density increases with cosmological redshift, such that its boosted energy density (in the jet frame) is

$$u'(\mathrm{CMB}) = 4 \times 10^{-13}\ (1+z)^4\ \Gamma^2\ \ \mathrm{erg\ cm^{-3}}, \tag{2.1}$$

(e.g., Harris & Krawczynski 2006). Consequently, IC/CMB is much more likely to be dominant in jets at large redshifts than in those nearby. It also has the advantage of being a mandatory process that must be taking place to some degree in FR II jets and requires only a single population of electrons, but places heavy constraints on other

jet parameters (Tavecchio et al., 2000). In particular, it demands a highly relativistic jet with bulk Lorentz factor $\Gamma \sim 10$ over distances of perhaps hundreds of kpc (since an inverse-Compton-scattered photon is boosted by a factor of $\sim \gamma^2$). IC/CMB also favors a small viewing angle to the observer, so that the Doppler factor is very high, to explain the observed X-ray flux in many jets. It also often demands a jet kinetic power in excess of the Eddington limit.

The Γ^2 term in (2.1) is why the CMB is particularly important as a seed photon field. Other photon fields, such as starlight from the host galaxy, will have a reduced factor of Γ^2 in energy density (in the relativistic jet frame) compared to the CMB field (Begelman et al., 1984).

Another possible explanation for the detected X-ray emission is that of synchrotron emission from a second population of relativistic electrons. This model does not require the jet to be highly relativistic or to have a small viewing angle. It does, however, require extremely efficient particle acceleration *in situ* along the large-scale jet.

Recent work has demonstrated strong evidence against the IC/CMB model in several FR II jets (Cara et al., 2013; Meyer & Georganopoulos, 2014; Meyer et al., 2015, 2016; Clautice et al., 2016; Breiding et al., 2017) using various independent methods. Today, the simplest explanation for the observed X-ray emission is that a second population of electrons emitting their own high-energy synchrotron photons. It requires, however, extremely efficient particle acceleration reaching at least $\gamma \sim 10^8$ operating *in situ* at distances of hundreds of kpc from the central engine. The nature of this acceleration is an open question, with many possible explanations, including instabilities within the jet, interactions with the external medium, density propagation, or the result of a local intensification of the magnetic field (Uchiyama et al., 2006; Georganopoulos et al., 2016).

Given the weight of evidence, it seems clear now that for many FR II jets the high-

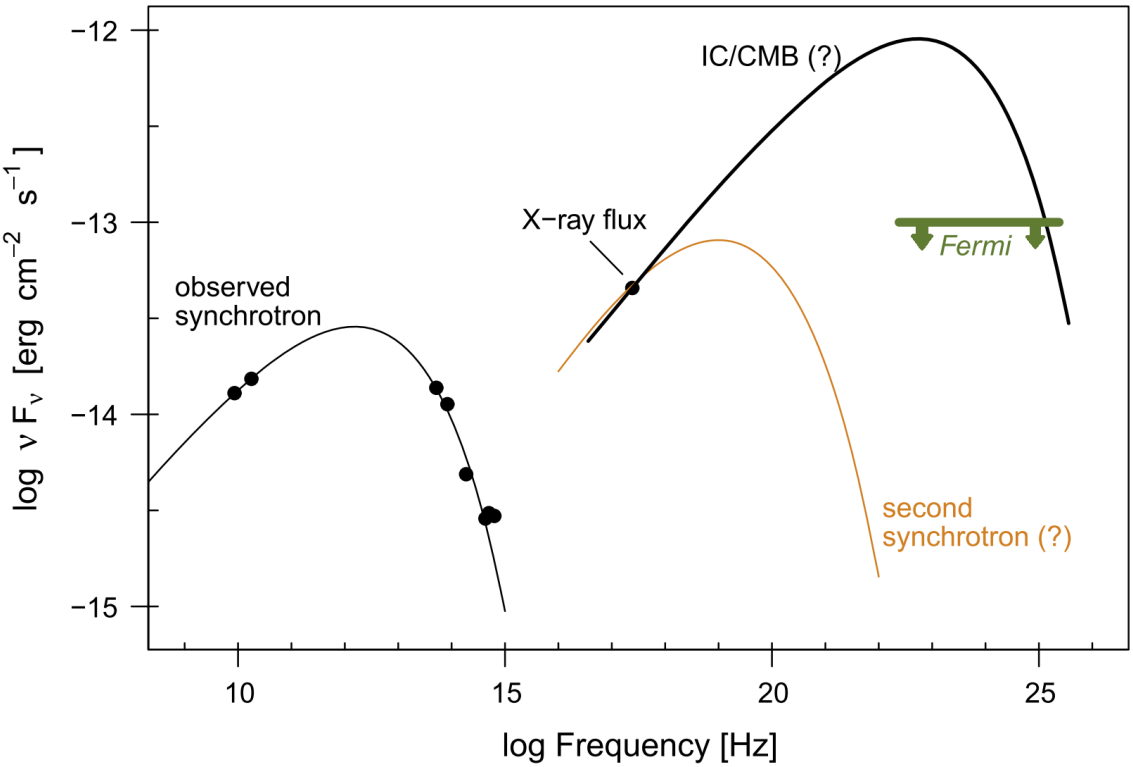

Figure 2.2: Broadband SED models fitted to the observed flux in the PKS 0637−752 jet (total emission). Both the synchrotron and IC/CMB models are a fit for the photometry data (and X-ray spectral index), so additional methods are needed to favor one over the other. The green line represents the frequency range over which *Fermi* can provide an upper flux limit. Adapted from Meyer et al. 2015.

energy emission is synchrotron in nature. Given that the IC/CMB model underpinned much of the work in the field of FR II jets for more than a decade, and that there are still some that invoke it as the preferred explanation, it is important that we work to solidify our understanding of the physics involved in these jets. The two-synchrotron model has profound implications for the kinematics of these jets (requiring a different jet composition) and the nature of extreme particle acceleration within their kpc-scale emission regions.

Figure 2.2 shows SED models for the IC/CMB and second-synchrotron cases of one such FR II jet (PKS 0637−752). Differentiating between models is difficult with just

optical and X-ray imaging, making optical polarimetry an important diagnostic tool. In the case of Meyer et al. (2015), they used observations from the Fermi Gamma-ray Space Telescope to disfavor the IC/CMB model.

Our previous work in Clautice et al. (2016) found a significant spatial offset between the peak radio, infrared, and X-ray emission in several knots of the 3C 111 jet, strongly implying the presence of separate electron populations responsible for the low- and high-energy emission.

2.1.1 Gamma-rays as a Diagnostic of IC/CMB

One of the most important recent tests developed to test the high-energy emission in FR II jets is using the *Fermi* Gamma-ray Space Telescope. *Fermi* lacks the resolution to resolve and separate the jet emission from that of the AGN core. However, while the jet emission is relatively constant, the Gamma-ray emission from the core varies significantly with time, allowing for an upper limit of Gamma-ray jet flux to be determined.

Meyer & Georganopoulos (2014) used *Fermi* observations to put an upper limit on the gamma-ray flux from the jet of 3C 273 − they found an upper limit that is below the flux predicted by the IC/CMB model. The authors have applied the same technique to rule out IC/CMB for PKS 0637-752 (Meyer et al., 2015). This method has now been used to rule out IC/CMB in several other jets (Breiding et al., 2017, 2023).

The *Fermi* test has proven to be a powerful technique for ruling out IC/CMB in numerous FR II jets, however it does not provide any new information with which to constrain particle acceleration within the jets in the case of the second-synchrotron model, or indeed in any alternative model to IC/CMB. This is an important reason why optical polarimetry remains such an important tool in studying jets, with its unique

ability to show us the ordering of jet magnetic field regions.

2.2 Polarization of Synchrotron Radiation

Rybicki & Lightman (1979) provides a full derivation and treatment for the synchrotron emission of both an individual charge and a distribution of charged particles and the polarization properties thereof. The radiation emitted by a single relativistic charge will be elliptically polarized, however for a reasonable distribution of synchrotron-emitting particles the elliptical components of polarization will cancel out. Legg & Westfold (1968) showed that the circular components of polarization are cancelled out to greater degree as γ becomes larger. Thus, radiation from a highly-relativistic synchrotron-emitting source is expected to be partially linearly polarized.

This is confirmed by circular polarimetry observations of AGN jet regions using VLBI. Homan et al. (2018) analyzed 278 sources from the MOJAVE program observed from 2002 to 2009. They found typical levels of circular polarization to be in the range of 0.3% to 0.7%, with a few sources as high as 1%.

Observations of linear polarization in jets are discussed later in §2.3. The theoretical maximum linear polarization we would expect to observe can be calculated using standard parameters for the electron distribution. The total net polarization of the emission can be calculated by integrating over the range of pitch angles within the velocity cone of the emitting relativistic electrons. This simplifies to

$$P_{\max} = \frac{p+1}{p+\frac{7}{3}}. \tag{2.2}$$

For a typical electron index of $p = 2$, we have a theoretical maximum polarization of $P_{\max} \approx 70\%$.

The fractional polarization we are measuring is representative of how well-ordered

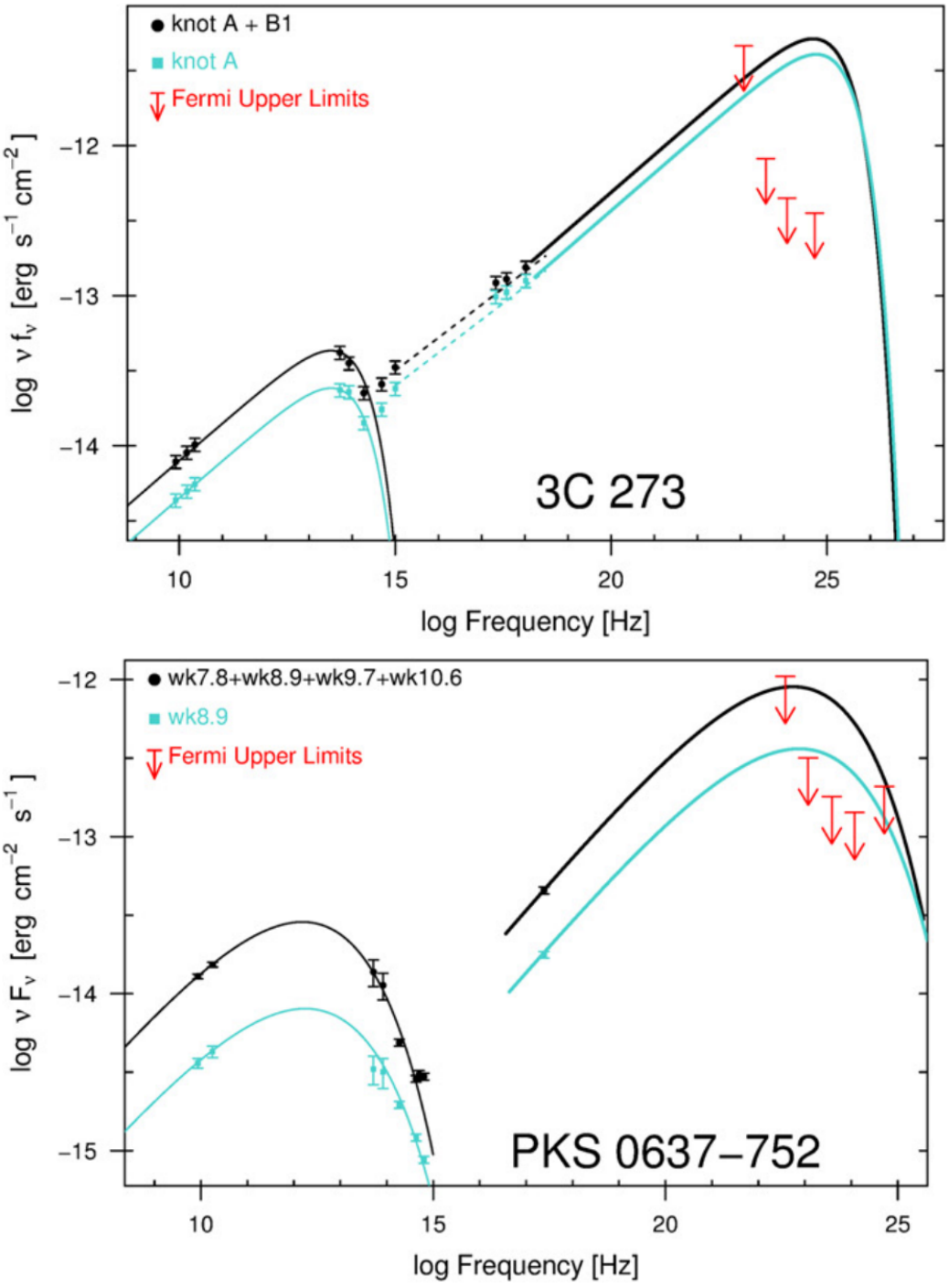

Figure 2.3: SEDs and *Fermi* Gamma-ray upper limits for the (*top*) 3C 273 and (*bottom*) PKS 0637−752 jets. Taken from Meyer & Georganopoulos (2014); Meyer et al. (2015).

the magnetic fields in the region are, and so this maximum value coincides with perfect ordering of the magnetic fields. In practice, the magnetic fields are expected to be disordered to some degree, which would decrease the fraction of observed polarization. A polarization lower than the maximum could also be indicative of multiple emission regions with differing polarization angles accounting for the emitted flux.

2.3 Jet Polarimetry Studies

Optical polarimetry has been used on many FR I jets by our group and has been invaluable in understanding their nature. To date, optical *HST* polarimetry analyses have been performed for ∼7 FR I jets (Perlman et al., 1999, 2006, 2010; Perlman & Wilson, 2005; Dulwich et al., 2007, 2009), which represents a large fraction of the ∼17 known FR I jets with detected optical emission (Boettcher et al., 2012). Of these, M87 is by far the most well-studied due to its proximity ($z = 0.00427$) and brightness. Avachat et al. (2016) compared the radio and optical polarimetry of M87; they found a similar helical polarization structure in the two bands in the nucleus, as well as a much higher fractional polarization in the optical emission of HST-1 thought to be caused by a shock deep within the inner jet. Fundamental issues such as the 3-dimensional magnetic field configuration, the role of jet dynamics and magnetic field configuration in particle acceleration, and the energetics of the X-ray emission in have been probed in these polarimetry studies of FR I jets.

Polarimetry also provides the best evidence of the synchrotron nature of jet emission; synchrotron emission is predicted to be highly polarized (up to $\sim 75\%$, depending on the kinematics of the particular jet), whereas IC/CMB is expected to be unpolarized because the seed photon field (the CMB) is itself unpolarized (Uchiyama et al., 2007; Krawczynski, 2012). Polarimetry studies of FR I jets have shown an anti-correlation

between peak flux and fractional polarization, representing a disordered magnetic field structure where the flux is maximum. However, fractional polarization is shown to be high in the areas adjacent to the flux maximum; this will be shown and discussed in Chapter 6.

To date, high-quality *HST* polarimetry has been analyzed for just one FR II jet, that of PKS 1136-135 (Cara et al., 2013). While powerful, optical polarimetry requires a large SNR ($\gtrsim$ 20 in a region) to yield the most accurate results. Since many FR II jets are faint in the optical (due in part to their high amount of beaming), long exposure times are needed, and the relatively high background of ground-based data is a limiting factor. In some FR II jet knots (such as in the 3C 273 jet), the optical emission is part of the high-energy emission component, and thus optical polarimetry can be used to probe the nature of the highly-efficient particle acceleration demanded within these jets.

Cara et al. (2013) was the first to provide strong evidence against the IC/CMB model as a reasonable explanation for the high-energy emission of an FR II jet, as they found the emission to be highly polarized (Figure 2.4).

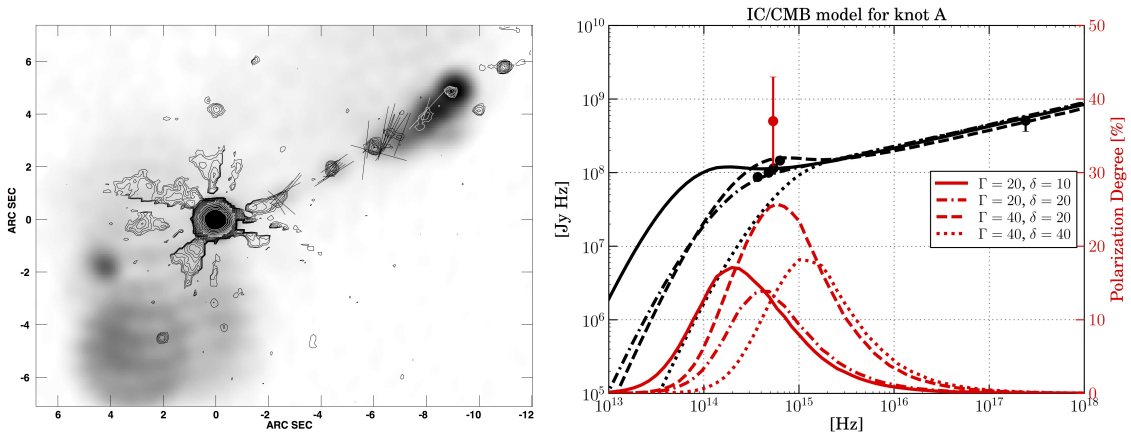

Figure 2.4: *Left*: Radio image of the PKS 1136-135 jet, with optical *HST* contours and polarization vectors. A 1" vector represents $\Pi_{\rm Optical} = 40\%$. *Right*: The SED in intensity (black) and polarization degree (red) for modeled IC/CMB emission, along with *HST* results for knot A. Taken from Cara et al. 2013.

Chapter 3

Jets in This Study

All three jets in this study have FR II characteristics and are launched from radio-loud quasars.

3.1 3C 273

3C 273 was one of the first quasars to be discovered and is the brightest optical quasar known. Its jet is one of the most well-studied, having been one of the first FR II jets to be discovered. Figure 3.1 shows an archival optical image of the nucleus and approaching jet.

3C 273 is well-suited for multi-band polarimetric study due to its brightness and many visible optical components. 3C 273 has been extensively analyzed previously (Jester et al., 2005, 2006, 2007; Uchiyama et al., 2006), however without our much improved optical polarization data. Here we will discuss some of the more relevant studies that have been published on the jet.

Thomson et al. (1993) studied the 3C 273 jet using *HST* optical polarimetry, however with observations that were taken early in *HST*'s mission, using the Faint Object

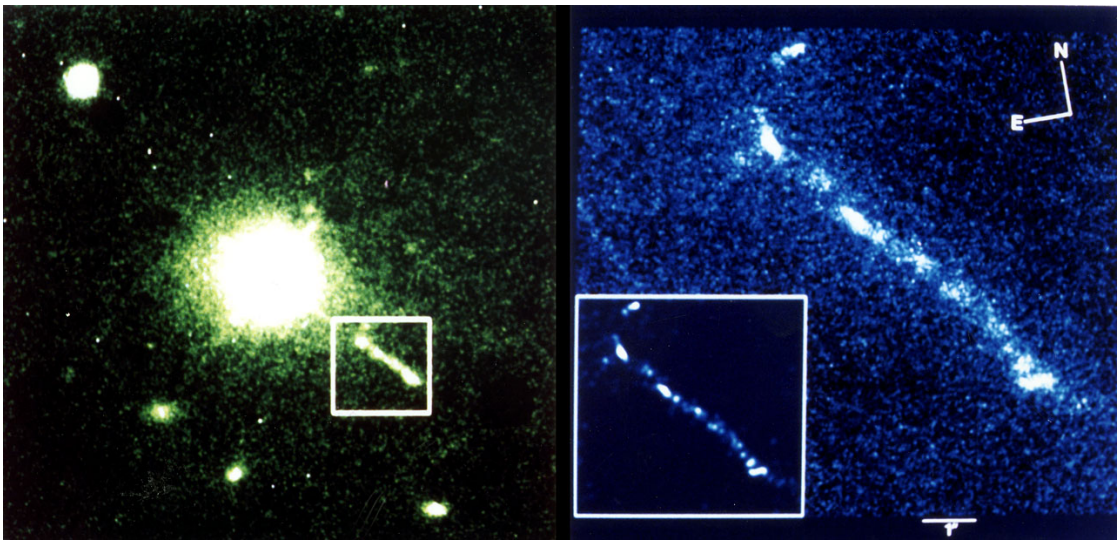

Figure 3.1: Archival V- and B- band optical image of the 3C 273 core and jet. Data from pre-COSTAR *HST*/FOC observations by Thomson et al. (1993) and processed by NASA.

Camera (FOC) before the optics were corrected with the Corrective Optics Space Telescope Axial Replacement (COSTAR). Consequently, the fractional polarization map from that data is significantly lower SNR and resolution than that we have obtained with our new observations. Their observations exhibit significant differences with existing ground-based polarimetry data (Roeser & Meisenheimer, 1991; Thomson et al., 1993). Figure 3.2 shows the optical polarization map using that data.

Jester et al. (2005, 2006, 2007) performed a thorough study on the broadband SED of each of the 3C 273 jet knots. They used new *HST* and *Chandra* observations to construct the broadband SED and X-ray spectral indices. We use the flux values they measured in constructing our broadband SED (discussed in §6). Their SED modeling showed the likelihood that the X-ray emission was from a synchrotron source in at least some of the knots. In particular Knots A, B1, and B2 have an excess X-ray flux that cannot be connected to the radio by a single power law (as we discussed in §2.1).

Meyer & Georganopoulos (2014) used the *Fermi* Gamma-ray Space Telescope to

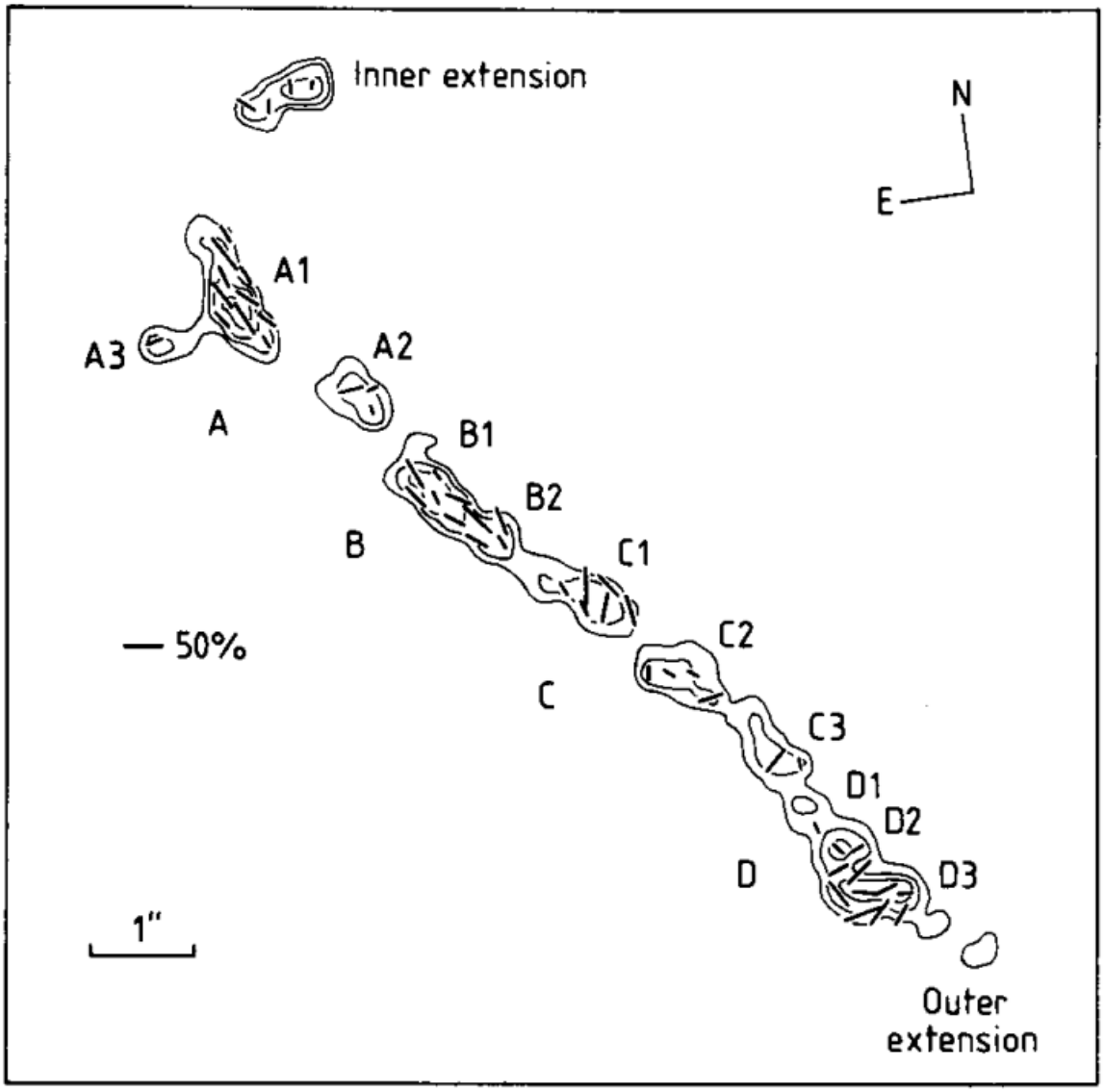

Figure 3.2: Pre-COSTAR *HST*/FOC optical polarimetry map of the 3C 273 jet. Taken from Thomson et al. (1993).

test the IC/CMB case for the 3C 273 jet. This method was discussed in §2.1.1 and the broadband SED and upper limits are shown in Figure 2.3. They measured Gamma-ray upper limits that are above the modeled SED for the IC/CMB case, thus ruling it out for this jet.

Most recently, Meyer et al. (2016) conducted a proper motion study of the 3C 273 jet. They analyzed *HST* imaging taken over a period of 19 years and found no significant proper-motion in any jet knot. They conclude that the jet is mildly relativistic at kpc scales, having a bulk Lorentz factor of $\Gamma < 2.9$, making the high-energy emission unlikely to be caused by IC/CMB.

3.2 PKS 0637−752

The PKS 0637−752 jet was the first target observed with *Chandra*, and the first for which an unexplained excess X-ray flux was found (Schwartz et al., 2000). IC/CMB was initially favored as the most reasonable explanation for the X-ray emission. Tavecchio et al. (2000) first made the case that the high-energy emission component was due to inverse-Compton scattering of the CMB photon field. Figure 3.3 shows archival optical and X-ray images of the PKS 0637−752 jet.

Due to its high redshift ($z = 0.651$), measurements of its superluminal motion (implying $\delta > 8$, Tavecchio et al. 2000), and the associated CMB photon density ($u'(\mathrm{CMB}) \propto (1+z)^4\ \Gamma^2$), it has been considered an ideal jet for IC/CMB to be dominant.

Mehta et al. (2009) used *HST* and *Chandra* observations to analyze the broadband SED from radio to X-ray of the PKS 0637−752 jet and its implications for jet physics, though without the inclusion of optical polarimetry which we now have. We use the flux values they measured in constructing our broadband SED as well (discussed in

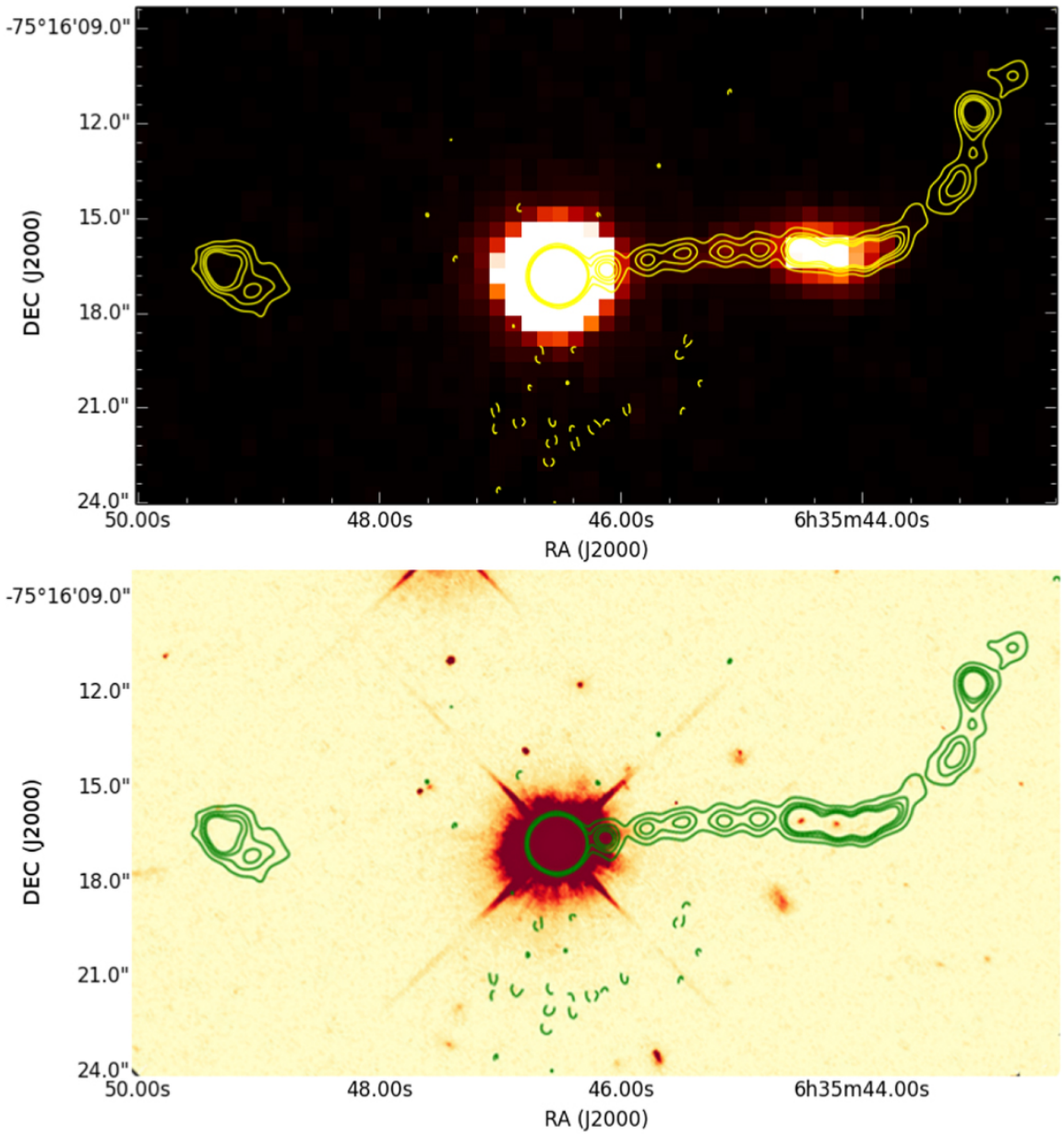

Figure 3.3: Archival *Chandra* (*top*) and *HST* (*bottom*) images of the PKS 0637−752 nucleus, approaching jet, and counter-jet radio hotspot, with ATCA 18GHz radio contours overlaid. Taken from Meyer et al. (2015).

§6).

Meyer et al. (2015) used the *Fermi* Gamma-ray Space Telescope to test the IC/CMB case for the PKS 0637−752 jet. This method was discussed in §2.1.1 and the SED and upper limits are shown in Figure 2.3. They measured Gamma-ray upper limits that are above the modeled SED for the IC/CMB case, thus ruling it out for this jet.

3.3 1150+497

The 1150+497 jet is the least-studied of the three jets in this project. The broadband SED of the jet was previously analyzed from radio to X-ray (Sambruna et al., 2006a,b). Our new observations using *HST* and *Chandra* provide much deeper images of the jet.

Figure 3.4 shows their published multiwavelength images of the 1150+497 jet. Figure 3.5 shows their constructed broadband SEDs and X-ray spectral indices for each jet knot.

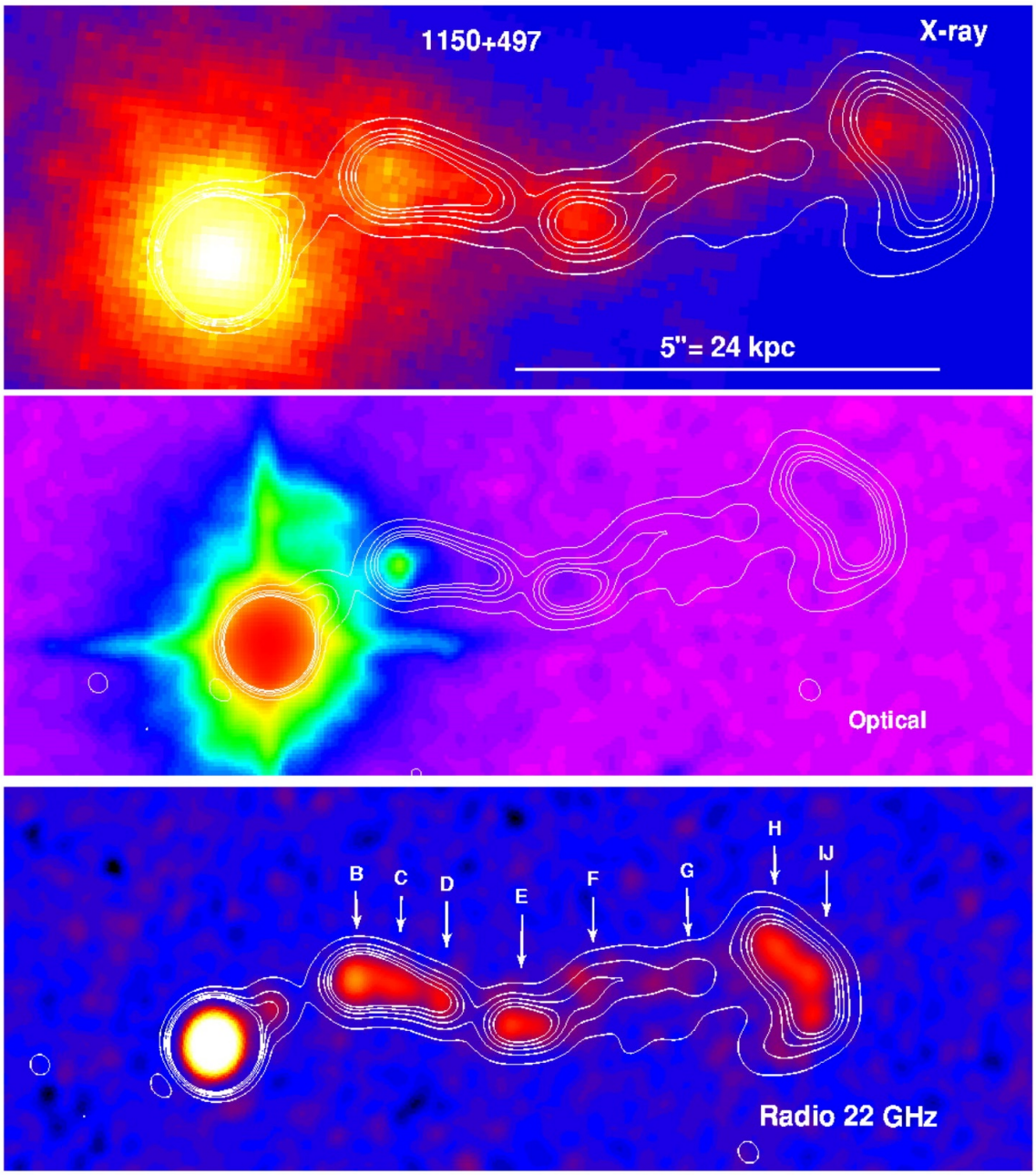

Figure 3.4: Archival *Chandra*, *HST*, and 22 GHz VLA radio images of the 1150+497 nucleus and approaching jet, with 4.9 GHz VLA radio contours overlaid. Taken from Sambruna et al. (2006a).

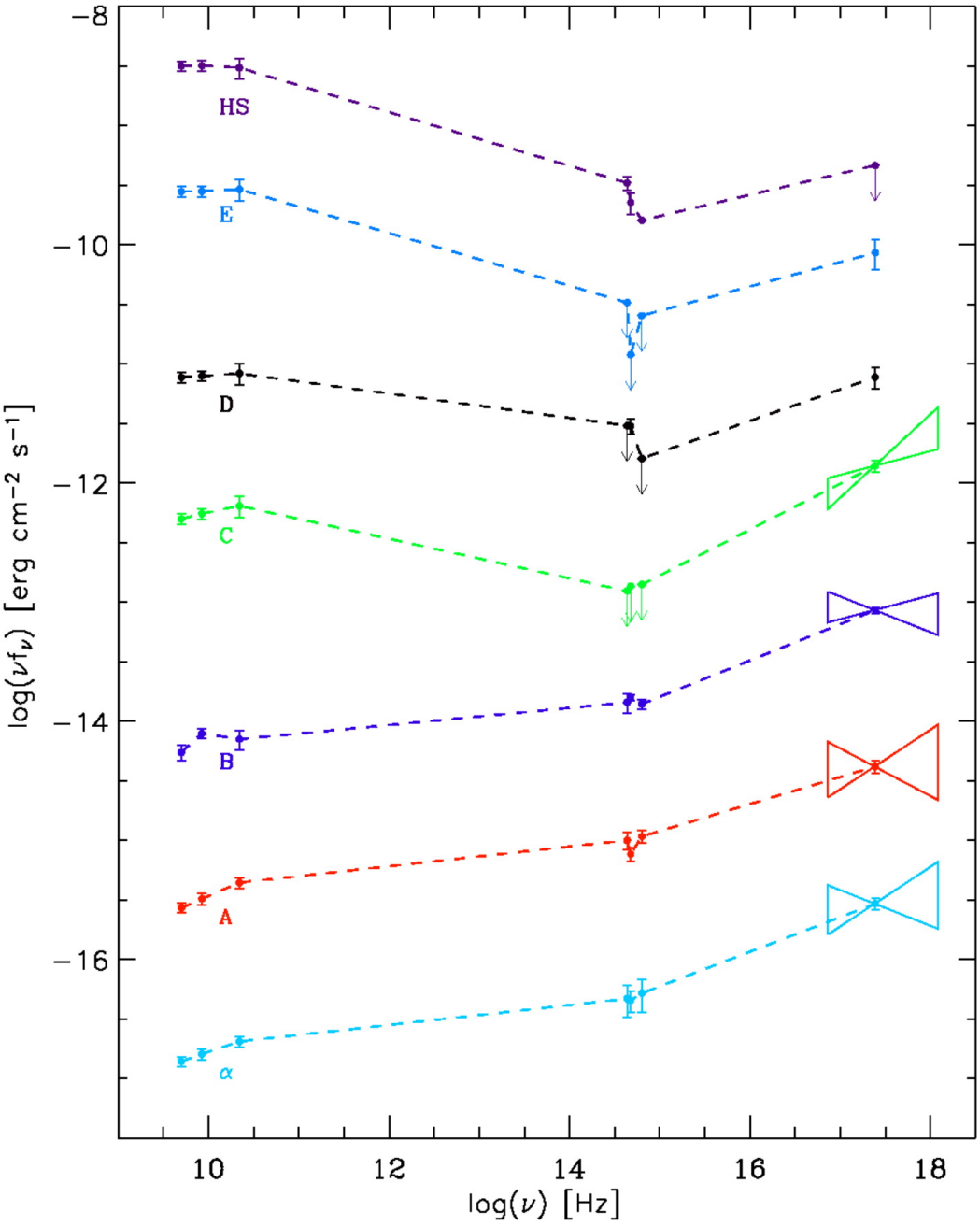

Figure 3.5: Archival broadband SEDs of 1150+497 jet knots. Figure taken from Sambruna et al. (2006a); the author has applied arbitrary vertical shifts for clarity.

Chapter 4

Observations and Data Reduction

4.1 Overview

This project is focused on new optical Hubble Space Telescope (*HST*) polarimetry observations of three quasar jets: 3C 273, PKS 0637−752, and 1150+497. Each target jet was chosen based on previous observations which showed that the optical-to-X-ray emission lies on a second SED component for at least some of the bright jet knots.

We have also acquired new X-ray observations of the PKS 0637−752 and 1150+497 jets using the Chandra X-ray Observatory (*Chandra*).

Details of the new observations are given in tables 4.1 and 4.2. In total, the observation time for our new data amounts to 33 orbits of *HST* and 380 ks of *Chandra*. Each jet also has archival radio images available which were used to compare morphology, flux, and polarization.

4.2 Optical

In this section is described our new *HST* observations and the various data reduction techniques that were used to improve data quality. *HST* is a space telescope with a primary mirror of diameter 2.4 m and several instruments specializing in near-IR through UV observations with good spatial resolution and sensitivity. It has the unique capability of performing optical and UV polarimetry from space.

4.2.1 *HST* Observations

All of our new *HST* observations were taken with the Advanced Camera for Surveys (ACS) instrument and the Wide Field Channel (WFC) detector. ACS is a third-generation instrument that was installed in March 2002, with the WFC channel having been restored to service in May 2009. The ACS instrument has two other detectors in it, the High Resolution Channel (unavailable since January 2007) and the Solar Blind Channel. The ACS Instrument Handbook (Ryon et al., 2021) provides full technical specifications for the instrument and its capabilities and is the source of most information in this section.

The ACS/WFC detector is a versatile instrument with a very large field of view (202 × 202 arcsec), allowing for a large selection of wavelength filters over a broad range (from 350 nm to 1100 nm). The large field of view allowed us to comfortably fit each jet in the frame of the image with no issues.

For our observation planning, each orbit of *HST* was divided into two long-duration dithered exposures (∼1410 seconds each, disregarding overhead), and one short-duration (∼125 seconds) exposure when orbital time permitted. For our PKS 0637−752 observations, this provided a total of eight long-duration and four short-duration dithered exposures per filter (0°, 60°, and 120°), which were later combined as described in

Table 4.1: Hubble Space Telescope (*HST*) Polarimetry Observations

Jet	Program	Instrument	Filter Set	Obs. Date	Exp. Time[a] (s)
1150+497	11,138	ACS/WFC	F606W + POLV	19–23 December 2009	7,890
3C 273	13,764	ACS/WFC	F606W + POLV	6–7 January 2015	7,492
PKS 0637−752	14,696	ACS/WFC	F606W + POLV	18–23 November 2017	11,585

[a]Exposure times are per polarizing filter combination. Total exposure time is a factor three higher.

§4.2.2. For 3C 273, there were six long-duration exposures per filter.

The observations of 1150+497 differ in that we used one exposure per orbit resulting in a total of three long-duration exposures for each filter. All exposures were dithered between orbits.

Dithering is necessary for the removal of cosmic ray strikes, data from bad or dead pixels, and to allow for sub-pixel sampling (providing for higher resolution). Dithering is a technique where multiple exposures are taken using an offset in pointing position of the telescope. Typically this involves a small offset, though where large clumps of dead pixels exist on some detectors a large offset in pointing may be necessary. A four-point dither is encouraged for *HST* observations because it greatly decreases the likelihood of having no useful data on a given pixel.

The ACS/WFC detector is undersampled by a factor of as much as three (Ryon et al., 2021), furthering the usefulness of dithering. By utilizing a pointing offset of half of a pixel within the dither pattern, the PSF can be spread between different combinations of pixels and the mosaicking of multiple dithered exposures can allow for better sampling of the PSF, allowing for higher resolution in the final science image.

In all cases we used standard dithering patterns (ACS-WFC-DITHER-BOX and ACS-WFC-DITHER-LINE) which have varying pixel spacing depending on the number of dithers and orbits. The result is that every exposure is separated by a number of pixels and sub-pixels. For example, the default pattern of a four-point ACS-WFC-DITHER-BOX is a pixel spacing of (0, 0), (5.0, 1.5), (2.5, 4.5), (-2.5, 3.0).

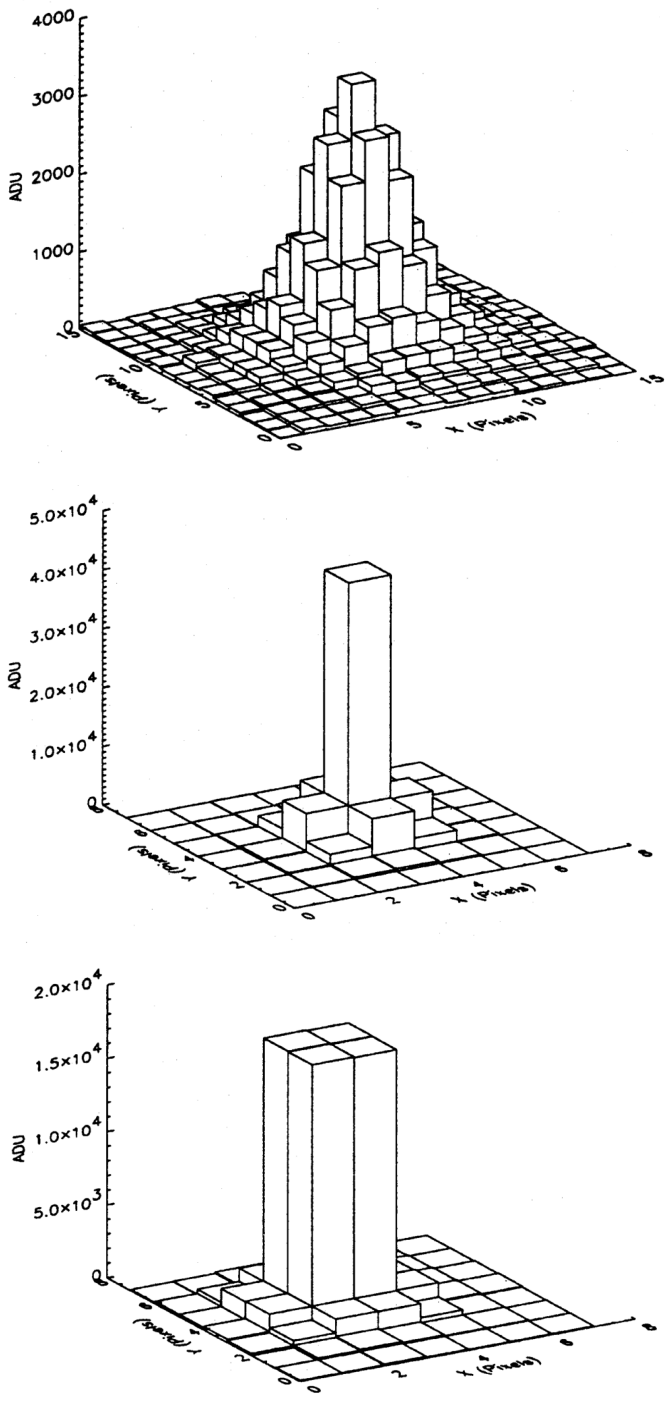

Figure 4.1: The same point spread function (PSF) is shown in each panel with varying degrees of sampling ratio and position on the detector (reproduced from Howell et al. 1996).

4.2.2 *HST* Data Reduction

The data reduction for our *HST* observations was done primarily with AstroConda and the Python programming language. When requested for download, *HST* data are processed using On-The-Fly-Reprocessing (OTFR), which incorporates the use of `calwf3` and `AstroDrizzle` − software written by STScI for use in calibrating and processing HST images (Lucas et al., 2021).

`calwf3` is used in the pipeline process to handle the necessary calibration steps, while `AstroDrizzle` can be used manually to adjust the specific parameters of image processing and whose main purpose is to align and combine *HST* images; both of these are included in a software package called `DrizzlePac`, which also includes various other programs for handling *HST* data. The individual **raw** exposures are processed by `calwf3` to give the calibrated **flt** files. The steps involved with this include flagging bad pixels in the data quality (DQ) array, subtracting off the bias, dark image and read noise (described below), correcting for photometric non-linearity and calculating the photometric values needed for flux conversion, and flat-fielding and applying the gain. The bias image is usually an image taken with an exposure time of zero seconds; it allows for determining the noise level within each frame. Dark current is the thermal noise from the CCD itself and tends to increase linearly with time. `calwf3` uses the associated dark frame, scales it, and subtracts it from each science image. Flat fielding is the process in which the telescope is exposed to a light source of uniform brightness, such as a lamp or a white wall; this is done to correct for pixel-to-pixel variations in the CCD response and account for any nonuniform sensitivity of the detector. The primary flat field images used were created while the detector was still on the ground; these are supplemented by in-orbit "L-flats" which are created by exposing different parts of the detector to the same bright region of stars. These are then multiplied into the ground-based flat field image and that is what is used by `calwf3` for processing.

Since our new *HST* data were taken with the ACS instrument, the ACS Destripe Plus module from the `ACSTOOLS` Python library was used to correct for instrument artifacts such as charge transfer efficiency (CTE) degradation and striping (Lucas et al., 2021; Anderson & Ryon, 2018). CTE of the ACS/WFC detector has been declining since it was first installed on *HST* and is the result of accumulated damage to the silicon in the detector caused primarily by cosmic ray strikes. A primary effect of this degradation is an increase in charge traps, resulting in a striping pattern as the CCD is read out; other effects, such as an increase in the number of hot pixels, are handled earlier in the calibration process. This tool is applied to each **raw** file and generates a new calibrated and destriped **flt** file. Figure 4.2 shows a before and after comparison of the destriping process.

After this, the `tweakreg` tool (part of the `DrizzlePac` package) was used to improve the alignment between each of the **flt** files. When mosaicking images, it is important that the header of each file includes World Coordinate System (WCS) information that is aligned to sub-pixel accuracy. `Tweakreg` allows for the alignment of several images to one another or to an external reference image.

The `AstroDrizzle` task was then used to mosaic the images for each filter. Because our observations were taken using the F606W+POLV filter set, we essentially have three independent sets of *HST* exposures. Each set of calibrated and aligned **flt** images for the 0°, 60°, and 120° filters must be combined with `AstroDrizzle` separately, and will later be used to calculate the Stokes vector (discussed in §4.2.2.1). The observations taken with each filter were dithered as discussed previously, so that the mosaicked output for each filter will have all cosmic ray strikes removed (example shown in Figure 4.3).

The linchpin of `AstroDrizzle` is the variable-pixel linear reconstruction algorithm, better known as Drizzle. By drizzling multiple dithered images, a closer approximation

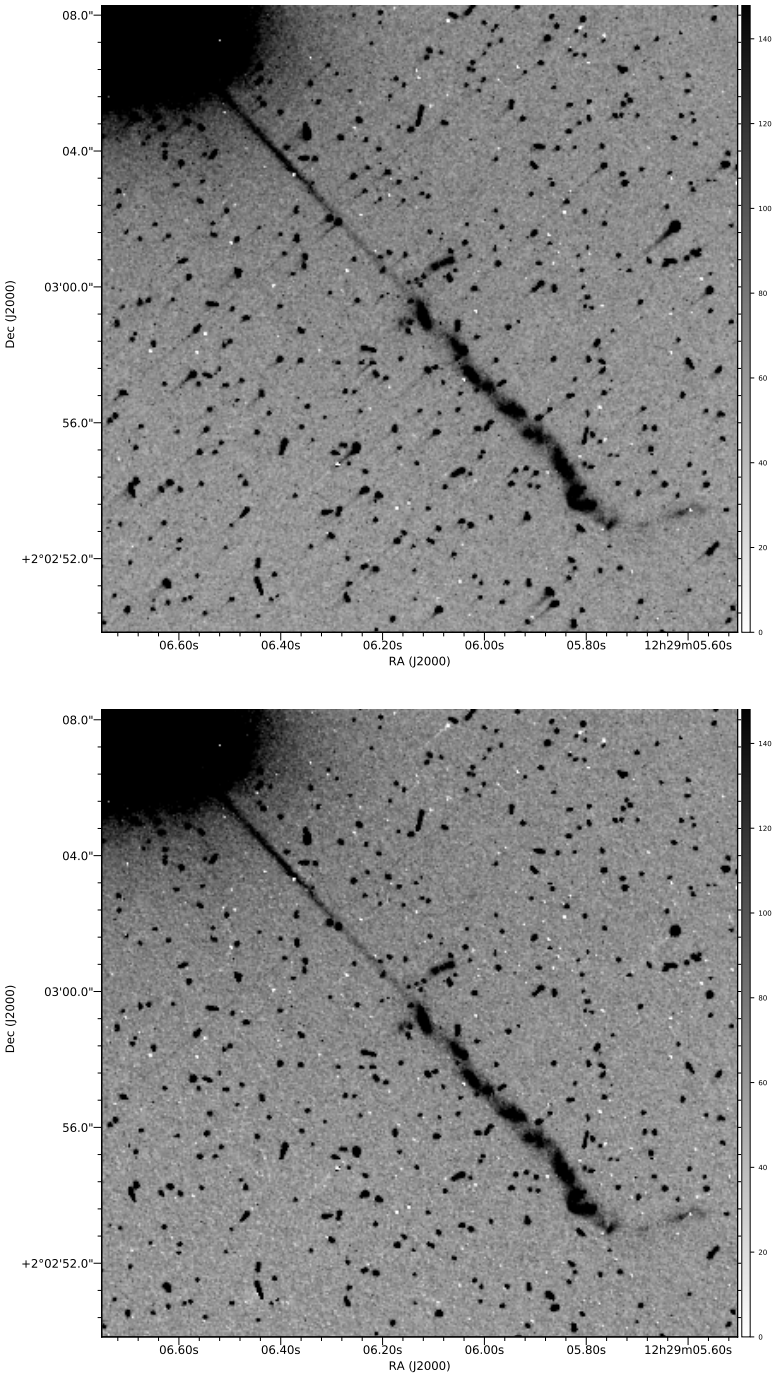

Figure 4.2: One of our *HST*/ACS+F606W POLV exposures before (*top*) and after (*bottom*) CTE correction and destriping. Note that cosmic ray strikes are removed later in the data reduction process (also see Figure 4.3).

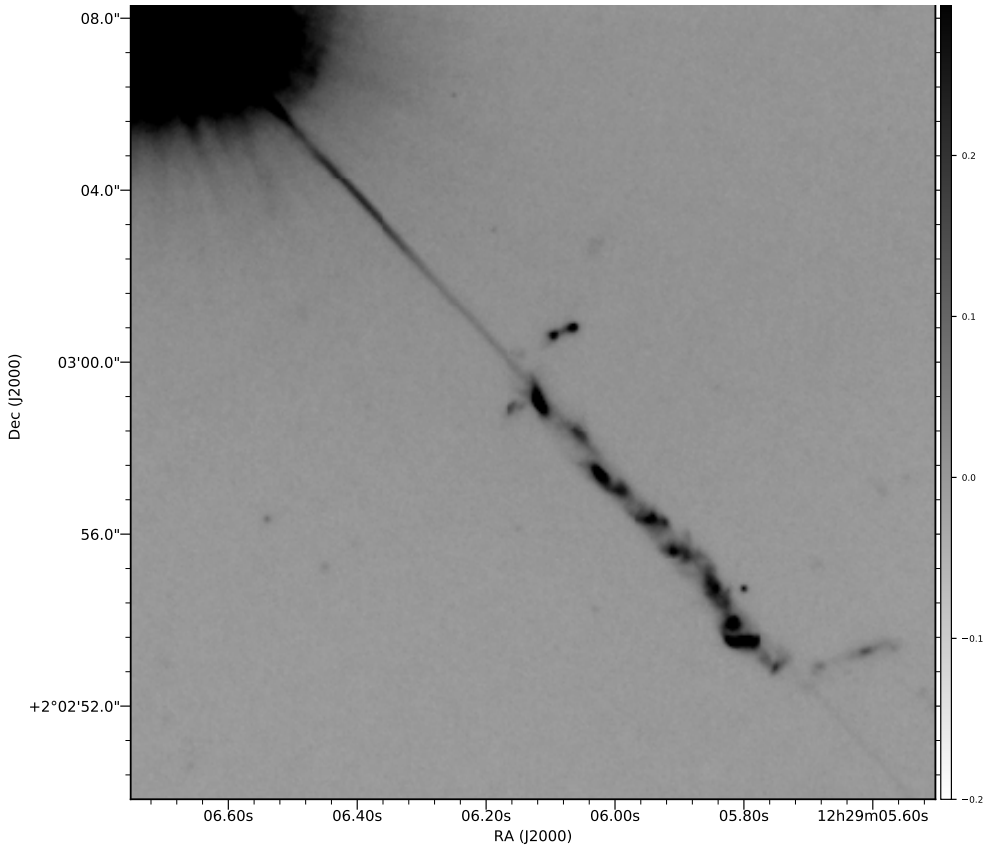

Figure 4.3: Drizzled *HST*/ACS+F606W image showing the result of cosmic ray removal for the 3C 273 jet.

of the "true sky" image can be recovered (Gonzaga et al., 2012). Drizzling allows for the pixel size to be shrunken using the pixfrac parameter before it is averaged onto the output image. The shrunken pixels are aligned and geometrically corrected before being "drizzled" onto the subsampled pixel grid (shown in Figure 4.4). The flux from each input pixel is divided up proportionally to how much of its area was drizzled onto the subsampled image. In practice, the Drizzle algorithm has shown good success in recovering information that is lost due to the finite size of detector pixels (Figure 4.5). `AstroDrizzle` must account for the differences in exposure time between each combined image and also factor in the drizzling process to create a weight map.

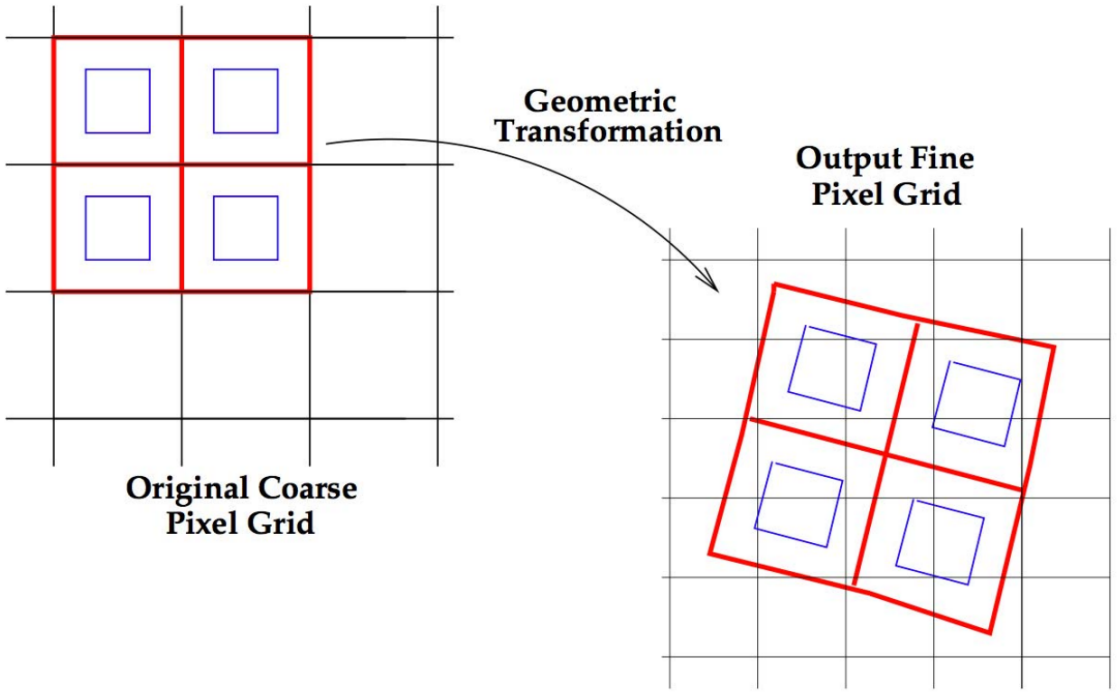

Figure 4.4: Schematic representation of how Drizzle maps input pixels onto the output image. The pixfrac parameter controls the size ratio between the original (red) pixel size and the shrunken (blue) pixel sizes used to distribute the flux onto the output image (Gonzaga et al., 2012).

`AstroDrizzle` also corrects the geometric distortions in the final output image and removes cosmic rays by comparing the various exposures.

Below, we highlight some of the important parameters we used in `AstroDrizzle` for our data set.

PIXFRAC: The pixfrac parameter determines how the input pixels should be scaled before being drizzled onto the output image. Setting this value to 0 is equivalent to using the interlacing method of combining images, while setting it to 1 is equivalent to the shift-and-add method. In general, a lower pixfrac value will result in higher resolution and lower correlated noise, but a reduced sensitivity to faint features. The DrizzlePac Handbook suggests leaving the parameter set to 1 for the individual drizzling of each exposure, as this helps with cosmic ray rejection, and then using a minimum fraction of

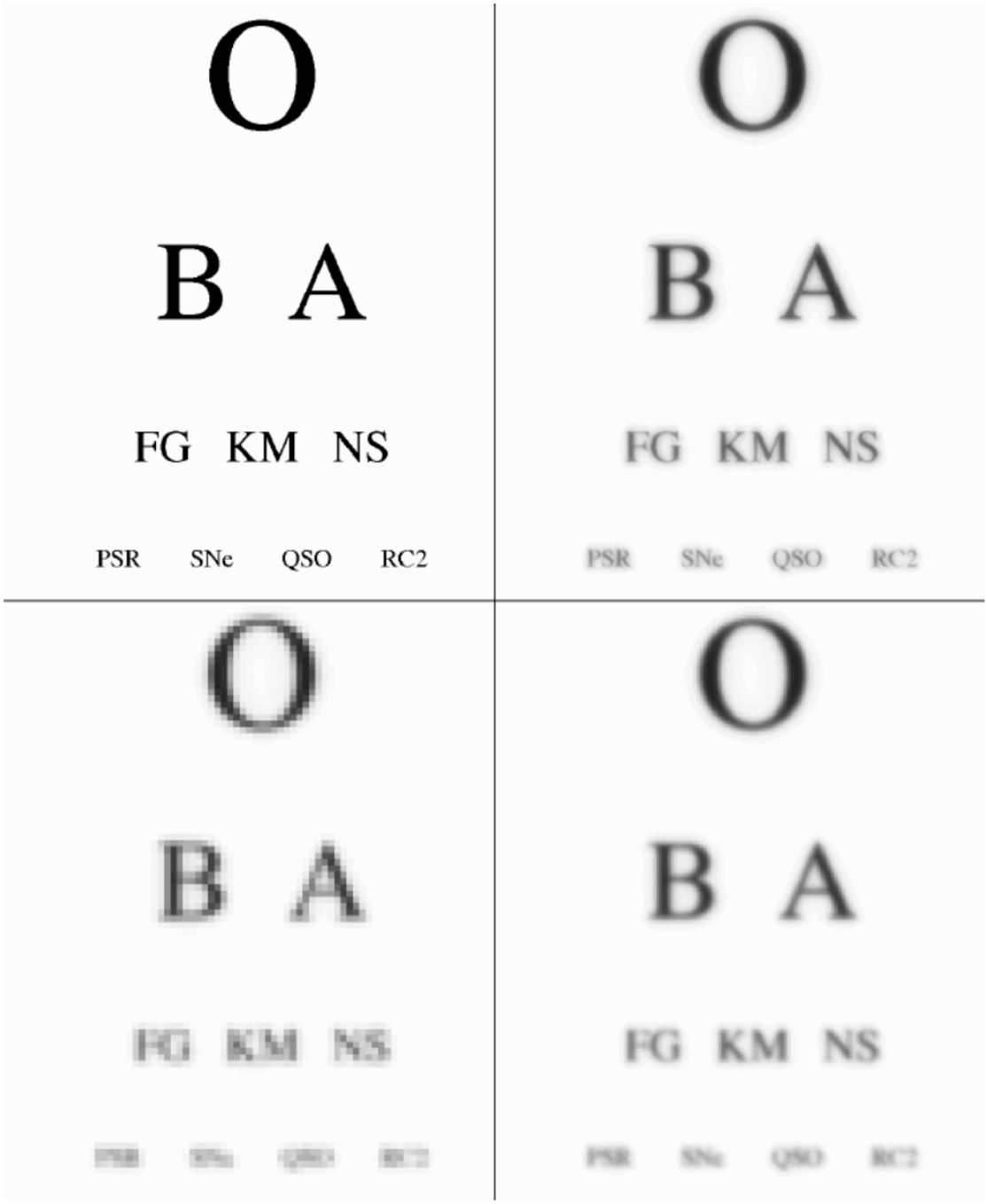

Figure 4.5: *Upper Left*: A "true" image as seen by a telescope of infinite aperture. *Upper Right*: The "true" image convolved with the *HST*/WFPC2 PSF. *Lower Left*: The effect of sampling the convolved image with the WF2 CCD. *Lower Right*: The result of using the Drizzle algorithm to recover information lost due to sampling (Gonzaga et al., 2012).

0.7 when combining the drizzled exposures into the final output image to ensure good coverage. The linear ratio used will depend on the number of images one is combining. Using a too low of a pixfrac value results in some scattered pixels that have no flux from the input images. In our case we used a pixfrac of 0.7.

PIXEL SCALE: The smallest recommended pixel scale is half of the plate scale. In practice, we determined the best scale to be 0.03 arcsec/pixel. This was used in our imaging and photometry, however for our polarimetry calculations we used created images with 0.05 arcsec/pixel (plate scale).

After the exposures were mosaicked, we then updated the WCS coordinates to be more accurate. We used the radio position of the quasar core for each jet, determined from archival radio data, to calibrate its position on our *HST* image. The Astronomical Image Processing System (AIPS) task known as `jmfit` was used to find the pixel value of the center of the quasar core. It does so by fitting Gaussian components to the image and using those to find the peak.

4.2.2.1 Polarimetry Data Reduction

Our *HST*/ACS/WFC+F606W observations employ the use of three polarizing filters that are optimized for visible light, with relative position angles of 0°, 60°, and 120°. The components of the Stokes vector are then calculated as prescribed by section 5.3.4 of the ACS Data Handbook (Lucas et al., 2021):

$$I = \frac{2}{3}\left(r_0 + r_{60} + r_{120}\right) \tag{4.1}$$

$$Q = \frac{2}{3}\left(2r_0 - r_{60} - r_{120}\right) \tag{4.2}$$

$$U = \frac{2}{\sqrt{3}}\left(r_{60} - r_{120}\right), \tag{4.3}$$

where r_n is equal to the count rate measured in a given pixel or aperture multiplied by a constant which differs for each filter. The constants are chosen so that the *Stokes I* will be equivalent to the count rate with no polarizing filter present. The Stokes parameters are then used to calculate the fractional polarization:

$$P = \frac{\sqrt{Q^2 + U^2}}{I} \left(\frac{T_{par} + T_{perp}}{T_{par} - T_{perp}} \right), \tag{4.4}$$

where T_{par} and T_{perp} are constants that differ by filter and serve to correct for cross-polarization leakage. Values for the WFC+F606W filter are $T_{par} = 0.5157$ and $T_{perp} = 5.591 \times 10^{-5}$ (Lucas et al., 2021).

The position angle (in degrees) of the linear polarization E-vector (EVPA) is then calculated:

$$EVPA = \frac{1}{2}\tan^{-1}\left(\frac{U}{Q}\right) + PAV3 + \chi, \tag{4.5}$$

where $PAV3$ is the roll angle of *HST* at the time of the observation (found in the FITS header) and $\chi = -38.2°$ is a constant related to the camera geometry of ACS/WFC. Note that the inferred direction of the magnetic field vector is +90° from the EVPA.

These methods were used on a per-pixel basis to create fractional polarization maps for each jet, and also used to calculate aperture polarimetry values for key jet regions (both discussed in §6). Importantly, the *Stokes I* image approximates the count rate with no polarizing filter in place and can thus be used for photometry.

We then used code to debias the fractional polarization to account for Rician bias (Serkowski, 1958; Wardle & Kronberg, 1974). Measurements of polarization adhere to a Rice distribution rather than a typical Gaussian or Poisson distribution like our

other measurements. In principle,

$$\hat{p} = (p^2 - \sigma^2)^{1/2} \tag{4.6}$$

serves as an accurate estimator given high SNR (Clarke, 2010). The distribution of P will be Rician for small SNR and approximates Gaussian for large SNR. Pixels with SNR<0.1 are excluded, as were pixels with negative P values or values where P was >100%. In practice, the debiasing process has a very small effect for our aperture polarimetry where the SNR is high.

In principle, for high SNR, the uncertainty in the position angle can be described by

$$\sigma_{PA} = \frac{\sigma_p}{2p}\text{rad} = 28^\circ.65\frac{\sigma_p}{p} \tag{4.7}$$

(Naghizadeh-Khouei & Clarke, 1993). For high SNR the uncertainty in PA approximates a Gaussian as well and the errors can be propagated as such.

There is one issue with our 3C 273 data that we are unable to completely resolve. Unfortunately, the roll angle of *HST* during our observations was such that the diffraction spike from the quasar core overlaps the jet (shown in Figure 4.6). We believe that the effect on the fractional polarization should be minor, due to its low SNR at that distance from the core. Also, the EVPA values of the diffraction spike appear to be entirely random well before the first optical component of the jet. We have attempted to compensate for the additional intensity due to the spike in the *Stokes I* image by modeling the fall-off of the spike using values measured inside and outside the radius where the jet appears. While this method is not perfect, it is probably the best we can do as there is no method currently to accurately model a PSF so far from the core (out to 20+ arcsec away from the PSF center).

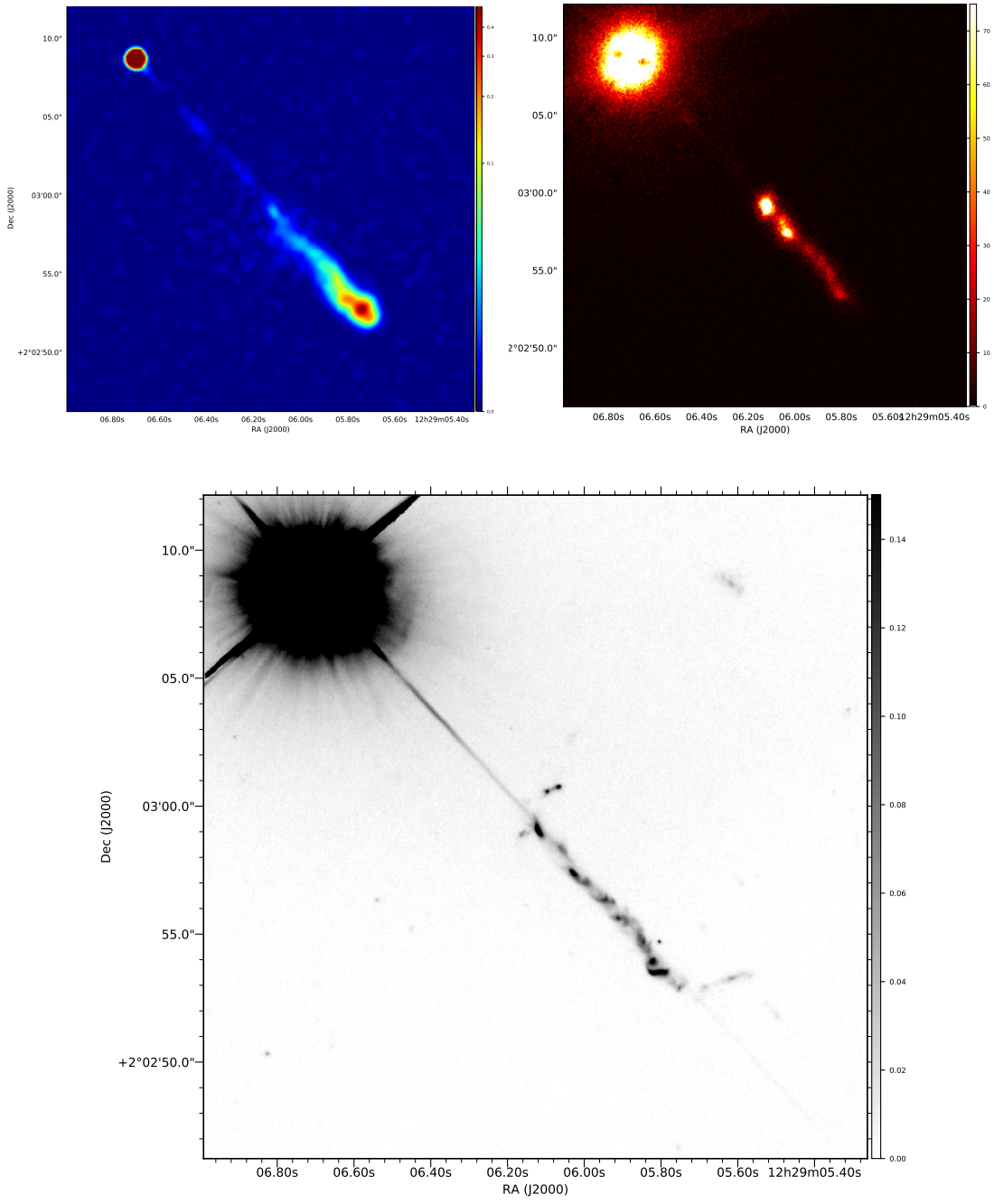

Figure 4.6: The nucleus and approaching jet of 3C 273, oriented north-up. *Top Left*: Archival VLA 8.4 GHz radio image. *Top Right*: Archival *Chandra* X-ray image. *Bottom*: *HST*/ACS+F606W optical *Stokes I* intensity image, from our new observations. Note the lack of optical and X-ray emission over the first half of the length of the jet.

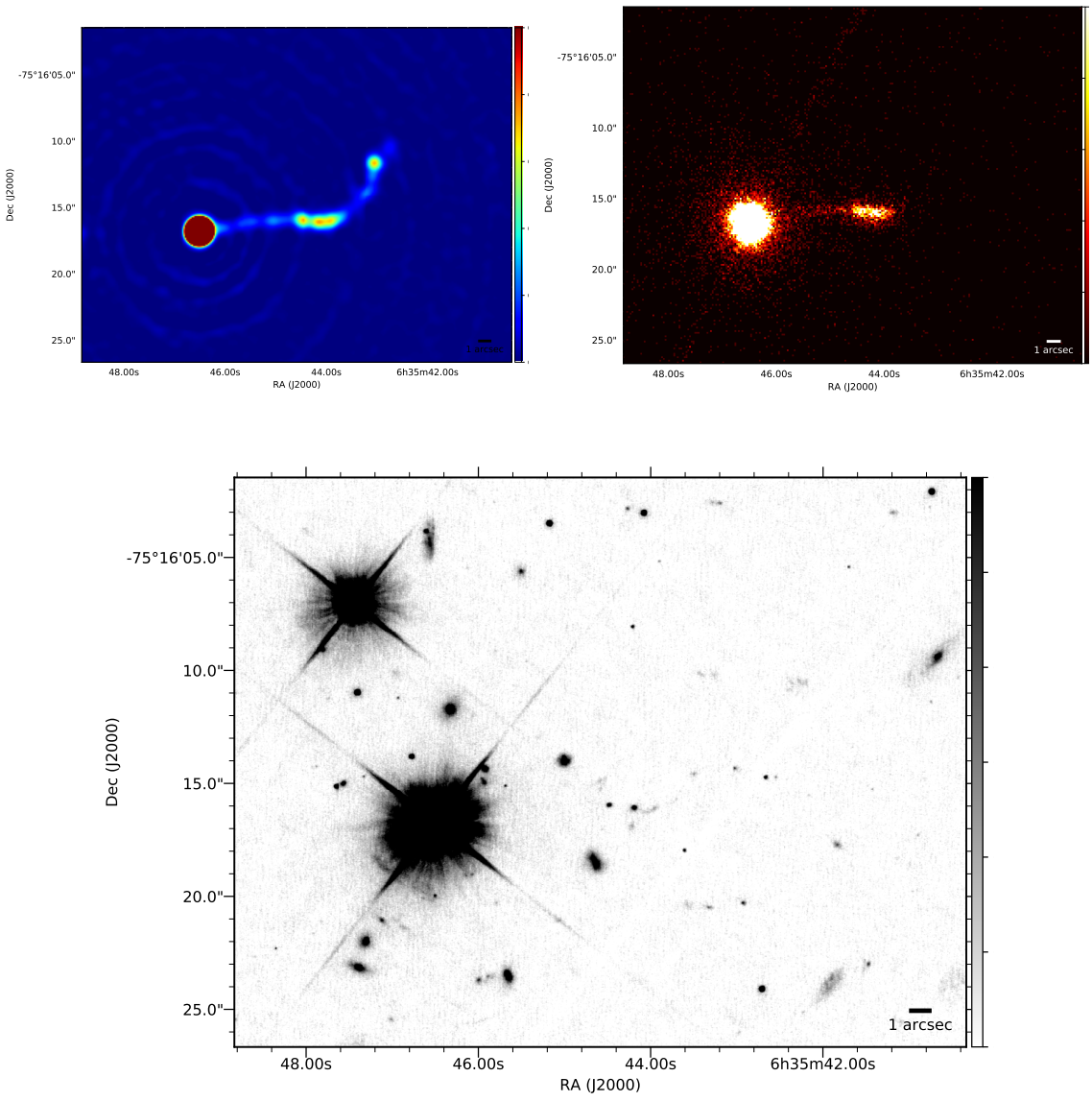

Figure 4.7: The nucleus and approaching jet of PKS 0637−752, oriented north-up. *Top Left*: Archival ATCA 8.64 GHz radio image, with counter-jet hotspot visible to the west of the core. *Top Right*: New 0.3-7 keV *Chandra* X-ray image. *Bottom*: *HST*/ACS+F606W optical *Stokes I* intensity image, from our new observations.

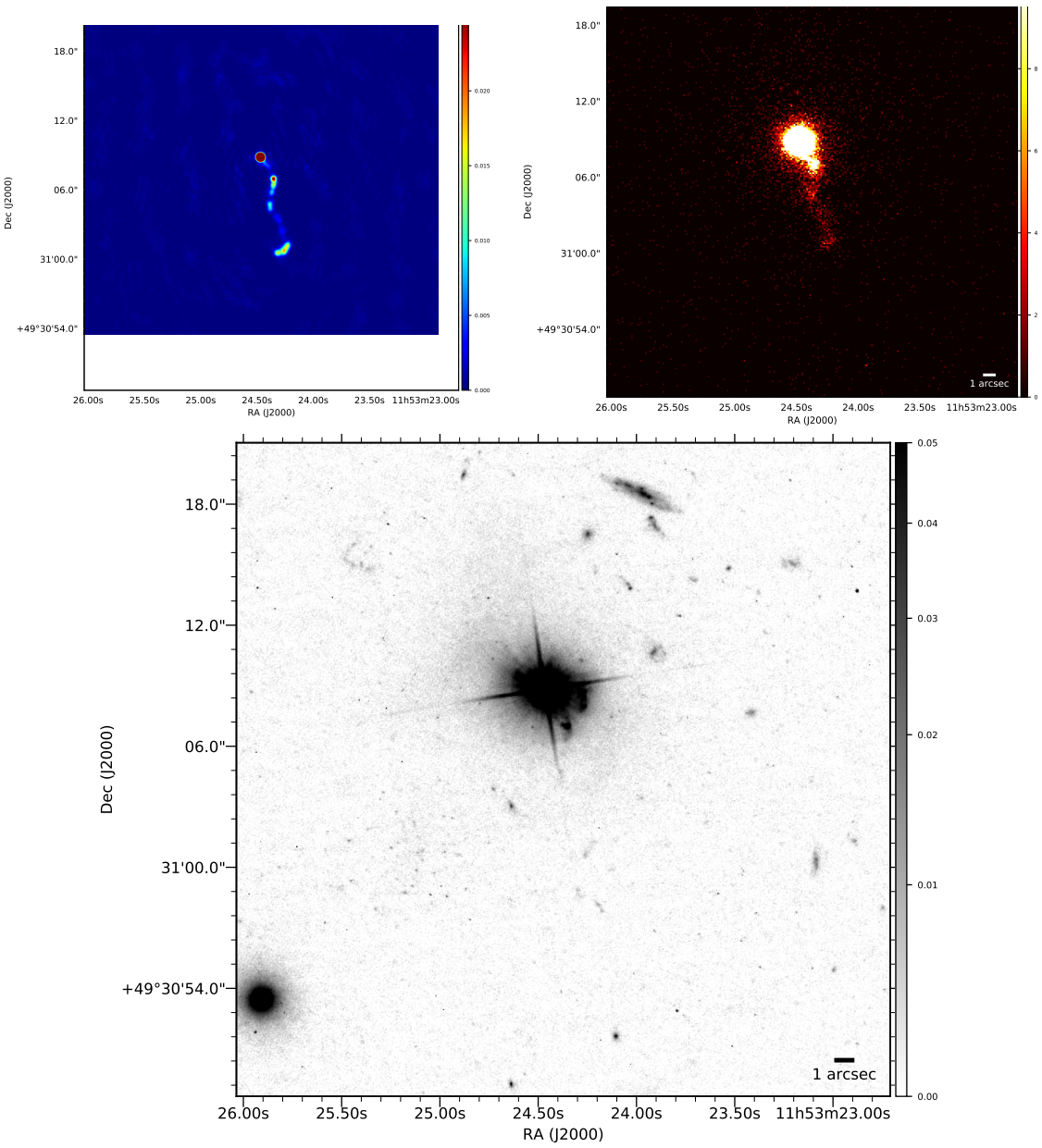

Figure 4.8: The nucleus and approaching jet of 1150+497, oriented north-up. *Top Left*: Archival 1.66 GHz Merlin radio image. *Top Right*: New 0.3-7 keV *Chandra* X-ray image. *Bottom*: *HST*/ACS+F606W optical *Stokes I* intensity image, from our new observations.

4.2.2.2 Galaxy & PSF Subtraction

Since we are interested in faint jet components near to the core of 1150+496, we performed galaxy subtraction on its *Stokes I* image. First we created a region mask of all of the various galaxies and stars present in the image to try to isolate only the contribution in flux from the galaxy. The regions were then converted into pixel masks (FITS images with pixel values of 0s and 1s) using a Python script. The STSDAS package in IRAF contains the task `ellipse`[1], which was then used to fit isophotes at varying distances to the galaxy's core. As part of its input, it takes in the mask so as to exclude most other sources of flux aside from the galaxy itself.

The `bmodel` task was then used to convert the isophote parameters generated by `ellipse` into a FITS image, which was then subtracted from the science image using `imarith` to give a residual output image that (ideally) includes everything except the galaxy's flux contribution. This was done as an iterative process - after the galaxy was subtracted, it makes it easier to see faint sources of flux that can then be excluded before running the `ellipse` task again.

Because each isophote is determined independently, each is subject to its own systematic error in its intensity. If the pixels used to fit one isophote contain a bit of flux from a star that was not completely masked, then the isophote's intensity will be slightly larger than that from the galaxy alone. Likewise, if too many pixels are excluded from the fit, `ellipse` will underestimate the flux from the galaxy for that isophote. To reduce the amount of variation between each isophote, we decided to smooth it out by fitting the isophotes to a Nuker law model (Lauer et al., 1995). The isophote table was then edited so that the model values of intensity replaced the original values. The `bmodel` task was used to convert the isophote table into an image,

[1] `http://stsdas.stsci.edu/documents/SUG/UG_33.html`

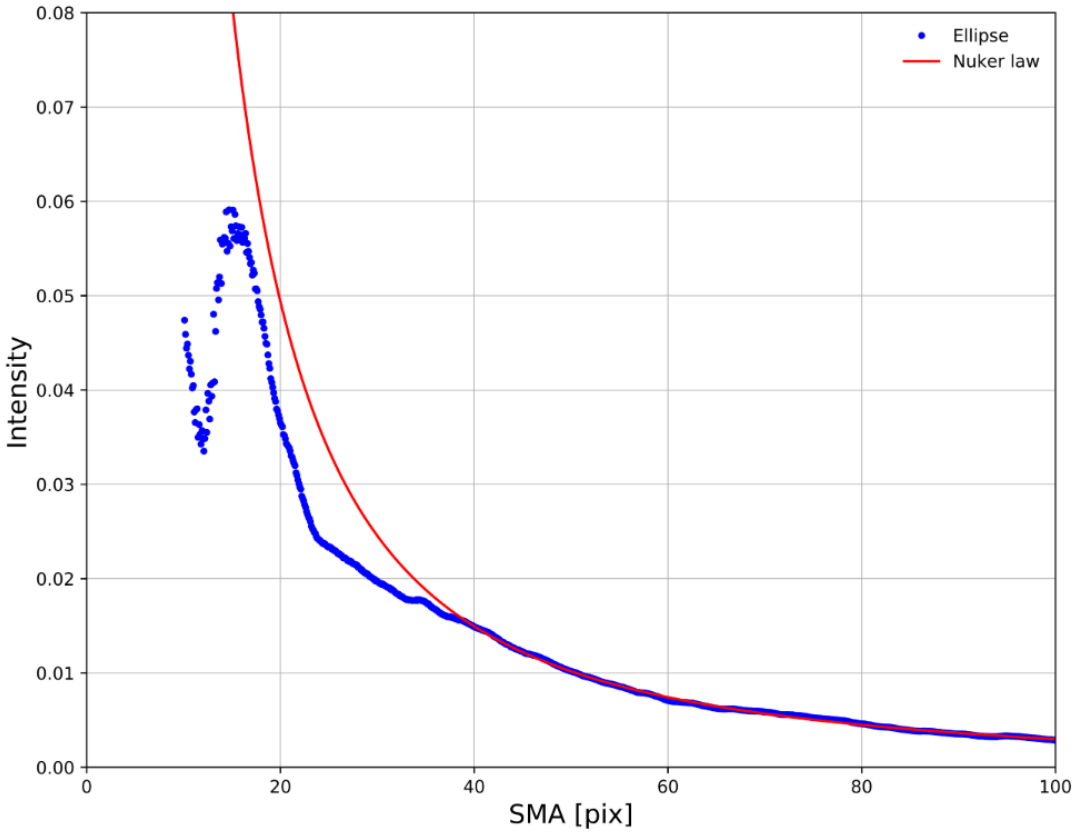

Figure 4.9: The galaxy emission profile of 1150+497 modeled with a Nuker law for our *HST*/ACS/WFC *Stokes I* intensity image fit to isophotes generated with the `ellipse` task in IRAF. The model was only fit to pixels of radius > 40 from the core.

and then the `imarith` task was used to subtract the galaxy model from the original drizzled image. This was successful in smoothing the transitions between isophotes.

Note that we also performed this process using a Sérsic galaxy profile (Sérsic, 1963), and found it to be equivalent to the Nuker profile in the regime that we are fitting. We opted to use the Nuker profile for our fitting due to its supposed better modeling of the inner galaxy region, though we found the differences to be negligible for our case.

Figure 4.9 shows the fitted model; note that the model did not attempt to fit closer to the core than 40 pixels on the image, as the galaxy profile becomes overpowered by the PSF and the emission profile diverges from a Nuker profile. The first optical

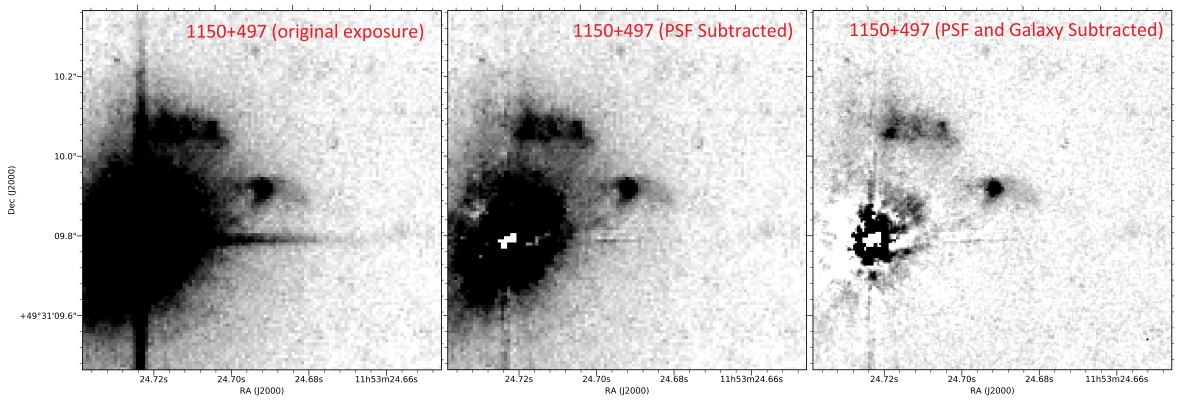

Figure 4.10: Showing the various stages of our process for PSF and galaxy subtraction for the case of 1150+497. Note that galaxy emission has a much larger effect than the PSF at the distance we first detect jet emission. Also note that the artifacts present near the quasar core are a result of not fitting the galaxy subtraction model to the area inside of our detected optical jet emission.

jet component visible in the image appears at ∼55 pixels on the sub-sampled *Stokes I* image, and so we are largely unconcerned with the galaxy subtraction profile inside of that radius.

We also experimented with PSF subtraction for the quasar of 1150+497. We used Tiny Tim (Krist et al., 2011) to generate a model of the PSF given its location on the sensor. We then used Python to scale and align the model PSF with the quasar core and subtract it. Figure 4.10 shows an example for the case of 1150+497. This must be done for each exposure (**flt** file) before drizzling, making the procedure problematic and potentially introducing a separate bias for each **flt** image before they are drizzled. Because the systematic error introduced would be different for each of the three polarizing filter angles, it could potentially cause a significant effect in the calculation of our Stokes parameters which rely on the differences in count rate between each filter. Because of this potentially large effect, we opted not to include PSF subtraction in our final data analysis.

Table 4.2: New *Chandra* X-ray Observatory Observations

Jet	Seq. Num	Data Mode	Obs. Date	Exposure Time (ks)
1150+497	704282	VFAINT	Sept. 2021 – July 2022	251.11
PKS 0637−752	703441	FAINT	27–30 November 2017	113.2

4.3 X-ray

In this section our new and archival *Chandra* X-ray Observatory data is discussed as well as the processes that were used to improve the data quality. All X-ray observations were performed with the same instrument and detector, so the data reduction procedure is the same for all jets except where noted.

4.3.1 *Chandra* X-ray Observations

All X-ray data sets were obtained using the Advanced CCD Imaging Spectrometer (ACIS) onboard *Chandra*, in particular using the ACIS-S array of CCDs. The ACIS-S array allows for high resolution X-ray imaging at an energy range of 0.1 to 10 keV, with a field of view of 8.3 x 8.3 arcmin and a pixel scale of 0.492 ± 0.0001 arcsec/pixel (Chandra team, 2014). The ACIS detector has the capability of generating high-resolution images as well as moderate-resolution spectra, with the option of combining it with either the High Energy Transmission Grating (HETG) or Low Energy Transmission Grating (LETG) to achieve higher resolution spectra, though for our purposes we did not include a grating for our observations. The ACIS detector, like all X-ray detectors, measures individual photons − the large energy of individual photons combined with the relatively low count rate makes this ideal.

The ACIS detector has a section which is exposed for a set time ("full frame time" adjustable from 0.2 to 10 s), after which the charges are quickly read out in parallel into a separate frame. While the next exposure is being taken, the charges are read out

from the frame store region serially, at which point any "events" are detected. This is important for particularly bright sources to prevent pile-up, where in multiple events occur in the same pixels in the same exposure, leading to a loss of information.

To distinguish between good events and bad events (such as cosmic rays), ACIS employs a small "event island" (which is a grid of several pixels) over which the cleaning algorithm is applied. The VFAINT mode of ACIS utilizes a 5x5 event island; this is optimal for very faint sources as it does a much better job of excluding background events - by a factor of up to 1.4 (Vikhlinin, 2002). The downside to this mode is that for bright sources where pile-up superimposes events over one another, it can exclude good events. Other observations use the FAINT mode, in which a 3x3 event island is used to detect background events. FAINT mode is preferred when dealing with bright sources.

4.3.2 *Chandra* X-ray Data Reduction

The data from *Chandra* was processed using version 4.15 of the Chandra Interactive Analysis of Observations (CIAO) software (Fruscione et al., 2006). As mentioned before, X-ray detectors measure individual photons. The list of these detected photons is stored in an "event file," with parameters such as the time of arrival, energy of the photon, position on the detector, etc. This makes the data reduction process significantly different from that used for *HST* data. Event files are stored in FITS format.

The data was first reprocessed using the CIAO task `chandra_repro`. This is a script which automates the standard recommended X-ray data processing tasks. Arnaud et al. (2011) provides a thorough description of this processing and how the events are used to make an image. Reprocessing is beneficial because the calibration files are continuously being improved. The end result of this script is to refine the event

parameters and create a "level=2 event file," which can be used for data analysis. The primary calculation performed is to determine the "grade" of each event. An event requires that a pixel exceeds a minimum charge threshold. The event is graded by considering the eight adjacent pixels and noting which of those also have a charge that exceeds the minimum threshold. The different grades then determine the "resolution" of each photon impact as well as to filter out particle impacts. The total charge of the event is the sum of the charge of those pixels that were above the minimum threshold; this can then be converted into the event energy by using the response matrix. Another task the script performs is to remove any background flares by analyzing the light curve during the observation window. The script also updates the observation-specific bad pixel file.

The default parameters were used when running the `chandra_repro` task. For ACIS, this means using the Energy-Dependent Subpixel Event Repositioning (EDSER) algorithm (Li et al., 2004). This algorithm uses the fact that the PSF is smaller than the size of the pixels to improve image quality when subsampling. This is possible because all *Chandra* observations are dithered − rather than pointing at a fixed position, the telescope is continually dithering in a Lissajous pattern.

The other important parameter is that of VFAINT background cleaning. Since we performed our 1150+497 observations in VFAINT mode, we had the option of using the larger (5x5) event island for cleaning the background. This can allow for better flagging of background events by using more pixels when determining the grade of an event. At its best, this can reduce the particle background by a factor of 2 near 0.5 keV and by a factor of 1.1−1.15 over the 1−5 keV energy range. However, there is an added risk of real events being excluded. This risk becomes a certainty for bright sources where pile-up is an issue. For our data set, comparison showed that some real events were excluded by the VFAINT background cleaning near the AGN core. Given

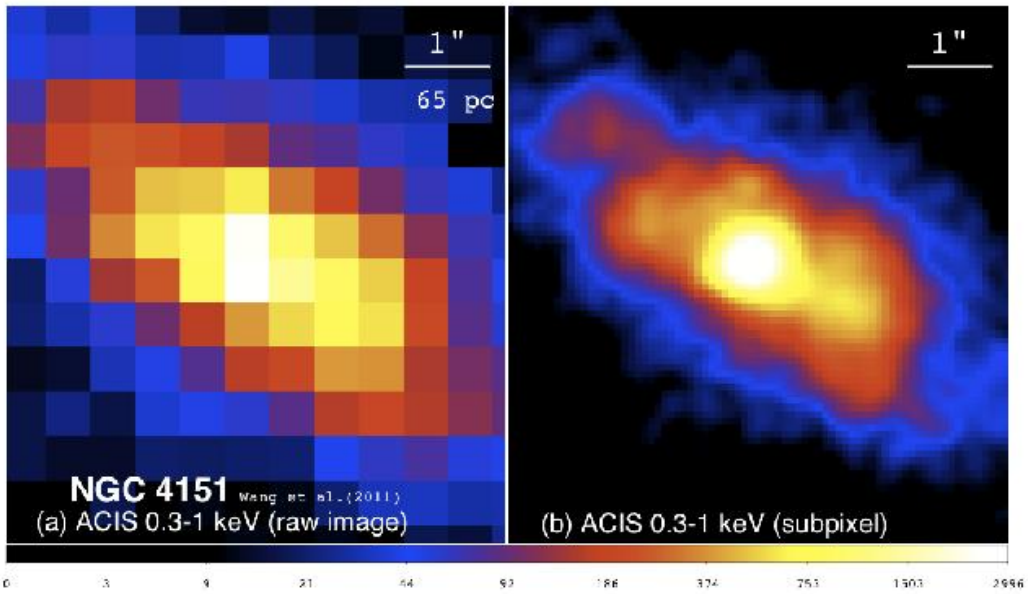

Figure 4.11: The core of NGC 4151 showing the comparison of the raw ACIS image (*left*) and subpixel sampling (1/8 native pixel size) using the EDSER algorithm (*right*). Adapted from Wang et al. (2011).

the proximity of the brightest jet region to the core, we opted to not use the VFAINT background cleaning. Overall, the difference it made in the background pixel counts was not large for our chosen energy range, and should be handled sufficiently using a background region and aperture photometry.

Though the ACIS detector is capable of collecting photons in the 0.1−10 keV range, we used a narrower energy filter of 0.3−7 keV because it is less affected by the quantum efficiency (QE) degradation in ACIS over time. QE is the fraction of incident photons detected by the CCD. It is thought that the ACIS detectors are being coated with some material(s) over time that decrease the QE (Chandra team, 2015). During the calibration steps, CIAO applies a correction for the modeled effect of QE with energy.

Once the level=2 event file is made, astrometry correction can be performed. The CIAO tasks `wavdetect`, `wcs_match`, and `wcs_update` were used for this purpose.

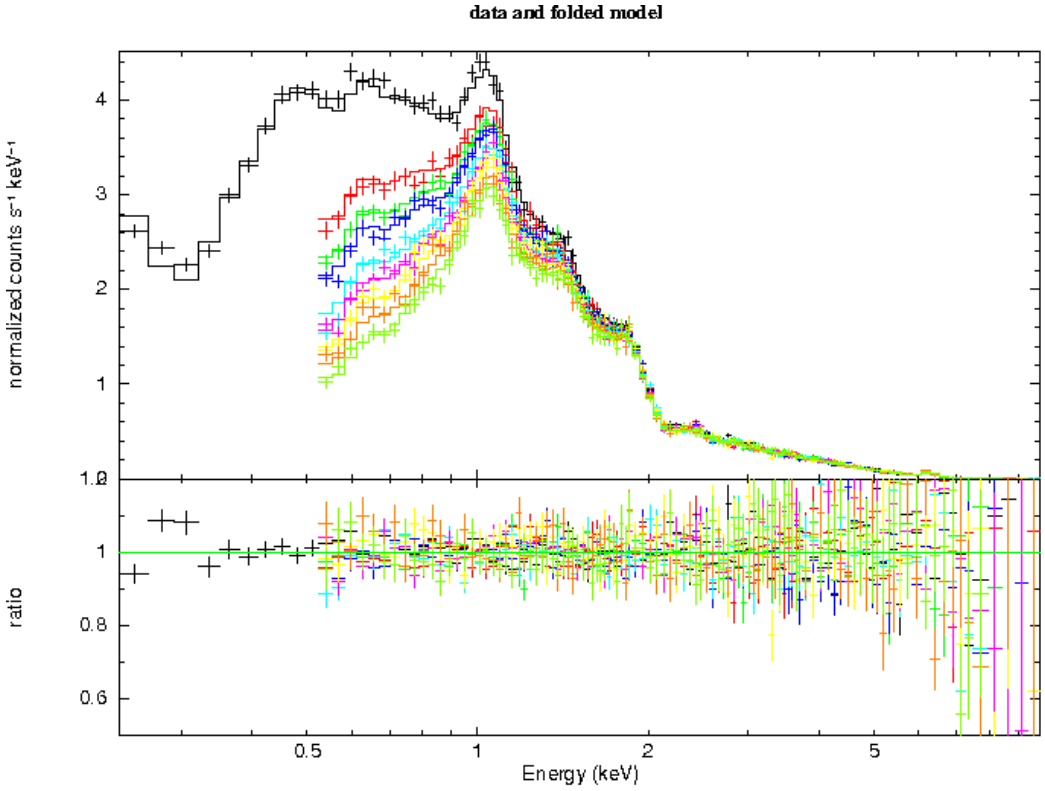

Figure 4.12: Fitted spectra from observations of A1759 (in 2000, 2002, 2004, 2005, 2009, 2010, 2011,2012 and 2013) showing the energy-dependent decrease in QE for the ACIS-S detector with time. Figure taken from `http://cxc.harvard.edu/ciao/why/acisqecontam.html`.

`wavdetect` is a task that statistically detects sources in the image. `wcs_match` is used to match the astrometry of detected X-ray sources with those in an external catalog, preferably one that has very good astrometry. The astrometry of the 2MASS catalog is ± 0.1 arcsec, a significant improvement over the *Chandra* absolute astrometry accuracy of ± 0.5 arcsec (Weisskopf et al., 2003). Since few sources in each image were available for matching, we excluded rotational corrections from being made. `wcs_update` was then used to apply the astrometry correction to the event file. The various exposures are then combined to form a final image using `merge_obs`.

The combined X-ray image for each jet was then smoothed to improve visual com-

parison using a Gaussian kernel over three pixels. Though normalized to conserve flux, smoothed images were not used to calculate photometry. To do photometry on *Chandra* images, spectra must be fit to source and background regions. This is discussed in §5.1.2.

4.4 Archival Data

4.4.1 3C 273

The archival radio data of the 3C 273 jet came from Perley & Meisenheimer (2017). The provided image library is made from Very Large Array (VLA) observations in all frequency bands, ranging from 73.8 MHz to 43 GHz, taken between 1987 and 1999. It provides intensity, fractional polarization, and position angle maps for all bands. For our direct comparison in figures used in this paper, we use the 8.4 GHz X band images.

The *Chandra* X-ray images used for 3C 273 were combined from archival observations (Jester et al., 2006).

The jet component fluxes published in Jester et al. (2007) were used in plotting the broadband SED for the jet (shown and discussed in Chapter 6) as well as SED modeling, in addition to our new data.

4.4.2 1150+497

For the 1150+497 jet, we used archival 1.66 GHz data from the Multi-Element Radio Linked Interferometer Network (MERLIN) (Sambruna et al., 2006a). The observations were taken in January 2002 and provide only the intensity map.

The jet component fluxes published in Sambruna et al. (2006a) were used in plotting the broadband SED for the jet (shown and discussed in Chapter 6) in addition to our

new data.

4.4.3 PKS 0637–752

For the PKS 0637–752 jet, we used archival 8.64 GHz images from the Australia Telescope Compact Array (ATCA) (Lovell et al., 2000). The observations were taken in August 1999 and provide only the intensity map.

The jet component fluxes published in Mehta et al. (2009) were used in plotting the broadband SED for the jet (shown and discussed in Chapter 6) in addition to our new data.

Chapter 5

Data Analysis

5.1 Aperture Photometry

This section describes the methods and tools used to determine the flux in each jet region, which differ considerably between optical (*HST*) and X-ray (*Chandra*).

5.1.1 Optical Photometry

Aperture photometry is a simple method of determining the counts (and therefore flux) in a source region wherein the number of observed counts in each pixel of a source region are summed up and the background sky contribution is removed. For each source region, background regions were chosen nearby to estimate the local source background. Determining the best size of the source region is an issue because a larger source size means more pixels from which the error contribution increases, leading to a smaller signal-to-noise ratio (SNR). Exclude regions were used to omit the counts from stars, galaxies and diffraction spikes in all source and background regions. Local background regions were chosen such that they contained a larger number of pixels

than the source region where possible.

However, the PSF from the source will be larger than the region used, meaning that some small amount of source flux is not being accounted for. The technique of aperture correction is used to account for this missing flux without adding in the noise from all the additional pixels outside the source region. In practice this is generally done using aperture growth curves (Howell, 1989), also known as encircled energy fractions. Bohlin (2016) provides the most recent photometric calibrations for the ACS/WFC instrument, including encircled energy fractions for different aperture radii[1]. The source apertures we use vary in size according to the size of each jet region, but typical aperture corrections for our data sets lie in the 4% – 8% range.

In addition to this, we compensated for the presence of the diffraction spike in our *Stokes I* image in the manner described in §4.2.2.1.

For drizzled and combined *HST Stokes I* images, the pixels had units of counts per second (count rate). This was done because, after drizzling and mosaicking, each pixel has a different effective exposure time. A Python script of our making was used to determine the background-subtracted count rate in each source region, which can then be converted into flux. The `pyregion` package and a custom script were used to convert the source, background, and exclude regions into pixel masks which could then be imported into `NumPy` arrays in Python using the `astropy` package (Astropy Collaboration et al., 2013). Sigma clipping was applied to the background pixel arrays to remove any outlier pixels that were missed by the exclude regions.

In the case of 1150+497, where galaxy subtraction was applied previously, some of the pixels had negative count rates, which obviously is not realistic. To rectify this,

---

[1] `https://www.stsci.edu/hst/instrumentation/acs/data-analysis/aperture-corrections`

in source/background regions where there were negative pixel values, we subtracted the minimum pixel value so that the minimum value would then become 0. This had no effect on the background-subtracted count rate, but does affect the uncertainty calculation. This is necessary because in some cases the total background counts could be negative, which is troublesome given that the CCD error equation involves taking the square root (due to Poisson statistics). From testing with sample arrays, this seemed the best method to determine the error for the galaxy-subtracted source regions. The issue of negative pixels is unavoidable when doing any sort of global sky subtraction, such as that performed by default by `AstroDrizzle`, though there appears to be no standardized method to deal with it.

The average count rate per pixel in the background region was determined by

$$\overline{DN}_{\rm sky} = \frac{DN_{\rm sky}}{n_{\rm B}}, \tag{5.1}$$

where $DN_{\rm sky}$ is the total number of counts per second ("data numbers") in the background region and $n_{\rm B}$ is the number of pixels in the background region. The total number of background-subtracted counts per second in a source region was then determined by

$$DN_* = \sum_{i=1}^{n_{\rm pix}} \left(DN_{\rm source,i} - \overline{DN}_{\rm sky} \right), \tag{5.2}$$

where $DN_{\rm source,i}$ is the count rate of a given pixel in the source region and $n_{\rm pix}$ is the number of pixels in the source region.

The background-subtracted count rate can then be converted into flux by

$$F_* = DN_* \cdot PHOTFLAM \cdot PHOTPLAM \quad [\text{erg s}^{-1}\ \text{cm}^{-2}], \tag{5.3}$$

where $PHOTFLAM$ (inverse sensitivity) and $PHOTPLAM$ (pivot wavelength) are

photometric calibration values found in the header of the drizzled image. Since we used the same filter for all *HST* observations, $PHOTPLAM = 5936.9736$ Å for all images. Header values of $PHOTFLAM(\text{3C 273}) = 3.0728759E{-}19$ [erg cm^{-2} Å^{-1} electron^{-1}], $PHOTFLAM(\text{PKS 0637-752}) = 3.0629278375E-19$ [erg cm^{-2} Å^{-1} electron^{-1}], and $PHOTFLAM(\text{1150+497}) = 3.04795653333333E-19$ [erg cm^{-2} Å^{-1} electron^{-1}] were used for their respective calibrations.

F_* is then multiplied by the aperture correction factor for the source region to get the total flux. This must then be corrected for extinction using the standard equation

$$A_\nu = -2.5 \log_{10} \left(\frac{F_*}{F} \right) \tag{5.4}$$

$$\Rightarrow F = 10^{\frac{A_\nu}{2.5}} F_* \tag{5.5}$$

(e.g., Schneider 2006), where A_ν is the wavelength-dependent extinction coefficient, F_* is the observed flux, and F is the extinction-corrected source flux. The extinction coefficients were taken from the NASA/IPAC Extragalactic Database (NED)[2]. The values used for F606W were: 0.051 for 3C 273, 0.237 for PKS 0637-752, and 0.056 for 1150+497.

To estimate the error in count rate (DN), first the count rate needed to be converted into counts. This was done by multiplying the pixel DN value by its associated weight map pixel (in the WHT extension of the drizzled image), the value of which is the calculated exposure time of that pixel. The uncertainty in source counts were then

[2] `http://ned.ipac.caltech.edu`

determined for each source region using

$$\sigma_{\mathrm{N}_*} = \sqrt{N_* + n_{\mathrm{pix}} \left(1 + \frac{n_{\mathrm{pix}}}{n_{\mathrm{B}}}\right) (N_{\mathrm{sky}} + N_{\mathrm{D}} + N_{\mathrm{R}}^2)} \tag{5.6}$$

(e.g., Howell 2006), where N_* is the total number of background-subtracted counts in the source region, N_{sky}, N_{D} and N_{R} are the total number of counts (or electrons) per pixel in the background, due to dark current, and due to read noise, respectively. The $(1 + n_{\mathrm{pix}}/n_{\mathrm{B}})$ term attempts to account for the noise introduced due to the relative size of the chosen background region. The median dark current was found in Lucas et al. (2021) and in the dark frame that corresponds to each image, while the average read noise was written to the header during calibration; both were corrected for the smaller (drizzled) pixel size. The error in source counts was then divided by the median exposure time per pixel in the source region to get the total error in source count rate. This was then converted into the error in flux as described above.

5.1.2 X-ray Photometry and Spectral Indices

The same source apertures were used for our X-ray aperture photometry as were used for the optical, to provide a direct comparison between bands. However, the process is quite different. Spectra were fitted to the observed X-ray data for each source region to calculate the flux.

Background aperture regions were chosen adjacent to each source region to account for the flux due to the AGN and sky. For the source regions that were particularly close to the core, an annulus region was used for the background.

Spectra were extracted from these regions using the CIAO task `specextract`. This task generates the Response Matrix Files (RMFs) and Ancillary Response Files (ARFs) for each source and background region, which are used in converting the information

Table 5.1: Jet Component X-Ray Spectra and Flux Densities

Jet	**Region**	$\mathbf{N_H}^a$	Γ_X	$\mathbf{F}_{1keV}(10^{-14}$erg s^{-1}cm$^{-2})$
1150+497	Knot B	2.1	1.84 ± 0.2	1.92
PKS 0637−752	Knot WK 7.8	0.5	1.62 ± 0.2	1.56

[a]Absorption column density (10^{21} cm^{-2}).

about the events into the energy. We altered the correctpsf parameter to apply aperture correction to the source regions (aperture correction is described further in §5.1.1). The energy range was set to 0.3−7 keV with an energy bin of 0.01 keV.

The *Sherpa* software package (Freeman et al., 2001) was used to fit models to our observed spectra. We used *XSpec* models contained in *Sherpa* to do the fits, namely *xspowerlaw* and *xsphabs*, which respectively model a photon power law fit and background photoelectric absorption. The Cash statistic (Cash, 1979) was chosen as our maximum likelihood function to assess the goodness of fit as it is a Poisson likelihood function, along with the Simplex (aka Nelder−Mead) fitting optimization method. Source and background spectra were modeled independently and no background-subtraction was performed, as is required when using the Cash statistic. Fits were done on unbinned data per the recommendation of Arnaud et al. (2011), over the 0.3−7 keV energy range.

Since we have many separate *Chandra* exposures, separate spectra must be made from each image separately – merged images lose their event information and cannot easily be used for spectroscopy or photometry.

The goodness-of-fit of each model was checked in two ways: first, by looking at the reduced statistic; and second, by running a simulation of the model and using the `plot_cdf` function to check that the cumulative distribution function[3] had a median

[3]`http://pysherpa.blogspot.com/2012/06/goodness-of-fit-with-cstatcash.html`

at about 0.5. The *xspowerlaw* model is of the power law

$$F_{\rm E} = KE^{-\Gamma}, \tag{5.7}$$

where E is the energy, Γ is the photon index and K is the normalization constant. The photon index Γ is related to the spectral index α such that $\alpha = \Gamma - 1$, where $F_\nu \propto \nu^{-\alpha}$ (Peterson, 1997). Figure 5.1 shows the model fit and residual for one of our images of 1150+497 (Knot B). The fitted spectral parameters for each source region are given in Tables 5.1. Errors in spectral index and normalization are given at 90% confidence intervals. Note that at this time we have only provided the model parameters for the brightest region in each jet. Both of these exhibit a photon index that is typical of jet regions.

The flux was determined using the `calc_energy_flux` function over a range of 0.3−7 keV; the flux density was determined at 1 keV. Simulations were used to determine the errors at 68% and 90% confidence intervals using the `sample_energy_flux` task.

5.2 Aperture Polarimetry

Stokes I, Q, and U images were created as described in §4.2.2.1, as were fractional polarization and electric vector position angle maps for each jet. To calculate the fractional polarization and position angle of an aperture, we must calculate the Stokes parameters again, where r_0, r_{60}, and r_{120} are each the sum of the counts (or count rates) in the source aperture rather than individual pixel values.

The uncertainty in each of the POL0V, POL60V, and POL120V filter images was assumed to be Poisson in nature, as these images are simply arrays of the count rates for each pixel, combined with the dark current and read noise as before. Gaussian error propagation is then used to calculate the uncertainties in the *Stokes I*, Q, and U

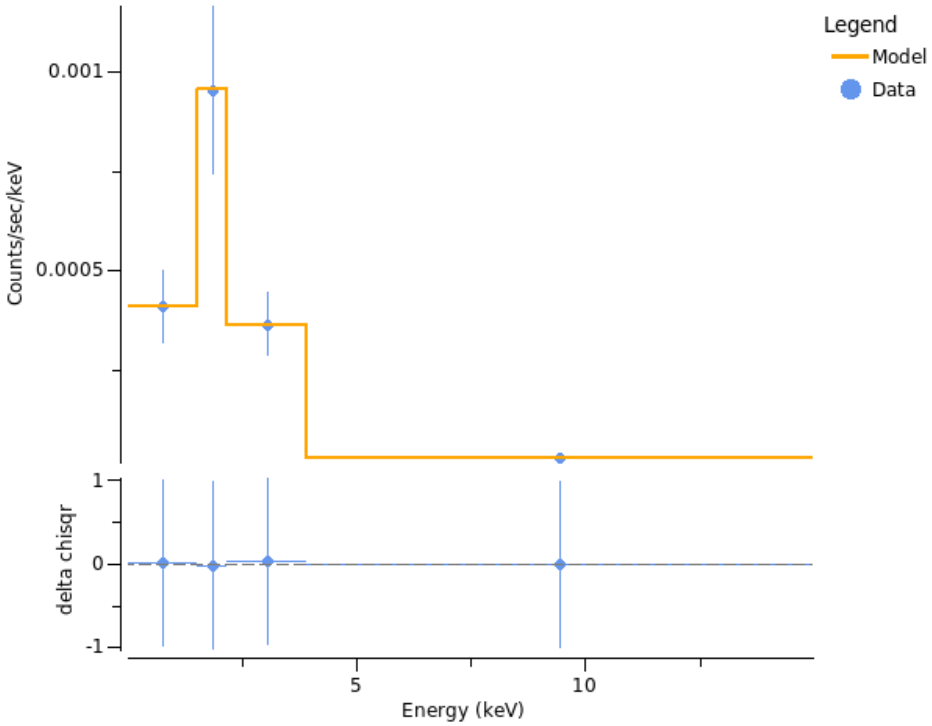

Figure 5.1: One of our spectral models and residuals fitted to a source and background region for the 1150+497 jet, Knot B. Events have been grouped into bins of 20 in this example.

values. This process is as described in Perlman et al. (2006); Cara et al. (2013). The `uncertainties` package in Python was used for the calculations, as it can calculate the error propagation steps (including correlated variable terms) alongside the equations themselves. Debiasing was then performed, and the uncertainties in P and PA were calculated as described in §4.2.2.1.

Additionally, Lucas et al. (2021) notes that there is an additional systematic instrumental error that must be added in quadrature with the propagated photon (and related) noise for the fractional polarization and position angle. They have measured the instrumental uncertainty for highly-polarized sources to be at a one-part-in-ten level for the fractional polarization and $\sim 3^\circ$ for the position angle for the ACS/WFC detector. These systematic errors have been added in quadrature to the calculated

uncertainties for each aperture and are included in the values given in tables 6.1, 6.2, and 6.3.

Note that we have included an "SNR" column in these tables which shows the SNR without the instrumental uncertainties included. While this is imperfect, we believe it provides a useful gauge of the "source" SNR, which is required to be high for reliable polarimetry measurements. In other words, the "SNR" column represents P/σ_P, whereas the uncertainties of P reported in the table are σ_P added in quadrature with the instrumental uncertainty, as discussed previously in this section.

Normal convention is for EVPA is be calculated such that 0° is north and increasing in the clockwise direction. Since our images have been rotated so that the jets are advancing to the right, we have displayed EVPA such that it will be parallel to the jet when EVPA $\approx 0°$ and perpendicular to the jet when its value is $\pm 90°$. The inferred magnetic field position angle will be perpendicular to the EVPA.

5.3 Modeling of the SED

We used the Compton Sphere suite[4] to generate models of synchrotron and inverse-Compton emission for Knot A in the 3C 273 jet. We used the published flux values from Jester et al. (2006) as well as our new optical and X-ray data points for the fitting. This knot is shown to have optical emission that falls on the high-energy spectral component and thus can be used to constrain the fits. For most of the knots, including the knots in the other two jets, the optical fluxes seem to connect to the low-energy radio SED component, giving us no constraints on fitting a model to the X-ray component.

The Compton Sphere program takes in several jet parameters (e.g., Doppler factor,

[4] `http://astro.umbc.edu/compton`

comoving luminosity, $\gamma_{\rm min}$, $\gamma_{\rm max}$, magnetic field strength) and computes the associated synchrotron and IC/CMB spectra. We wrote a Python wrapper to improve the usability of Compton Sphere by allowing it to generate many models at once over a range of values for each parameter. Each model was stored in an efficient HDF5 container (using the Python Data Analysis Library (pandas)). This allowed us to consider a wide range of parameters to determine the models that best fit our observations using χ^2 minimization.

Chapter 6

Results and Discussion

Our core result is that we find significant linear polarization in all optically-bright knots in all three jets. This is consistent with a synchrotron source of radiation within these jets as an explanation for the optical emission (a prediction we discussed in §2.2). Several polarized jet knots are shown to have optical emission that connects with the X-ray component, lending strong support to the second-synchrotron hypothesis.

The fractional polarization maps we have made allow us to view the magnetic field structure of FR II jet knots at a much higher resolution than previous studies of FR II jet polarimetry.

Below we will explain the points of interest that we find for each jet before summarizing the overall findings of the project.

6.1 3C 273

We find significant optical linear polarization in all knots throughout the length of the 3C 273 outer jet. Nearly every knot exhibits a fractional polarization of ∼10%+, with several regions of the jet reaching the ∼30%+ range. This is consistent with our

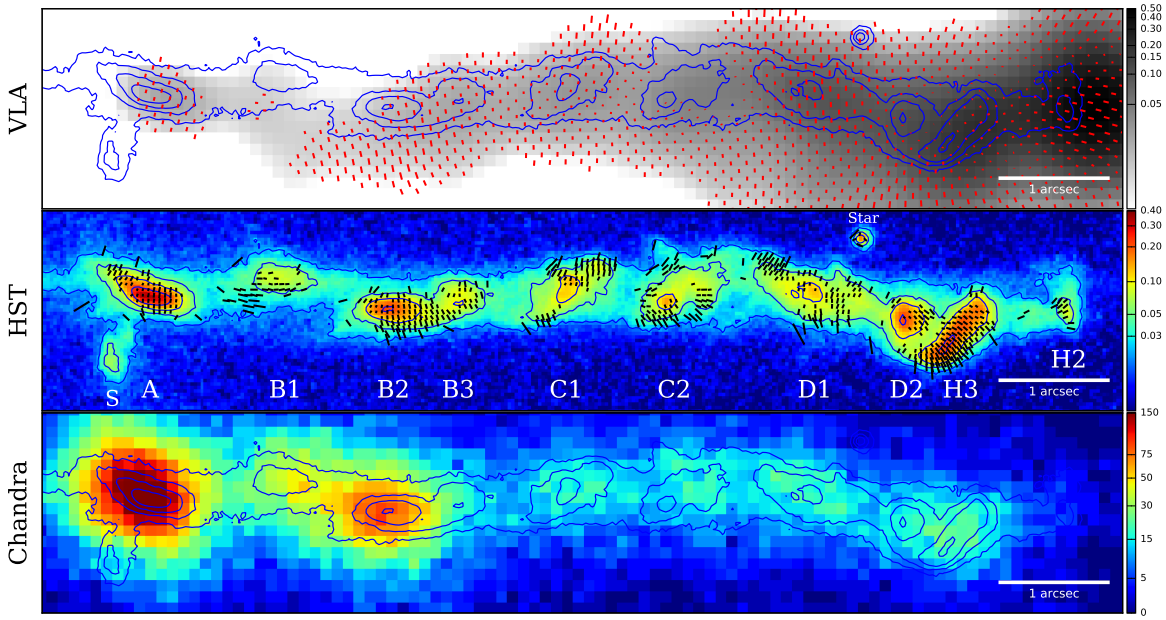

Figure 6.1: The outer jet of 3C 273 in multiple bands. *Top*: VLA 8.4 GHz radio image with polarization E-field vectors (SNR > 5.0, in red) and HST contours overlaid. *Middle*: Color *Stokes I* image using new *HST*/ACS+F606W data with blue contours and polarization E-field vectors overlaid (SNR > 3.5, in black). *Bottom*: Color Chandra X-ray flux image with HST/ACS *Stokes I* contours overlaid. E-field vectors show the orientation of the plane of linear polarization, with their lengths being proportional to the degree of polarization, scaled such that 0.2 arcsec = 100% polarization. The inferred magnetic field direction is perpendicular to the plotted E-field vectors. Stark differences are seen between the radio and optical, both in flux and polarization.

expectation of synchrotron emission.

Figure 6.1 shows a multiwavelength view of the 3C 273 outer jet, including our new *HST* fractional polarization map. In all images that display polarization vectors, the E-vectors are shown (using the EVPA). The E-vector represents the orientation of the plane on which the electric field of the polarized photons oscillate. The magnetic field direction of the emitting region can be inferred to be perpendicular to this. Table 6.1 gives the value of the fractional polarization of each jet knot using aperture polarimetry. The fractional polarization is indicative of the degree of ordering of the magnetic field in each emitting region. Figure 6.2 shows the fractional polarization for certain highly-

Table 6.1: 3C 273 Optical Jet Polarization and Flux Densities

Knot	**P (%)**	**S/N**[a]	**EVPA**[b] (°)	$\mathbf{F_\nu}$[c](μ**Jy**)
A	13.0 ± 1.3	39.4	79 ± 3	4.83 ± 0.05
B1	12.4 ± 1.4	20.1	15 ± 3	1.79 ± 0.02
B2	16.0 ± 1.7	38.1	−81 ± 3	3.76 ± 0.04
B3	13.7 ± 1.5	19.7	−79 ± 3	1.29 ± 0.01
...	9.3 ± 1.3	10.2	−78 ± 4	0.82 ± 0.01
C1	13.3 ± 1.4	28.1	82 ± 3	2.77 ± 0.03
C2	7.3 ± 0.9	15.4	−31 ± 4	3.03 ± 0.03
D1	13.8 ± 1.5	31.0	82 ± 3	2.77 ± 0.03
D2	4.0 ± 0.6	9.3	−64 ± 4	2.49 ± 0.02
H3	19.6 ± 2.0	60.8	−50 ± 3	4.33 ± 0.04
D2H3 (combined)	11.6 ± 1.2	40.3	−56 ± 3	6.82 ± 0.07
H2	13.8 ± 1.8	12.5	30 ± 4	0.49 ± 0.01
Total Jet[d]	6.6 ± 0.7	40.9	−83 ± 3	–

[a]Signal-to-noise ratio is calculated without the inclusion of instrumental systematic error (see §5.2). [b]EVPA is oriented such that it will be perpendicular to the jet when its value is ±90°. Inferred magnetic field vector is +90° from EVPA. [c]F606W flux density at 5.05E14 Hz. [d]Including all optical emission from Knot A to H2.

polarized regions that do not coincide with flux maxima. Figure 6.3 shows a more clear picture of the optical fractional polarization along the jet on a per-pixel basis.

Every knot in the jet is seen to be narrower in the optical than it is in the radio. This is shown in the multiwavelength images and explicitly shown with jet width profiles in Figure 6.7. This is consistent with our expectation of a spine-sheath structure within the jet, wherein the spine, being insulated from interaction with the ISM and IGM, has a more relativistic velocity than the sheath. An important note is that we have not deconvolved the *Chandra* image, so the width of the jet in these images is not physical, instead it is due to the large *Chandra* PSF. Marchenko et al. (2017) has performed the X-ray deconvolution and found the width of the X-ray knots to be comparable to that of the optical. Our optical images are also affected by the *HST*/ACS/WFC PSF with ideal FWHM≈0.1 arcsec. There is some smoothing in the radio given the clean beam of FWHM=0.35 arcsec. An ideal comparison would require new high-resolution JVLA

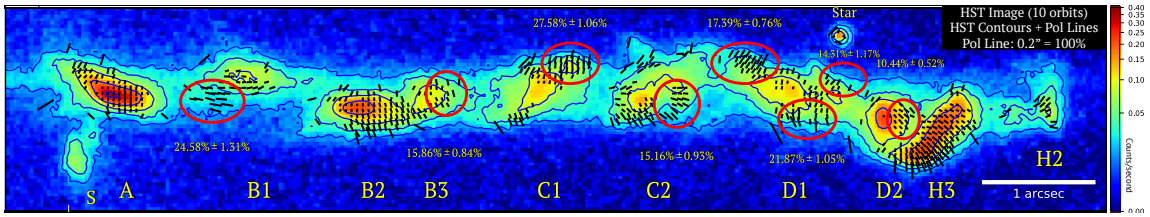

Figure 6.2: The outer jet of 3C 273, color *Stokes I* image using new *HST*/ACS+F606W data with blue contours and polarization E-field vectors overlaid (SNR > 3.5, in black). These E-field vectors show the orientation of the plane of linear polarization, with their lengths being proportional to the degree of polarization, scaled such that 0.2 arcsec = 100% polarization. The inferred magnetic field direction is perpendicular to the plotted E-field vectors. Circled regions show the fractional polarization of areas of certain areas of interest.

radio imaging, however the current data is sufficient and the narrower optical knots are consistent with the data.

6.1.1 Jet Morphology

Knot A: Optical and radio polarimetry are consistent and show the magnetic field direction to be parallel to the jet throughout the knot. The optical polarization becomes significant earlier (upstream) in the knot than does the radio. This may be due to the frequency of our available radio observations; probably, there is significant radio polarization in the upstream region that is below the energy at which we observe.

The peak optical flux in the knot is correlated with the radio and X-ray and coincides with the local minimum of fractional polarization. This characteristic is seen in many jet knots, including several in the optical jet of M87 (Perlman et al., 1999; Avachat et al., 2016). Given the lack of other high-resolution and high-SNR FR II jet polarimetric observations, we must compare our findings with studies of the FR I jets.

The SED of Knot A (in Figure 6.5) shows that our optical F606W observations are connected to the same spectral energy component as the X-rays, and not the radio.

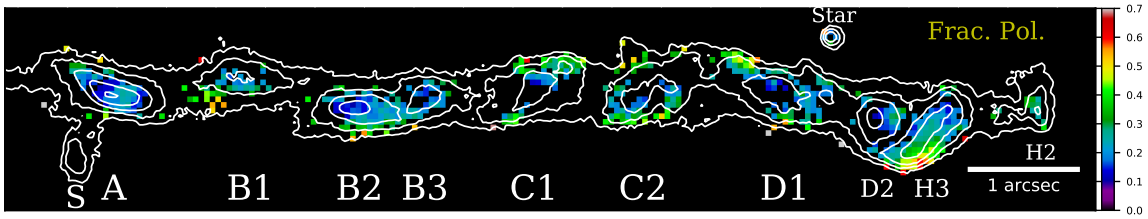

Figure 6.3: The outer jet of 3C 273, showing the optical linear fractional polarization per pixel (where polarization SNR > 3.5) along the jet, with *HST*/ACS+F606W *Stokes I* contours overlaid.

Given the SED, the optical would seem to be dominated by this high-energy spectral component. The presence of highly-polarized emission (P≈13%) strongly favors the two-component synchrotron model to explain the SED for Knot A, and rules out IC/CMB as an explanation as such emission would be unpolarized. This adds to the weight of evidence (discussed in §3.1) that for Knot A the optical–X-ray emission is synchrotron in nature radiating from a second, high-energy population of electrons within the region. This requires very efficient particle acceleration within the jet at ∼35 kpc away from the central engine of the AGN.

We attempted to model the high-energy SED synchrotron component for Knot A using the method discussed in §5.3, shown in Figure 6.6. This is a preliminary effort and can likely be improved in the future. The parameters of our preliminary best-fit model are: magnetic field strength $B = 3.75 \times 10^{-5}$ G, $\gamma_{min} = 1 \times 10^3$, $\gamma_{max} = 2 \times 10^9$.

Knot B1: Like Knot A, the SED of Knot B1 shows the optical F606W flux to be dominated by the second spectral component which connects to the X-rays. The overall polarization of B1 is significant (P≈12%) and provides strong evidence that the optical–X-ray component of the SED is synchrotron in nature by a high-energy population of accelerated electrons.

The fractional polarization is seen to be at a local minimum at the location of the

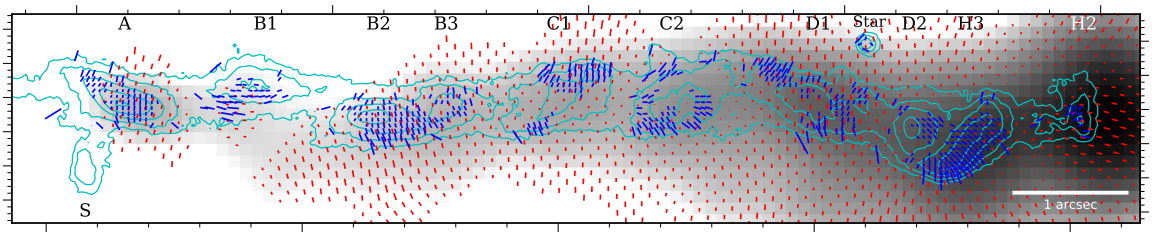

Figure 6.4: The outer jet of 3C 273, showing a more direct comparison of optical and radio polarization. Grayscale image is VLA 8.4 GHz, with *HST*/ACS+F606W *Stokes I* contours overlaid. Radio polarization E-vectors (SNR $>$ 3.0, in red) and optical polarization E-vectors (SNR $>$ 3.5, in blue) also shown. These E-field vectors show the orientation of the plane of linear polarization, with their lengths being proportional to the degree of polarization, scaled such that 0.2 arcsec = 100% polarization. The inferred magnetic field direction is perpendicular to the plotted E-field vectors. Note the significant differences between radio and optical polarization in Knots A, B1, D2 and the low-polarization channel through C1, C2, D1. Also note the significant curve in the radio jet between Knots B1 and B3.

optical maximum. The X-ray flux peaks at the downstream end of the knot. Note that while our 8.4 GHz radio image shows no significant flux at the optical flux peak of B1, the 14.9 GHz and 22.4 GHz radio images (published in Perley & Meisenheimer 2016, not shown here) do. Their fluxes are included for Knot B1 in the SED panel in Figure 6.5. However the flux morphology of all bands of radio differ significantly from that of the optical/X-ray.

Optical polarimetry shows the magnetic field direction to be perpendicular to the centerline of the optical jet, from a region upstream of B1 through its flux maxima. The radio polarization correlates with the optical here, however with the optical exhibiting a significantly higher fractional polarization.

The upstream portion of B1 shows highly-polarized optical emission along the edge of the optical jet (P$\approx$25%, see Figures 6.2 and 6.3), which coincides with where the radio jet appears to bend. This pattern of high polarization along the optical jet edge has been seen before in other jets, including the outer jet of M87 (Perlman et al., 1999;

Avachat et al., 2016).

As can be seen in the images and quantified in Figure 6.7, the jet width profile of the radio emission of Knot B1 is significantly off-center, due to the large bend that begins in this region.

Knot B2: Like Knots A and B1, the SED of Knot B2 shows the optical F606W flux to be dominated by the high-energy spectral component which connects to the X-rays. The B2 knot is highly polarized (P≈16%), which provides strong evidence that the optical–X-ray component of the SED is synchrotron radiation from a high-energy population of accelerated electrons.

Knot B2 exhibits a minimum in fractional polarization coinciding with the flux maxima in the radio, optical and x-ray bands.

The magnetic field direction throughout B2 is parallel with the optical jet and coincides with the radio. Like B1, B2 also exhibits a noticeable increase in polarization along the southern edge of the optical jet. The radio jet continues to be misaligned from the optical jet after the bend at B1. This is again quantified by the jet width profiles in Figure 6.7, showing the transverse distribution of jet emission to be asymmetric.

Knot B3: At Knot B3 we again see a polarization minimum at the flux maximum in radio, optical, and X-ray bands. The optical polarization is significant along the southern edge and the downstream portion of the knot. The polarization of the downstream emission is measured to be P≈16% (Figure 6.2). The SED shows the optical emission to be connected to the radio spectral component for B3.

Knot C1: Here we see a significant divergence in the magnetic field structure than in previous jet regions. A channel of very low optical polarization extends from the region upstream of C1, through the center of the C1 knot and its flux maximum, and continuing all the way to the flux maximum of Knot D1. To reiterate, the fractional polarization we are measuring is indicative of how well-ordered the magnetic field is in

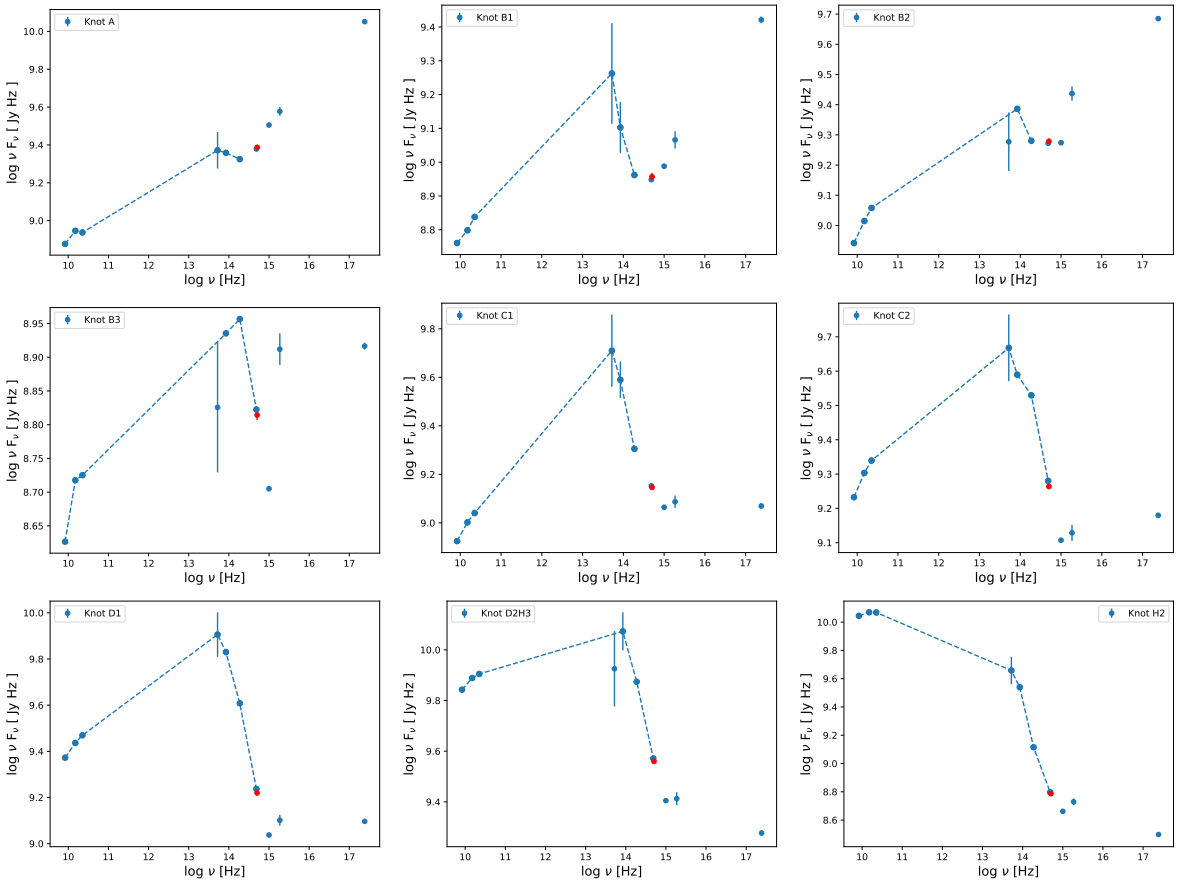

Figure 6.5: Broadband SED plots of the 3C 273 outer jet regions. Flux points in blue are referenced from Jester et al. (2007); those in red are measured from our *HST*/ACS+F606W *Stokes I*, with values listed in Table 6.1. Radio-IR fluxes have been naively connected between associated data points of the first synchrotron component, this is not meant to represent the actual shape of the SED component. Note that the F606W flux for several regions is shown to be part of the same SED component as the X-rays (e.g. Knots A, B1, B2) and exhibit significant linear polarization with high SNR.

those areas. A channel of such low polarization through the center of the jet is thus indicative of a disordered magnetic field in those areas. The low-polarization channel extends for ∼2.9 arcsec (a projected distance of just under 8 kpc).

The north and south edges of Knot C1 are highly polarized in the optical, significantly more than in the radio. The region of the northern edge shows a polarization of P≈28% (Figure 6.2) with the magnetic field orientated parallel with the optical jet.

The SED shows the optical emission to be connected to the radio spectral component for C1.

Knot C2: Again we see low optical and radio polarization at the optical flux maximum of the knot. The radio flux is dispersed and does not show a maximum in the knot, while the X-ray flux is also dispersed through the knot, with the peak flux happening downstream from the optical.The SED shows the optical emission to be connected to the radio component for C2.

Again the north and south edges of the optical knot exhibit high optical polarization, with the southern edge polarized to P≈15%. The channel of very low polarization continues through the knot to the flux maximum of D1. While the magnetic field direction along the south edge is parallel with the optical jet, that of the northern edge is perpendicular to the jet axis.

Knot D1: We see low optical and radio polarization at the optical flux maximum. This is where the low-polarization channel ends. The X-ray emission is dispersed evenly along the length of the knot. The SED shows the optical emission to be connected to the radio component for D1.

We see high polarization along the optical jet edges. Upstream of D1 is a large region with P≈17%. Just downstream of the flux maximum we see P≈22% on the southern edge and P≈14% on the northern edge along the optical jet.

Knot D2: Again we see low polarization in both the radio and optical coinciding

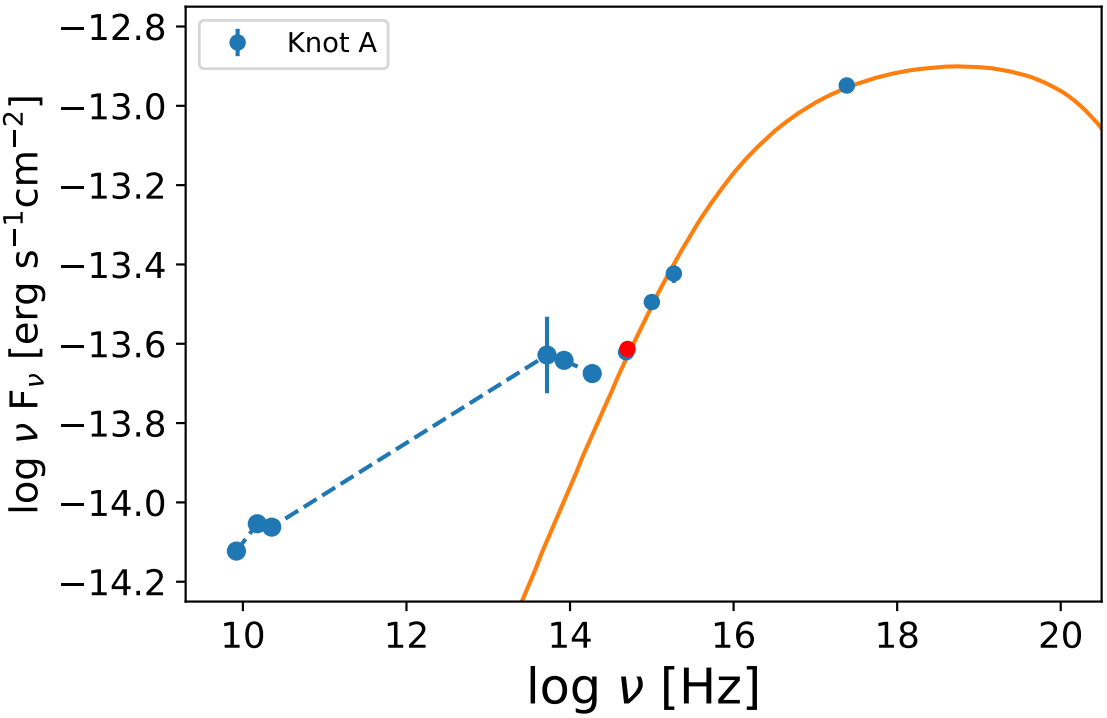

Figure 6.6: Preliminary SED model fit to the data of the broadband SED of Knot A of the 3C 273 jet. See §5.3 for details of the modeling process and §6.1.1 for the parameters used. It is apparent that the polarized emission we detect in our F606W image lies on the second emission component, thus strongly favoring a synchrotron source for the optical-to-X-ray flux.

with the flux maximum in the knot. However, the downstream sub-region of Knot D2 shows a stark difference in linear polarization between the radio and optical (see Figures 6.4 and 6.2). That particular sub-region shows a high SNR in the optical with fractional polarization of P≈10%, while the radio polarization is $\sim 1\%$ with the pixels in the center of the sub-region being below the SNR>3.0 cutoff that Perley & Meisenheimer (2017) used when creating the map. The magnetic field direction also changes to become perpendicular to the upstream flow.

This very significant mismatch between the radio and optical polarization may be evidence of particle populations that are differently placed along the line of sight

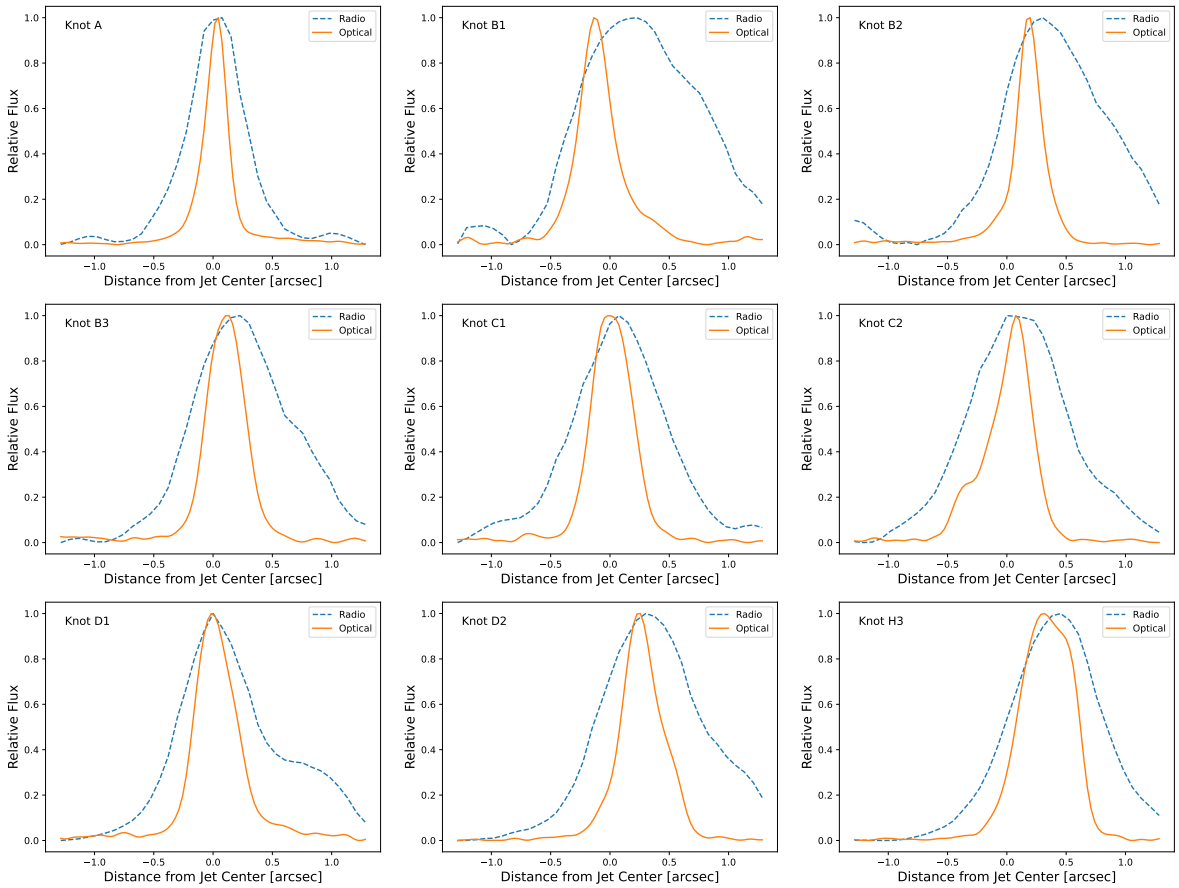

Figure 6.7: 3C 273: Relative flux profile of all jet knots in the direction perpendicular to the jet (as measured from the centerline of the first component to the hotspot), with fluxes from smoothed 8.4 GHz VLA radio and *HST*/ACS+F606W optical images. An emission profile that is narrower in the optical and/or X-ray than the radio could be evidence for the spine-sheath model of jet structure. Note the offset between radio and the other bands in Knot B1, where the radio emission profile is significantly misaligned (see Figure 6.4 as well).

through the jet emitting at different energies (as suspected in the case of M87 (Perlman et al., 1999; Avachat et al., 2016)).

Knot H3: The H3 knot exhibits a significant increase in flux compared to upstream regions (excepting Knots A and B2), and a very high degree of polarization. The entire H3 region averages a polarization of P≈20%, with its southern edge exhibiting polarization sub-regions of 40%+ (refer to Figure 6.3). This coincides with the location of the X-ray flux as well. The H3 region is significantly different from the upstream regions, showing high optical polarimetry coinciding with flux maxima, though the radio polarization is low. Most likely, H3 is a site of particle acceleration caused by a shock, perhaps with the optical jet interacting with the external medium.

Knot H2: This region is the radio hotspot where the radio emission reaches its maximum. Optical flux is also seen, though to a lesser degree, and is significantly polarized at P≈14%. Particle acceleration in this region is caused by Fermi acceleration in a so-called "planar shock" which explains the offset between optical and radio flux maxima (Meisenheimer & Heavens, 1986).

6.2 PKS 0637–752

We find a high degree of optical linear polarization in all optically-bright knots of the PKS 0637–752 jet, with the largest degree of polarization being P≈33%. This is indicative of synchrotron radiation being responsible for the observed optical flux.

As discussed in §3.2, the PKS 0637−752 jet has long been considered an ideal test case for the IC/CMB emission prediction in quasar jets. This is due to its relatively high redshift, $z = 0.651$, combined with the apparent energy density of the CMB $\propto (1+z)^4$.

Figure 2.4 shows our new *HST* and *Chandra* images and fractional polarization

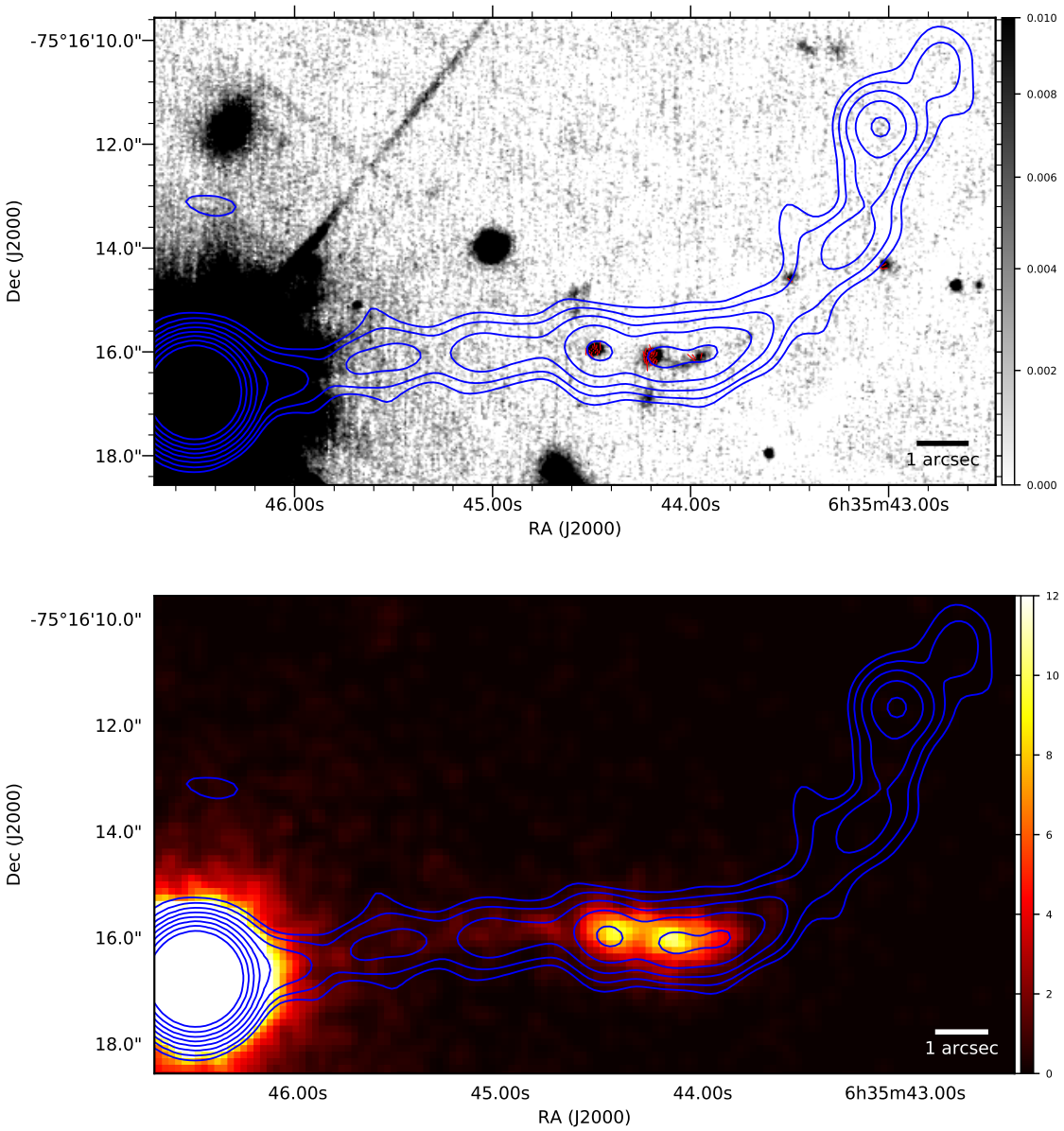

Figure 6.8: The nucleus and approaching jet of PKS 0637−752, with 8.64 GHz ATCA radio contours overlaid. *Top*: Optical *HST*/ACS+F606W *Stokes I* image, with optical polarization E-field vectors overlaid (SNR > 3.0, in red). These E-field vectors show the orientation of the plane of linear polarization, with their lengths being proportional to the degree of polarization, scaled such that 0.2 arcsec = 100% polarization. The inferred magnetic field direction is perpendicular to the plotted E-field vectors. *Bottom*: *Chandra* ACIS-S X-ray image (0.3–7 keV, smoothed) using our new observations.

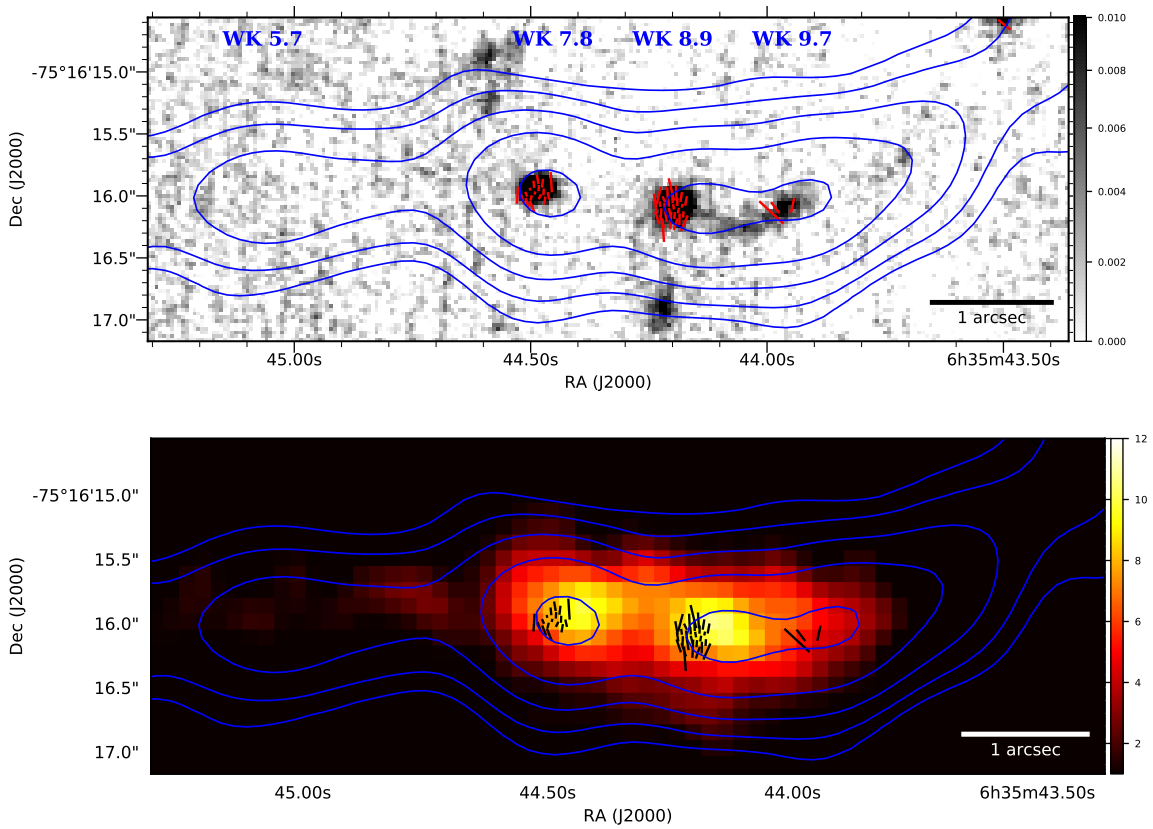

Figure 6.9: Bright optical–X-ray knots of PKS 0637−752, with 8.64 GHz ATCA radio contours overlaid. *Top*: Optical *HST*/ACS+F606W *Stokes I* image, with optical polarization E-field vectors overlaid (SNR > 3.0, in red). These E-field vectors show the orientation of the plane of linear polarization, with their lengths being proportional to the degree of polarization, scaled such that 0.2 arcsec = 100% polarization. The inferred magnetic field direction is perpendicular to the plotted E-field vectors. *Bottom*: *Chandra* ACIS-S X-ray image (0.3–7 keV, smoothed) with the same optical E-vectors overlaid (in black).

Table 6.2: PKS 0637−752 Optical Jet Polarization and Flux Densities

Knot	**P (%)**	**S/N**[a]	**EVPA**[b] (°)	$\mathbf{F}_\nu^c$**(nJy)**
WK 5.7	14.7 ± 10.0	1.5	−70 ± 17	<16
WK 7.8	18.7 ± 2.8	9.1	87 ± 4	166 ± 5
WK 8.9	33.1 ± 3.7	21.5	94 ± 3	223 ± 7
WK 9.7	13.4 ± 4.9	2.9	−68 ± 10	87 ± 3
Hotspot	16.9 ± 9.9	1.7	−35 ± 15	25 ± 2

[a]Signal-to-noise ratio is calculated without the inclusion of instrumental systematic error (see §5.2). [b]EVPA is oriented such that it will be perpendicular to the jet (before the bend) when its value is ±90°. Inferred magnetic field vector is +90° from EVPA. [c]F606W flux density at 5.05E14 Hz. 2σ upper limit for WK 5.7.

map, with radio flux overlaid. Table 6.2 gives the fractional polarization value for each of the three knots that are bright in the optical; Figure 6.10 shows just the fractional polarization values for the same region. The X-ray emission in the bright knots is clearly a separate SED component from the radio (Figure 2.2) and coincides with the highly polarized optical emission.

6.2.1 Jet Morphology

Knot WK 5.7: Detected in the radio and X-ray, the optical flux is below the threshold for detection, as seen in Figure 6.9. The X-ray flux does not have a distinctive maximum in the region. The polarization is measured at P≈15%, though with a SNR of just 1.5.

Knot WK 7.8: Optically bright knot with the flux maximum coinciding between radio, optical, and X-rays. Unlike the 3C 273 jet, we see significant polarization throughout the bright region of optical emission. The magnetic field direction is parallel with the jet. The optical knots are significantly narrower than the radio, as seen in Figure 6.12. This again is evidence for a spine-sheath model of jet structure, where the inner spine is moving at a faster relativistic speed than the sheath.

The SED of WK 7.8 is shown in Figure 6.11. Our F606W optical flux falls on the

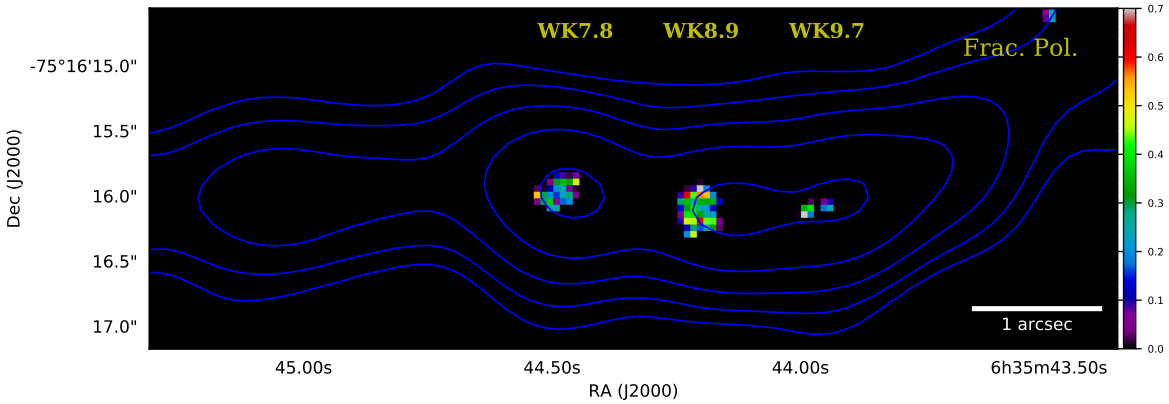

Figure 6.10: Bright optical–X-ray knots of PKS 0637−752, with 8.64 GHz ATCA radio contours overlaid, showing the optical linear fractional polarization per pixel (where polarization SNR > 3.0).

low-energy component that connects the radio. We also calculated the X-ray flux and spectral index of WK 7.8 using the methods described §5.1.2. Measuring the 1 keV flux density using the archival *Chandra* data and our new data, we find only a ∼4% difference which is within the uncertainties of both measurements. We also measure an 11% increase in the X-ray spectral index, from $\Gamma \approx 1.46$ to $\Gamma \approx 1.62$; this is on the bounds of the 90% uncertainties for both measurements. This is a preliminary result and more work will need to be done to measure the X-ray variabilities to a high degree of accuracy.

Knot WK 8.9: As with WK 7.8, the radio, optical, and X-ray flux maxima coincide with one another and coincide with a high degree of linear polarization. The linear polarization of the region is measured to be P≈33% with a high SNR. The magnetic field direction is parallel with the jet.

Knot WK 9.7: Bright in the optical and coinciding with X-ray and radio flux. The linear polarization is measured to be P≈13%, though with a SNR of only 2.9. A large bend in the radio jet occurs just downstream of WK 7.9 and no optical or X-ray

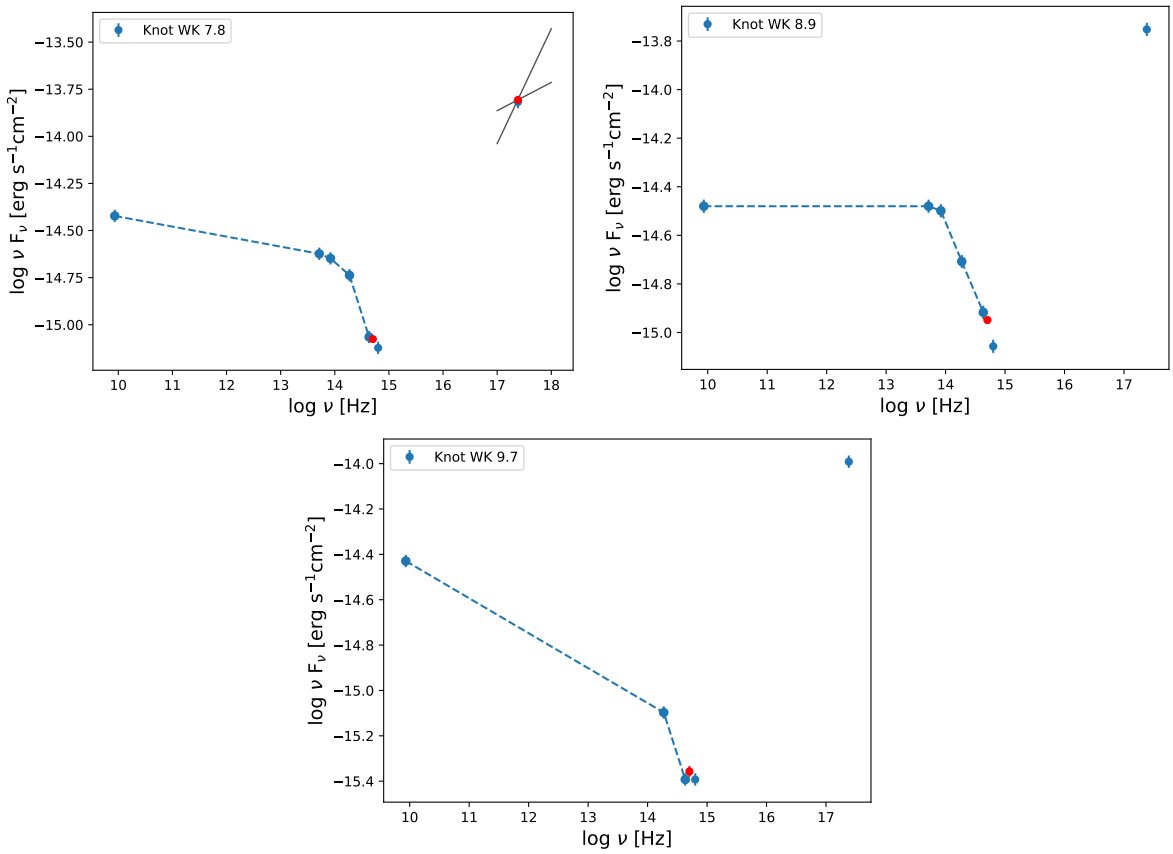

Figure 6.11: Broadband SED plots of the PKS 0637−752 jet regions which have significant optical–X-ray flux. Flux points in blue are referenced from Mehta et al. (2009); those in red are new measurements from *HST*/ACS+F606W *Stokes I* with values listed in Table 6.2, with *Chandra* X-ray (1 keV) flux and spectral index (90% uncertainties, Table 5.1) shown for Knot WK 7.8. Radio-IR fluxes have been naively connected between associated data points of the first synchrotron component, this is not meant to represent the actual shape of the SED component. Knots WK 7.8, WK 8.9, and WK 9.7 exhibit significant linear polarization with high SNR.

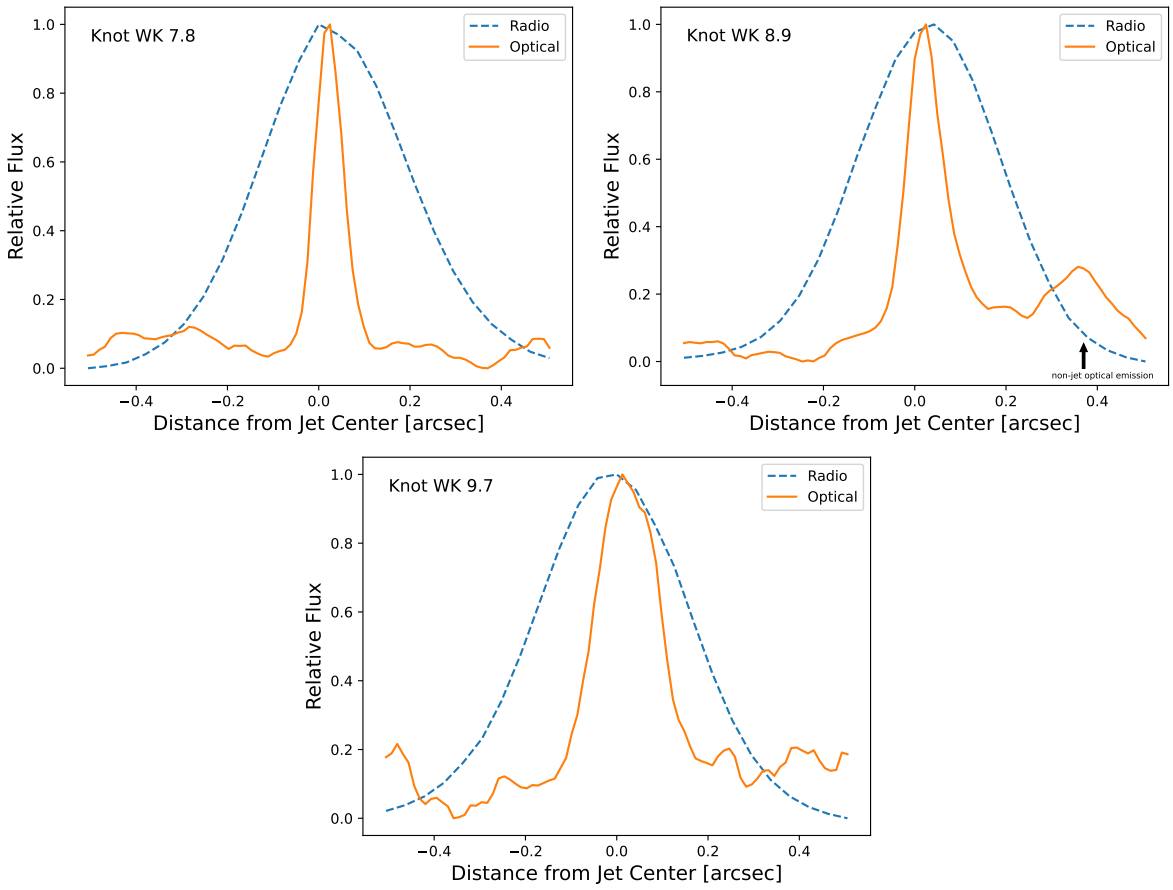

Figure 6.12: PKS 0637−752: Relative flux profile of several jet knots in the direction perpendicular to the jet, with fluxes from 8.64 GHz ATCA radio and *HST*/ACS+F606W optical (smoothed) images. An emission profile that is narrower in the optical and/or X-ray than the radio could be evidence for the spine-sheath model of jet structure.

emission is seen after the bend (see Figure 6.8). The reason for the lack of high-energy emission is an open question, though one possibility is that the jet is bent away from us as well as to the North. This would cause the relativistic flow of the jet to be more beamed away from us and de-boost the optical/X-ray radiation at our viewing angle.

Lovell et al. (2000) has published a 4 Ghz ATCA radio fractional polarization map of the PKS 0637−752 jet. Though low resolution, it shows the magnetic field direction to be parallel along the jet until the bend. At the bend, no polarization is detected. The polarization after the bend and downstream to the radio hotspot is significant, the magnetic field direction is perpendicular to the jet.

6.3 1150+497

We detect significant optical linear polarization in the optically-bright knots of 1150+497, though only one with high SNR.

6.3.1 Jet Morphology

Knot B: The polarization of Knot B is measured to be P≈8% with a high SNR. The radio, optical, and X-ray maxima all peak in the same location at the center of Knot B. It also is the location of a bend in the jet (see Figures 6.13).

The magnetic field orientation is roughly parallel with the jet before the bend (though not entirely), and rotates at the flux maximum to become parallel with the jet as it moves downstream. This is a characteristic signature of an oblique shock which has been found at the bends of other jets (e.g., Dulwich et al. 2009). Figures 6.14 and 6.15 for visualizations of the change in P and PA in this region.

We also measured the X-ray flux in Knot B in both the archival and new *Chandra* data sets (SED shown in Figure 6.16). We find the variability in the X-ray flux to be

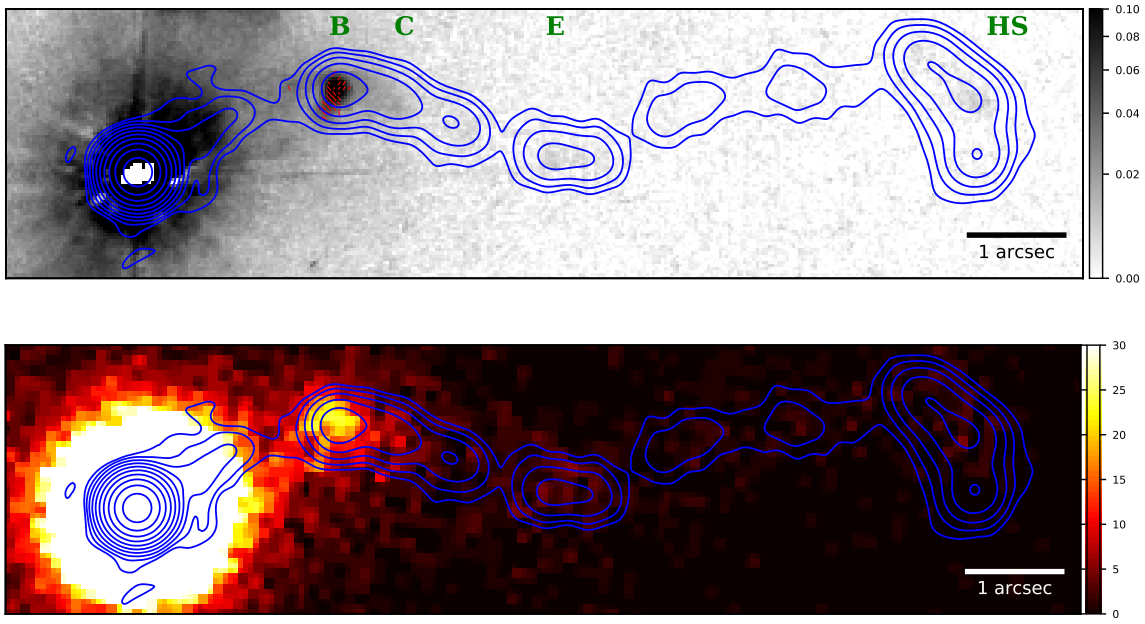

Figure 6.13: The nucleus and approaching jet of 1150+497, with 1.66 GHz MERLIN radio contours overlaid. *Top*: Optical *HST*/ACS+F606W *Stokes I* image, with optical polarization E-field vectors overlaid (SNR > 4.0, in red). These E-field vectors show the orientation of the plane of linear polarization, with their lengths being proportional to the degree of polarization, scaled such that 0.2 arcsec = 100% polarization. The inferred magnetic field direction is perpendicular to the plotted E-field vectors. *Bottom*: *Chandra* ACIS-S X-ray image (0.3–7 keV) using our new observations.

∼9% and the spectral index to be ∼10% using the same source and background regions. This is a preliminary result and care will need to be taken to minimize uncertainties when testing for variability.

Knot C: Just downstream of Knot B is Knot C, also with significant optical and X-ray flux. The distribution of emission throughout C is dispersed rather than flaring at a single point. Polarization is measured at P≈5, though with a SNR of only 4.3.

Knot E: Measuring an accurate optical flux for Knot E was complicated by the presence of a diffraction spike from the quasar. We modeled and subtracted it as described in §4.2.2.2, however the emission is still near the background level. Our

Table 6.3: 1150+497 Optical Jet Polarization and Flux Densities

Knot	**P (%)**	**S/N**[a]	**EVPA**[b] (°)	$\mathbf{F}_\nu^c$**(nJy)**
B	8.3 ± 1.0	16.0	−58 ± 4	823 ± 25
C	5.0 ± 1.3	4.3	60 ± 7	198 ± 6
E	11.5 ± 6.1	1.9	56 ± 14	97 ± 10
Hotspot	8.0 ± 4.7	1.8	78 ± 15	<66

[a]Signal-to-noise ratio is calculated without the inclusion of instrumental systematic error (see §5.2). [b]EVPA is oriented such that it will be perpendicular to the jet when its value is ±90°. Inferred magnetic field vector is +90° from EVPA. [c]F606W flux density at 5.05E14 Hz. 2σ upper limit for the hotspot.

measured polarization is P≈12% with an SNR of 1.9. Another bend occurs at Knot E, this time with no optical or X-ray flaring, though the radio emission does peak. Presumably this would involve the same type of physics that the oblique shock in Knot B exhibited. Perhaps the orientation of the jet by the time it reaches Knot E prevents us from seeing the emission from such a shock.

All knots for which we have constructed SEDs (Figure 6.16) show that our new optical F606W observations are part of the low-energy radio spectral component.

Only one optical knot has polarization detected at SNR > 10. The polarization map shows a stark 90° change in the direction of the inferred magnetic field across the optical flux maximum of the knot. Much less-polarized (∼5%) optical emission is detected just downstream.

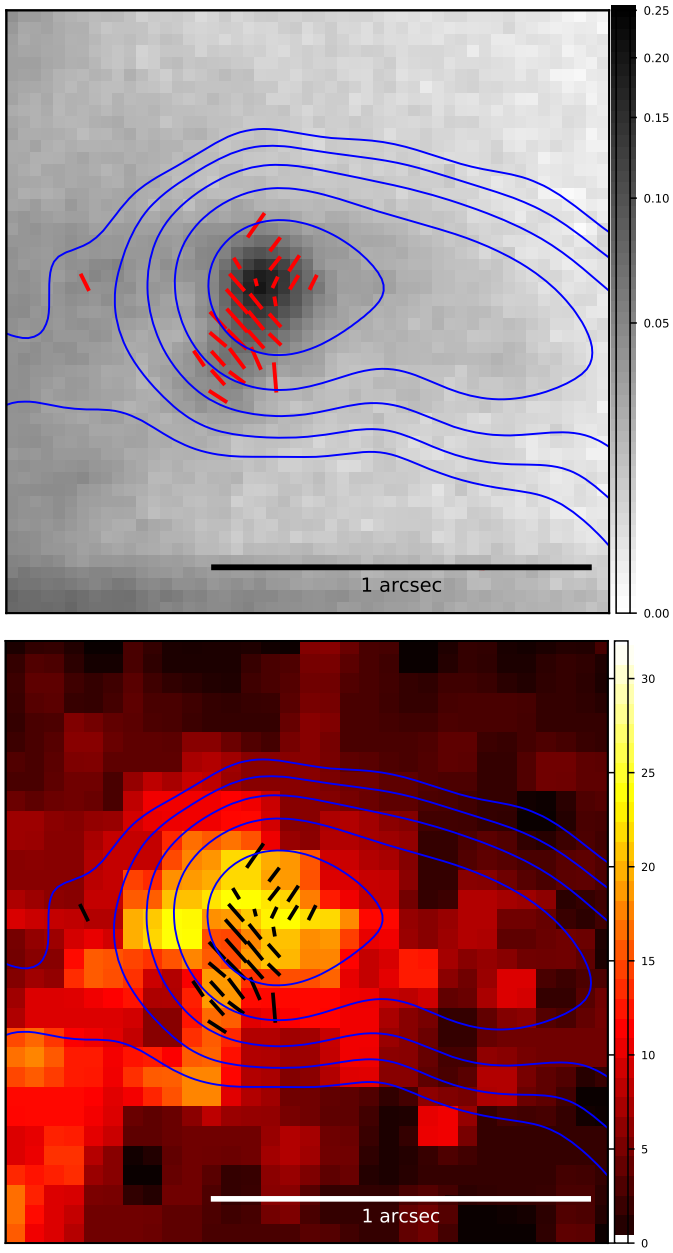

Figure 6.14: Brightest optical–X-ray region (Knot B) of 1150+497, with 1.66 GHz MERLIN radio contours overlaid. *Top*: Optical *HST*/ACS+F606W *Stokes I* image, with optical polarization E-field vectors overlaid (SNR > 4.0, in red). These E-field vectors show the orientation of the plane of linear polarization, with their lengths being proportional to the degree of polarization, scaled such that 0.2 arcsec = 100% polarization. The inferred magnetic field direction is perpendicular to the plotted E-field vectors. *Bottom*: *Chandra* ACIS-S X-ray image (0.3–7 keV) with the same optical E-vectors overlaid (in black).

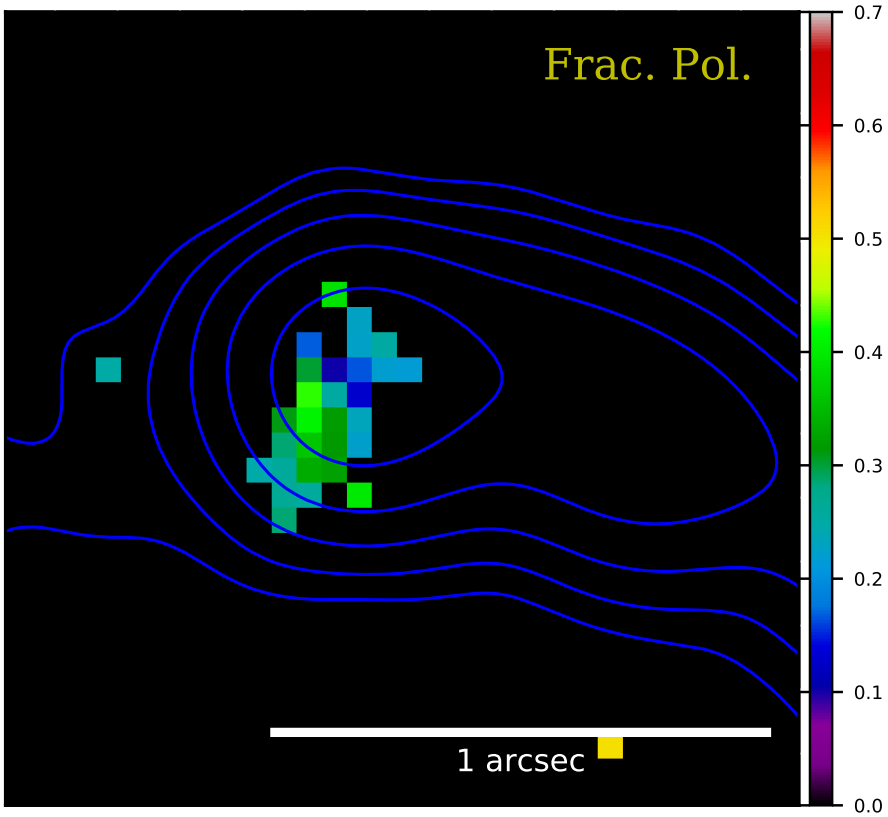

Figure 6.15: Showing the optical linear fractional polarization per pixel (where polarization SNR > 4.0) of the brightest optical–X-ray region (Knot B) of the 1150+497 jet, with 1.66 GHz MERLIN radio contours overlaid.

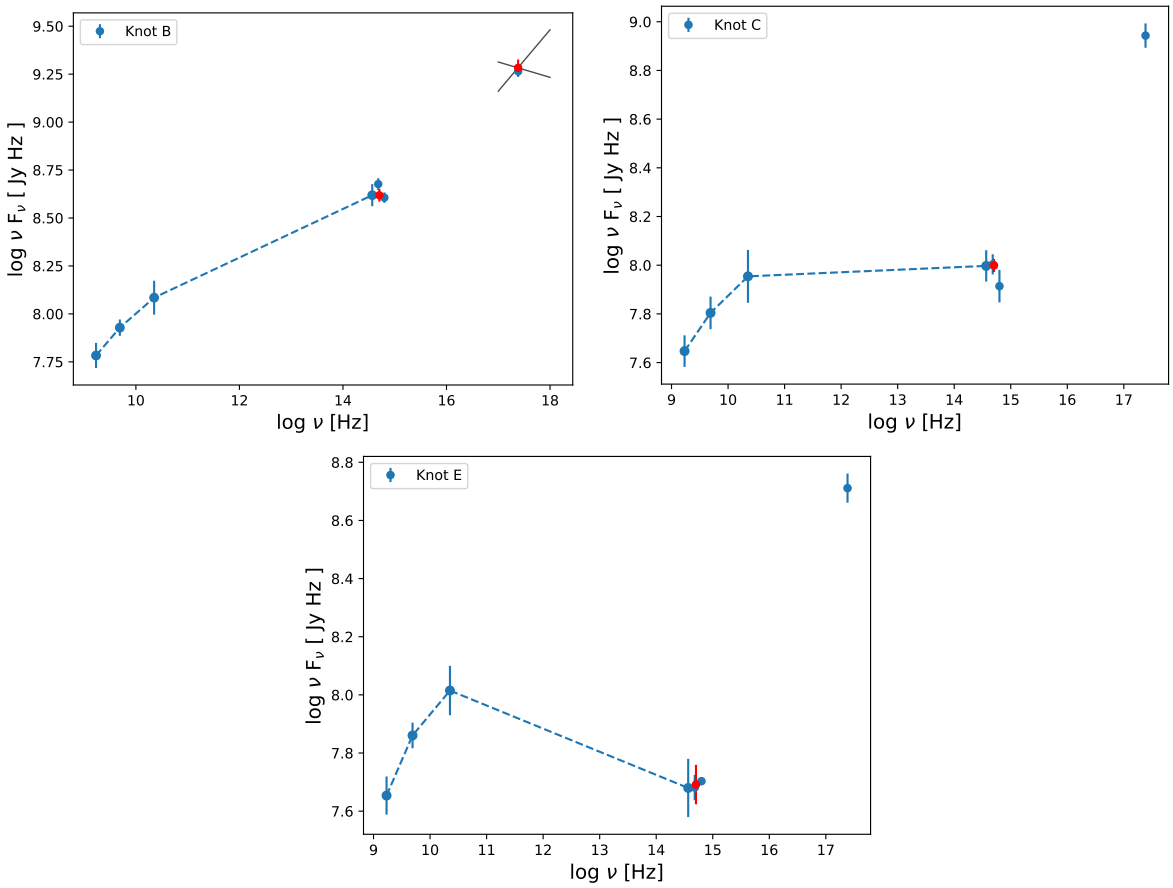

Figure 6.16: Broadband SED plots of the 1150+497 jet regions which have significant optical–X-ray flux. Flux points in blue are referenced from Sambruna et al. (2006a); those in red are new measurements from *HST*/ACS+F606W *Stokes I* with values listed in Table 6.3, with *Chandra* X-ray (1 keV) flux and spectral index (90% uncertainties, Table 5.1) shown for Knot B. Radio-IR fluxes have been naively connected between associated data points of the first synchrotron component, this is not meant to represent the actual shape of the SED component. Knot B exhibits significant linear polarization with high SNR.

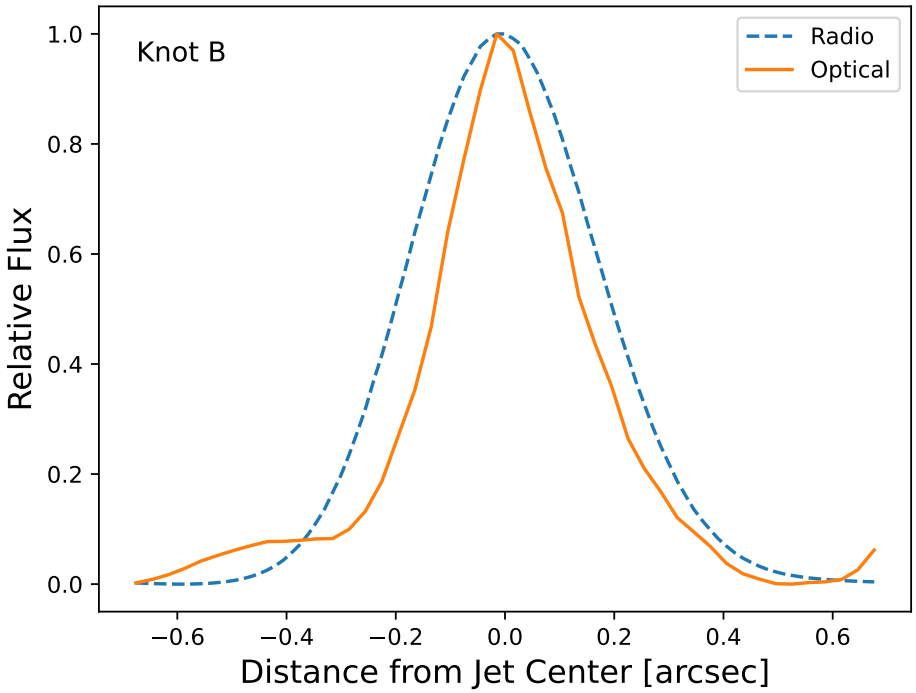

Figure 6.17: 1150+497: Relative flux profile of Knot B in the direction perpendicular to the jet, with fluxes from 1.66 GHz MERLIN radio and *HST*/ACS+F606W optical (smoothed) images. An emission profile that is narrower in the optical and/or X-ray than the radio could be evidence for the spine-sheath model of jet structure.

Chapter 7

Conclusion & Future Work

7.1 Summary

We have analyzed the optical polarization of three FR II quasar jets and compared their morphology with that of the radio and X-ray. First we will summarize the findings for each jet, and then the project as a whole.

3C 273:

- We find a high degree of optical linear polarization in every jet knot, from ∼10% up to ∼30%+.
- Three knots (A, B1, and B2) are shown to lie on the spectral energy component that connects to the X-rays. All three knots are highly polarized, which is a strong indication of a synchrotron origin for the high-energy emission in these regions.
- All knots (except H3) exhibit the same pattern of having a polarization minimum that coincides with peak flux in all bands.

- A low-polarization channel runs through the core of the jet from just downstream of Knot B3 to the flux maximum of D1. This may be an indication of a faster-moving spine, as the observed polarization is affected by relativistic beaming.

- All jet knots are shown to be narrower in the optical than in the radio, favoring a spine-sheath model of jet structure as discussed in §1.5.1.

- Most of the knots show the pattern of having their highest polarization values along the edges, again consistent with a spine-sheath model.

- The optical and radio polarization maps have a large mismatch in Knot D2, with the optical exhibiting strong polarization and the radio showing almost none.

- The magnetic field direction becomes perpendicular to the jet at various points, most distinctly at B1 and D2.

PKS 0637–752:

- Strong optical linear polarization measured in all optical knots, though only two with sufficient SNR to be confident in. Knot WK 8.9 exhibits P $\approx$ 33% with a high SNR.

- We detect no significant X-ray flux or spectral index variability in the one knot (WK 7.8) for which we have a preliminary estimate.

- Optical knots are seen to be significantly narrower than in the radio, favoring a spine-sheath model of jet structure as discussed in §1.5.1.

- The inferred magnetic field direction is consistently parallel with the jet through all optical knots.

- The jet exhibits a large bend downstream of Knot WK 9.7, after which no optical or X-ray flux is detected. No indication of the bend is shown in our polarization map.

1150+497:

- Significant optical linear polarization is measured in the knots of the 1150+497 jet – notably the sub-region of Knot B with P $\gtrsim$ 30% fractional polarization.
- We detect no significant X-ray flux or spectral index variability in the one knot (Knot B) for which we have a preliminary estimate.
- The polarization map of Knot B exhibits a complex morphology that is characteristic of an oblique shock at the site of a bend in the jet.
- The magnetic field direction rotates at Knot B to stay parallel after the bend.

7.2 Conclusion

We find the optically-bright knots in all three jets to be significantly polarized, with sub-regions of most knots exhibiting fractional polarization of P $\gtrsim$ 30%. This is strong evidence for a synchrotron source of radiation within these jets as an explanation for the optical emission.

Additionally, the fractional polarization maps we have made allow us to view the magnetic field structure of FR II jet knots at a much higher resolution than that was used for the only example of FR II jet polarimetry to date (PKS 1136−135, shown previously in Figure 2.4).

For the 3C 273 jet, there remains little doubt that the high-energy emission in Knots A, B1, and B2 are due to a separate population of accelerated electrons emitting high-

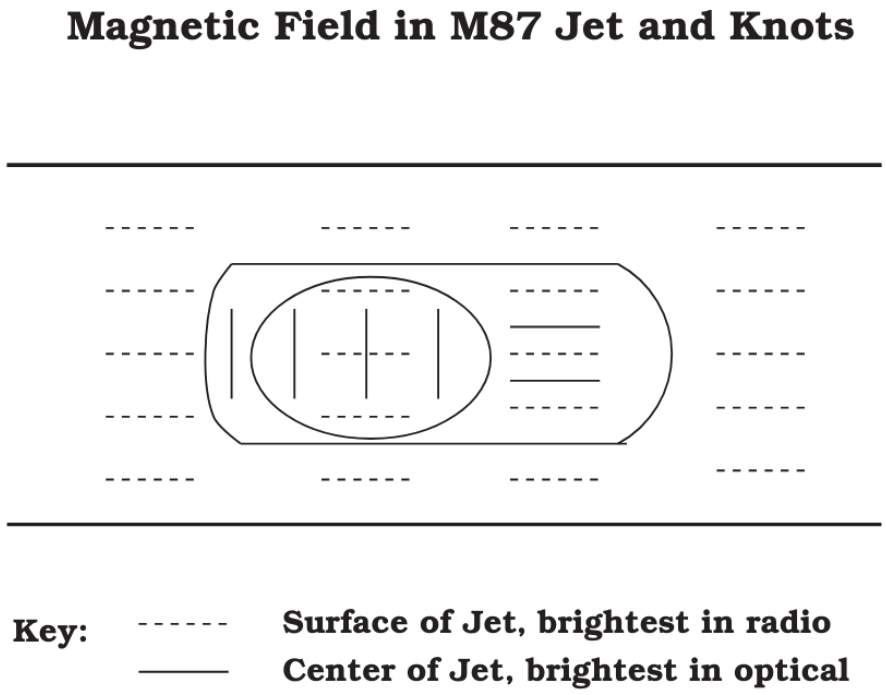

Figure 7.1: Structure of a jet knot as proposed for the M87 jet in Perlman et al. (1999). The solid and dashed lines represent the magnetic field directions in the inner spine and outer sheath of the jet, respectively. Observed polarization would be approximately zero at the maximum of knots, where perpendicular vectors are superposed. Figure taken from Boettcher et al. (2012).

energy synchrotron radiation. Our detection of strong linear polarization on the high-energy spectral component is definitive, as there is no other reasonable explanation given the known parameters of these jets or of non-thermal radiation processes. Other knots in the jet show significant differences between the optical and radio polarization, indicating a separate population of electrons responsible for the emission. This may be indicative of separate particle acceleration regions, and/or may be related to the proposed spine-sheath model of jet structure (discussed in §1.5.1).

7.2.1 Implications for the Spine-Sheath Model

Our observations of the jets of 3C 273, PKS 0637−752, and 1150+497 provide strong evidence for the spine-sheath model of jet structure and the high SNR and resolution allow us for the first time to compare the polarization structure of FR II knots with those of published FR I jets.

In the most well-studied FR I case of M87, Perlman & Wilson (2005) demonstrated a strong anti-correction between the X-ray peak flux and the optical fractional polarization in the jet knots (i.e., the magnetic field structure is least-ordered at the location of peak X-ray flux). Their interpretation is that the location of X-ray peak flux coincides with the location of shocks that accelerate electrons (and thus emit X-rays via synchrotron) and alter the magnetic field direction. Figure 7.1 shows the schematic for this model. In these shock regions (located in the spine of the jet), the magnetic field becomes roughly perpendicular to the jet. From our view, the overlap of the perpendicular fields in the sheath and the spine would overlap and cancel each other out, resulting in ∼zero polarization measured in these areas.

We see this same pattern of low or no observed polarization coinciding with the peak optical and/or X-ray flux in knots in each of our FR II jets, something that was not seen in PKS 1136−135, though with some interesting differences from that of M87. For example, Knot WK 7.8 in PKS 0637−752 shows the minimum polarization to be just upstream of the peak X-ray flux (Figure 6.9), and coinciding more with the optical – this may be indicative of particle acceleration located in different layers of the jet. Likewise many of the knots in 3C 273 show no measurable polarization at the location of the peak optical flux (e.g. Knots C1, C2, and D1). We interpret this general anti-correlation in the same way as the FR I cases, indicative of a spine-sheath structure within the jet with superposed perpendicular differences in the magnetic field directions at the location of particle acceleration sites. Evidence for the spine-sheath

structure of the 3C 273 jet was also shown by comparison of the deconvolved X-ray and radio morphologies in Marchenko et al. (2017), see Figure 1.6.

It remains an open question why this polarization anti-correlation does not match precisely with the peak X-ray flux in some of the observed knots, but does in others. If magnetic reconnection is a significant factor in particle acceleration in FR II jet knots, we lack the resolution to observe it.

7.3 Future Work

The main task that remains as future work for this project is a more complete analysis of our *Chandra* X-ray data. We intend to measure flux and model the spectra of each of the jet regions in PKS 0637−752 and 1150+497. We also intend to do an analysis of the X-ray variability over time. Observations of the PKS 0637−752 jet using *Chandra* go back to the first calibration images taken in 1999, and observations of 1150+497 go as far back as 2000. Given this significant period of time, there is a chance of finding X-ray flux and/or spectral index variability between the first observations and our new data. We will look for variability between all jet regions in multiple X-ray energy bands. Recently, our collaborator Meyer et al. (2023) recently published a study on X-ray variability for a sample of 53 jets.

We also intend to perform more robust SED model fitting, especially with Knots B1 and B2 of the 3C 273 jet.

7.3.1 PKS 1136-135

We also have new *Chandra* X-ray observations of the PKS 1136−135 jet that were acquired between March 2021 and June 2022. We intend to perform the same task as above, measuring the X-ray flux and spectral index for each observed jet knot and

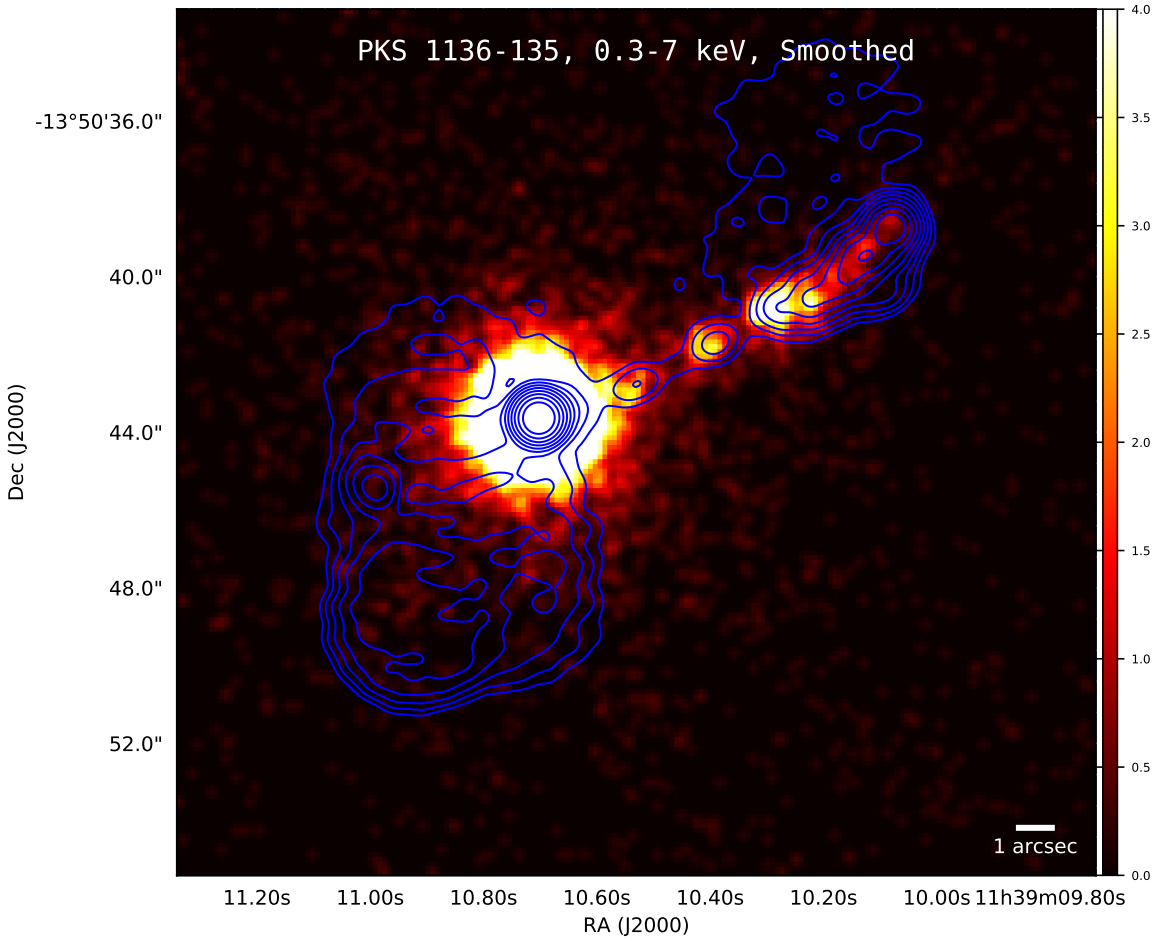

Figure 7.2: New *Chandra* X-ray (0.3 – 7 keV) image of the nucleus and approaching jet of PKS 1136−135, made using our new observations. PKS 1136−135 is the one FR II jet for which high-quality optical polarimetry had previously been performed (Cara et al., 2013), prior to this project.

checking for variability from past observations. The previous *Chandra* observations go back to 2003, so again there is a significant chance of X-ray variability between these epochs. The new data has already been reduced and is ready for science (Figure 7.2). The PKS 1136−135 jet was the first FR II jet for which high-SNR *HST* polarimetry was performed (Cara et al., 2013), and so we also intend to compare the X-ray flux morphology with that of the polarized optical emission, as we have done in this project.

7.3.2 3C 111

Previously, we acquired and analyzed new observations with in the infrared, ultraviolet, and X-rays using *HST* and *Chandra* of the large-scale jet of 3C 111 (Clautice et al., 2016). In that study, we compared the multiwavelength morphology with interesting results showing an offset between the flux maxima between bands in at least one knot, interpreted to be a signature of a high-energy synchrotron component in the SED. We also measured the flux of each knot in all bands and the X-ray spectral index for each jet region. We found a possible detection of the counter-jet lobe in the X-rays. This project was also the basis of my Master's thesis.

On the basis of that study, we were awarded additional observations of the 3C 111 jet, including 180 ks of *Chandra*, 8 orbits of *HST*, and 100 ks of *NuSTAR* time. We believe these observations will give us significantly better SNR in the fainter jet regions and allow us to probe the possible X-ray emission in the counter-jet lobe. Figure 7.3 shows an X-ray science image made from our new *Chandra* observations.

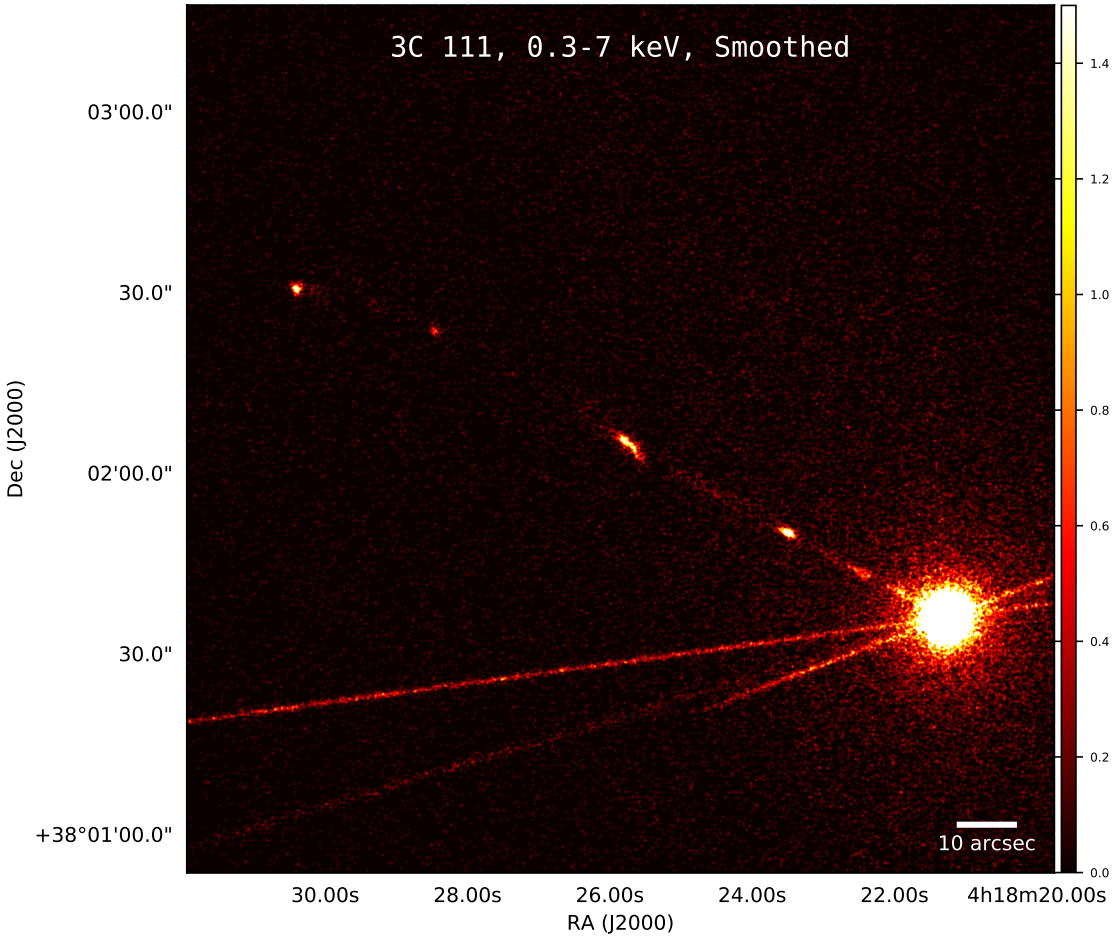

Figure 7.3: New *Chandra* X-ray (0.3 – 7 keV) image of the nucleus and approaching jet of 3C 111, made using our new observations. We previously studied the 3C 111 jet using *HST* and *Chandra* observations (Clautice et al., 2016), and have acquired new observations in multiple bands.

Bibliography

Anderson, J. & Ryon, J., *Improving the Pixel-Based CTE-correction Model for ACS/WFC*, Space Telescope Instrument Science Report ACS 2018-04, 2018

Arnaud, K., Smith, R., & Siemiginowska, A., *Handbook of X-ray Astronomy*, 2011

Astropy Collaboration, Robitaille, T. P., Tollerud, E. J., et al., *Astropy: A community Python package for astronomy*, Astronomy & Astrophysics, 2013, 558, A33

Avachat, S. S., Perlman, E. S., Adams, S. C., et al., *Multi-wavelength Polarimetry and Spectral Study of the M87 Jet During 2002-2008*, The Astrophysical Journal, 2016, 832, 3

Balbus, S. A. & Hawley, J. F., *A powerful local shear instability in weakly magnetized disks. I - Linear analysis. II - Nonlinear evolution*, The Astrophysical Journal, 1991, 376, 214–233

Bartel, N., Sorathia, B., Bietenholz, M. F., et al., *The Nuclear Jet and Counterjet Region of the Radio Galaxy Cygnus A*, Proceedings of the National Academy of Science, 1995, 92, 25, 11371–11373

Begelman, M. C., Blandford, R. D., & Rees, M. J., *Theory of extragalactic radio sources*, Reviews of Modern Physics, 1984, 56, 2, 255–351

Blandford, R., Meier, D., & Readhead, A., *Relativistic Jets from Active Galactic Nuclei*, Annual Review of Astronomy & Astrophysics, 2019, 57, 467–509

Blandford, R. D. & Payne, D. G., *Hydromagnetic flows from accretion discs and the production of radio jets*, Monthly Notices of the Royal Astronomical Society, 1982, 199, 883–903

Blandford, R. D. & Znajek, R. L., *Electromagnetic extraction of energy from Kerr black holes*, Monthly Notices of the Royal Astronomical Society, 1977, 179, 433–456

Blundell, K. M. & Alexander, P., *Spectral-index asymmetries in radio galaxies: The effects of projection and light traveltime*, Monthly Notices of the Royal Astronomical Society, 1994, 267, 241–246

Boccardi, B., Krichbaum, T. P., Ros, E., & Zensus, J. A., *Radio observations of active galactic nuclei with mm-VLBI*, , 2017, 25, 1, 4

Boettcher, M., Harris, D. E., & Krawczynski, H., *Relativistic Jets from Active Galactic Nuclei*, 2012

Bohlin, R. C., *Perfecting the Photometric Calibration of the ACS CCD Cameras*, The Astronomical Journal, 2016, 152, 3, 60

Bradt, H., *Astrophysics Processes*, 2014

Breiding, P., Meyer, E. T., Georganopoulos, M., et al., *Fermi Non-detections of Four X-Ray Jet Sources and Implications for the IC/CMB Mechanism*, The Astrophysical Journal, 2017, 849, 95

Breiding, P., Meyer, E. T., Georganopoulos, M., et al., *A multiwavelength study of multiple spectral component jets in AGN: testing the IC/CMB model for the large-scale-jet X-ray emission*, Monthly Notices of the Royal Astronomical Society, 2023, 518, 3, 3222–3250

Brenneman, L. W. & Reynolds, C. S., *Constraining Black Hole Spin via X-Ray Spectroscopy*, The Astrophysical Journal, 2006, 652, 1028–1043

Cara, M., Perlman, E. S., Uchiyama, Y., et al., *Polarimetry and the High-energy Emission Mechanisms in Quasar Jets: The Case of PKS 1136-135*, The Astrophysical Journal, 2013, 773, 186

Cash, W., *Parameter estimation in astronomy through application of the likelihood ratio*, The Astrophysical Journal, 1979, 228, 939–947

Chandra team, *The Chandra Proposers' Observatory Guide, Version 17.0*, Chandra X-ray Center, Massachusetts, 2014, available at `cxc.harvard.edu/proposer/POG`

Chandra team, *ACIS QE Contamination*, Chandra X-ray Center, Massachusetts, 2015, available at `cxc.harvard.edu/ciao/why/acisqecontam.html`

Clarke, D., *Stellar Polarimetry*, 2010

Clautice, D., Perlman, E. S., Georganopoulos, M., et al., *The Spectacular Radio-near-IR-X-Ray Jet of 3C 111: The X-Ray Emission Mechanism and Jet Kinematics*, The Astrophysical Journal, 2016, 826, 109

Curtis, H. D., *Descriptions of 762 Nebulae and Clusters Photographed with the Crossley Reflector*, Publications of Lick Observatory, 1918, 13, 9–42

Dulwich, F., Worrall, D. M., Birkinshaw, M., et al., *The structure of the jet in 3C 15 from multiband polarimetry*, Monthly Notices of the Royal Astronomical Society, 2007, 374, 1216–1226

Dulwich, F., Worrall, D. M., Birkinshaw, M., et al., *The magnetic field and geometry of the oblique shock in the jet of 3C 346*, Monthly Notices of the Royal Astronomical Society, 2009, 398, 3, 1207–1216

Event Horizon Telescope Collaboration, Akiyama, K., Alberdi, A., et al., *First M87 Event Horizon Telescope Results. I. The Shadow of the Supermassive Black Hole*, Astrophysical Journal Letters, 2019, 875, 1, L1

Event Horizon Telescope Collaboration, Akiyama, K., Algaba, J. C., et al., *First M87 Event Horizon Telescope Results. VII. Polarization of the Ring*, Astrophysical Journal Letters, 2021, 910, 1, L12

Fanaroff, B. L. & Riley, J. M., *The morphology of extragalactic radio sources of high and low luminosity*, Monthly Notices of the Royal Astronomical Society, 1974, 167, 31P–36P

Freeman, P., Doe, S., & Siemiginowska, A., *Sherpa: a mission-independent data analysis application*, *Astronomical Data Analysis*, (edited by J.-L. Starck & F. D. Murtagh), *Proc. SPIE*, vol. 4477, 2001 76–87

Fruscione, A., McDowell, J. C., Allen, G. E., et al., *CIAO: Chandra's data analysis system*, *Society of Photo-Optical Instrumentation Engineers (SPIE) Conference Series*, *Proc. SPIE*, vol. 6270, 2006 62701V

Georganopoulos, M. & Kazanas, D., *Relativistic and Slowing Down: The Flow in the Hot Spots of Powerful Radio Galaxies and Quasars*, Astrophysical Journal Letters, 2003, 589, 1, L5–L8

Georganopoulos, M., Kazanas, D., Perlman, E., & Stecker, F. W., *Bulk Comptonization of the Cosmic Microwave Background by Extragalactic Jets as a Probe of Their Matter Content*, The Astrophysical Journal, 2005, 625, 2, 656–666

Georganopoulos, M., Meyer, E., & Perlman, E., *Recent Progress in Understanding the Large Scale Jets of Powerful Quasars*, Galaxies, 2016, 4, 65

Giroletti, M., Giovannini, G., Cotton, W. D., et al., *The jet of Markarian 501 from millions of Schwarzschild radii down to a few hundreds*, Astronomy & Astrophysics, 2008, 488, 3, 905–914

Gonzaga, S., Hack, W., Fruchter, A., & Mack, J., *The DrizzlePac Handbook*, Space Telescope Science Institute, Baltimore, 2012, available at `drizzlepac.stsci.edu`

Hardcastle, M. J., Birkinshaw, M., & Worrall, D. M., *Chandra observations of the X-ray jet in 3C 66B*, MNRAS, 2001, 326, 1499–1507

Hardcastle, M. J., Lenc, E., Birkinshaw, M., et al., *Deep Chandra observations of Pictor A*, Monthly Notices of the Royal Astronomical Society, 2016, 455, 3526–3545

Harris, D. E. & Krawczynski, H., *X-Ray Emission from Extragalactic Jets*, Annual Review of Astronomy & Astrophysics, 2006, 44, 463–506

Harris, D. E. & Krawczynski, H., *Constraints on the Nature of Jets from KPC Scale X-Ray Data*, *Revista Mexicana de Astronomia y Astrofisica, vol. 27*, *Revista Mexicana de Astronomia y Astrofisica, vol. 27*, vol. 27, 2007 188

Homan, D., Hovatta, T., Kovalev, Y., et al., *Constraints on Particles and Fields from Full Stokes Observations of AGN*, Galaxies, 2018, 6, 1, 17

Homan, D. C., Lister, M. L., Kovalev, Y. Y., et al., *MOJAVE. XII. Acceleration and Collimation of Blazar Jets on Parsec Scales*, The Astrophysical Journal, 2015, 798, 2, 134

Howell, S. B., *Two-dimensional aperture photometry - Signal-to-noise ratio of point-source observations and optimal data-extraction techniques*, Publications of the Society of the Pacific, 1989, 101, 616–622

Howell, S. B., *Handbook of CCD Astronomy*, 2006

Howell, S. B., Koehn, B., Bowell, E., & Hoffman, M., *Detection and Measurement of Poorly Sampled Point Sources Imaged With 2-D Array*, The Astronomical Journal, 1996, 112, 1302

Jester, S., Harris, D. E., Marshall, H. L., & Meisenheimer, K., *New Chandra Observations of the Jet in 3C 273. I. Softer X-Ray than Radio Spectra and the X-Ray Emission Mechanism*, The Astrophysical Journal, 2006, 648, 900–909

Jester, S., Meisenheimer, K., Martel, A. R., et al., *Hubble Space Telescope far-ultraviolet imaging of the jet in 3C273: a common emission component from optical to X-rays*, Monthly Notices of the Royal Astronomical Society, 2007, 380, 828–834

Jester, S., Röser, H.-J., Meisenheimer, K., & Perley, R., *The radio-ultraviolet spectral energy distribution of the jet in 3C 273*, Astronomy & Astrophysics, 2005, 431, 477–502

Jiang, L., Fan, X., Ivezić, Ž., et al., *The Radio-Loud Fraction of Quasars is a Strong Function of Redshift and Optical Luminosity*, The Astrophysical Journal, 2007, 656, 680–690

Kellermann, K. I., Sramek, R., Schmidt, M., et al., *VLA observations of objects in the Palomar Bright Quasar Survey*, The Astronomical Journal, 1989, 98, 1195–1207

Kim, J. Y., Krichbaum, T. P., Lu, R. S., et al., *The limb-brightened jet of M87 down to the 7 Schwarzschild radii scale*, Astronomy & Astrophysics, 2018, 616, A188

Koide, S. & Arai, K., *Energy Extraction from a Rotating Black Hole by Magnetic Reconnection in the Ergosphere*, The Astrophysical Journal, 2008, 682, 2, 1124–1133

Konar, C., Jamrozy, M., Saikia, D. J., & Machalski, J., *A multifrequency study of giant radio sources - I. Low-frequency Giant Metrewave Radio Telescope observations of selected sources*, Monthly Notices of the Royal Astronomical Society, 2008, 383, 525–538

Kovalev, Y. Y., Lister, M. L., Homan, D. C., & Kellermann, K. I., *The Inner Jet of the Radio Galaxy M87*, Astrophysical Journal Letters, 2007, 668, 1, L27–L30

Krawczynski, H., *The Polarization Properties of Inverse Compton Emission and Implications for Blazar Observations with the GEMS X-Ray Polarimeter*, The Astrophysical Journal, 2012, 744, 30

Krichbaum, T. P., Graham, D. A., Bremer, M., et al., *Sub-Milliarcsecond Imaging of Sgr A* and M 87*, Journal of Physics Conference Series, 2006, 54, 328–334

Krist, J. E., Hook, R. N., & Stoehr, F., *20 years of Hubble Space Telescope optical modeling using Tiny Tim*, *Optical Modeling and Performance Predictions V*, *Proc. SPIE*, vol. 8127, 2011 81270J

Krtička, J., Kurfürst, P., & Krtičková, I., *Magnetorotational instability in decretion disks of critically rotating stars and the outer structure of Be and Be/X-ray disks*, Astronomy & Astrophysics, 2015, 573, A20

Lauer, T. R., Ajhar, E. A., Byun, Y.-I., et al., *The Centers of Early-Type Galaxies with HST.I.An Observational Survey*, The Astronomical Journal, 1995, 110, 2622

Legg, M. P. C. & Westfold, K. C., *Elliptic Polarization of Synchrotron Radiation*, The Astrophysical Journal, 1968, 154, 499

Lemoine, M., Pelletier, G., & Revenu, B., *On the Efficiency of Fermi Acceleration at Relativistic Shocks*, Astrophysical Journal Letters, 2006, 645, 2, L129–L132

Li, J., Kastner, J. H., Prigozhin, G. Y., et al., *Chandra ACIS Subpixel Event Repositioning: Further Refinements and Comparison between Backside- and Frontside-illuminated X-Ray CCDs*, The Astrophysical Journal, 2004, 610, 1204–1212

Lister, M. L., Cohen, M. H., Homan, D. C., et al., *MOJAVE: Monitoring of Jets in Active Galactic Nuclei with VLBA Experiments. VI. Kinematics Analysis of a Complete Sample of Blazar Jets*, The Astronomical Journal, 2009, 138, 1874-1892

Lister, M. L., Homan, D. C., Hovatta, T., et al., *MOJAVE. XVII. Jet Kinematics and Parent Population Properties of Relativistically Beamed Radio-loud Blazars*, The Astrophysical Journal, 2019, 874, 1, 43

Lister, M. L. & Marscher, A. P., *Statistical Effects of Doppler Beaming and Malmquist Bias on Flux-limited Samples of Compact Radio Sources*, The Astrophysical Journal, 1997, 476, 572–588

Longair, M. S. & Riley, J. M., *Statistical evidence on the dynamical evolution of extended radio sources*, Monthly Notices of the Royal Astronomical Society, 1979, 188, 625–635

Lovell, J. E. J., Tingay, S. J., Piner, B. G., et al., *VSOP and ATCA Observations of PKS 0637-752*, *Astrophysical Phenomena Revealed by Space VLBI*, (edited by H. Hirabayashi, P. G. Edwards, & D. W. Murphy), 2000 215–218

Lu, R.-S., Asada, K., Krichbaum, T. P., et al., *A ring-like accretion structure in M87 connecting its black hole and jet*, Nature, 2023, 616, 7958, 686–690

Lucas, R. et al., *ACS Data Handbook*, Space Telescope Science Institute, Baltimore, 2021, available at `https://hst-docs.stsci.edu/acsdhb/`

Marchenko, V., Harris, D. E., Ostrowski, M., et al., *Novel Analysis of the Multiwavelength Structure of the Relativistic Jet in Quasar 3C 273*, The Astrophysical Journal, 2017, 844, 1, 11

Marshall, H. L., Miller, B. P., Davis, D. S., et al., *A High-Resolution X-Ray Image of the Jet in M87*, The Astrophysical Journal, 2002, 564, 2, 683–687

Marshall, H. L., Schwartz, D. A., Lovell, J. E. J., et al., *A Chandra Survey of Quasar Jets: First Results*, The Astrophysical Journal, Supplement, 2005, 156, 13–33

Mehta, K. T., Georganopoulos, M., Perlman, E. S., et al., *Hubble Space Telescope Observations of the Quasar PKS 0637-752: Equipartition Electron-Proton Jet from the Most Complete Spectral Coverage to Date*, The Astrophysical Journal, 2009, 690, 1706–1714

Meier, D. L., *A Magnetically Switched, Rotating Black Hole Model for the Production of Extragalactic Radio Jets and the Fanaroff and Riley Class Division*, The Astrophysical Journal, 1999, 522, 753–766

Meier, D. L., *The formation of relativistic cosmic jets*, *Jets at All Scales*, (edited by G. E. Romero, R. A. Sunyaev, & T. Belloni), *IAU Symposium*, vol. 275, 2011 13–23

Meisenheimer, K. & Heavens, A. F., *Particle acceleration in the hotspot of the jet of quasar 3C273*, Nature, 1986, 323, 6087, 419–422

Meyer, E. T. & Georganopoulos, M., *Fermi Rules Out the Inverse Compton/CMB Model for the Large-scale Jet X-Ray Emission of 3C 273*, Astrophysical Journal Letters, 2014, 780, L27

Meyer, E. T., Georganopoulos, M., Sparks, W. B., et al., *Ruling out IC/CMB X-rays in PKS 0637-752 and the Implications for TeV Emission from Large-scale Quasar Jets*, The Astrophysical Journal, 2015, 805, 154

Meyer, E. T., Shaik, A., Tang, Y., et al., *Variability of extragalactic X-ray jets on kiloparsec scales*, Nature Astronomy, 2023, 7, 967–975

Meyer, E. T., Sparks, W. B., Georganopoulos, M., et al., *An HST Proper-motion Study of the Large-scale Jet of 3C273*, The Astrophysical Journal, 2016, 818, 195

Moderski, R., Sikora, M., & Lasota, J.-P., *On the spin paradigm and the radio dichotomy of quasars*, Monthly Notices of the Royal Astronomical Society, 1998, 301, 142–148

Mukherjee, D., Bodo, G., Mignone, A., et al., *Simulating the dynamics and non-thermal emission of relativistic magnetized jets I. Dynamics*, Monthly Notices of the Royal Astronomical Society, 2020, 499, 1, 681–701

Naghizadeh-Khouei, J. & Clarke, D., *On the statistical behaviour of the position angle of linear polarization*, Astronomy & Astrophysics, 1993, 274, 968

Narayan, R. & Quataert, E., *Black Hole Accretion*, Science, 2005, 307, 5706, 77–80

Perley, R. A. & Meisenheimer, K., *High-Fidelity VLA Imaging of the Radio Structure of 3C273*, ArXiv e-prints, 2016

Perley, R. A. & Meisenheimer, K., *High-fidelity VLA imaging of the radio structure of 3C 273*, Astronomy & Astrophysics, 2017, 601, A35

Perlman, E. S., Biretta, J. A., Sparks, W. B., et al., *The Optical-Near-Infrared Spectrum of the M87 Jet from Hubble Space Telescope Observations*, The Astrophysical Journal, 2001, 551, 1, 206–222

Perlman, E. S., Biretta, J. A., Zhou, F., et al., *Optical and Radio Polarimetry of the M87 Jet at 0.2" Resolution*, The Astronomical Journal, 1999, 117, 5, 2185–2198

Perlman, E. S., Clautice, D., Avachat, S., et al., *Unraveling the Physics of Quasar Jets: Optical Polarimetry and Implications for the X-ray Emission Process*, Galaxies, 2020, 8, 4, 71

Perlman, E. S., Padgett, C. A., Georganopoulos, M., et al., *Optical Polarimetry of the Jets of Nearby Radio Galaxies. I. The Data*, The Astrophysical Journal, 2006, 651, 2, 735–748

Perlman, E. S., Padgett, C. A., Georganopoulos, M., et al., *A Multi-Wavelength Spectral and Polarimetric Study of the Jet of 3C 264*, The Astrophysical Journal, 2010, 708, 1, 171–187

Perlman, E. S. & Wilson, A. S., *The X-Ray Emissions from the M87 Jet: Diagnostics and Physical Interpretation*, The Astrophysical Journal, 2005, 627, 1, 140–155

Perucho, M. & Martí, J. M., *A numerical simulation of the evolution and fate of a Fanaroff-Riley type I jet. The case of 3C 31*, Monthly Notices of the Royal Astronomical Society, 2007, 382, 526–542

Peterson, B. M., *An Introduction to Active Galactic Nuclei*, 1997

Punsly, B. & Coroniti, F. V., *Ergosphere-driven Winds*, The Astrophysical Journal, 1990a, 354, 583

Punsly, B. & Coroniti, F. V., *Relativistic Winds from Pulsar and Black Hole Magnetospheres*, The Astrophysical Journal, 1990b, 350, 518

Rees, M. J., *Appearance of Relativistically Expanding Radio Sources*, Nature, 1966, 211, 468–470

Roeser, H.-J. & Meisenheimer, K., *The synchrotron light from the jet of 3C 273*, Astronomy & Astrophysics, 1991, 252, 458–474

Rybicki, G. B. & Lightman, A. P., *Radiative processes in astrophysics*, 1979

Ryle, M., Sir & Longair, M. S., *A possible method for investigating the evolution of radio galaxies*, Monthly Notices of the Royal Astronomical Society, 1967, 136, 123

Ryon, J. et al., *ACS Instrument Handbook*, Space Telescope Science Institute, Baltimore, 2021, available at `https://hst-docs.stsci.edu/acsihb/`

Sambruna, R. M., Gliozzi, M., Donato, D., et al., *Deep Chandra and Multicolor HST Follow-up of the Jets in Two Powerful Radio Quasars*, The Astrophysical Journal, 2006a, 641, 2, 717–731

Sambruna, R. M., Gliozzi, M., Tavecchio, F., et al., *The Jet-Disk Connection in AGNs: Chandra and XMM-Newton Observations of Three Powerful Radio-Loud Quasars*, The Astrophysical Journal, 2006b, 652, 1, 146–156

Schneider, P., *Extragalactic Astronomy and Cosmology*, 2006

Schwartz, D. A., Marshall, H. L., Lovell, J. E. J., et al., *Chandra Discovery of a 100 kiloparsec X-Ray Jet in PKS 0637-752*, Astrophysical Journal Letters, 2000, 540, L69

Serkowski, K., *Statistical Analysis of the Polarization and Reddening of the Double Cluster in Perseus*, , 1958, 8, 135

Sérsic, J. L., *Influence of the atmospheric and instrumental dispersion on the brightness distribution in a galaxy*, Boletin de la Asociacion Argentina de Astronomia La Plata Argentina, 1963, 6, 41–43

Shakura, N. I. & Sunyaev, R. A., *Black holes in binary systems. Observational appearance.*, Astronomy & Astrophysics, 1973, 24, 337–355

Sikora, M., Nalewajko, K., & Madejski, G. M., *On the significance of relativistically hot pairs in the jets of FR II radio galaxies*, Monthly Notices of the Royal Astronomical Society, 2020, 499, 3, 3749–3754

Sikora, M., Rutkowski, M., & Begelman, M. C., *A spine-sheath model for strong-line blazars*, Monthly Notices of the Royal Astronomical Society, 2016, 457, 2, 1352–1358

Sironi, L., Petropoulou, M., & Giannios, D., *Relativistic jets shine through shocks or magnetic reconnection?*, Monthly Notices of the Royal Astronomical Society, 2015, 450, 183–191

Sol, H., Pelletier, G., & Asseo, E., *Two-flow model for extragalactic radio jets.*, Monthly Notices of the Royal Astronomical Society, 1989, 237, 411–429

Tavecchio, F., Maraschi, L., Sambruna, R. M., & Urry, C. M., *The X-Ray Jet of PKS 0637-752: Inverse Compton Radiation from the Cosmic Microwave Background?*, Astrophysical Journal Letters, 2000, 544, L23–L26

Tchekhovskoy, A. & Bromberg, O., *Three-dimensional relativistic MHD simulations of active galactic nuclei jets: magnetic kink instability and Fanaroff-Riley dichotomy*, Monthly Notices of the Royal Astronomical Society, 2016, 461, L46–L50

Thomson, R. C., Mackay, C. D., & Wright, A. E., *Internal structure and polarization of the optical jet of the quasar 3C273*, Nature, 1993, 365, 133–135

Tout, C. A. & Pringle, J. E., *Can a disc dynamo generate large-scale magnetic fields?*, Monthly Notices of the Royal Astronomical Society, 1996, 281, 219–225

Uchiyama, Y., Urry, C. M., Cheung, C. C., et al., *Shedding New Light on the 3C 273 Jet with the Spitzer Space Telescope*, The Astrophysical Journal, 2006, 648, 910–921

Uchiyama, Y., Urry, C. M., Coppi, P., et al., *An Infrared Study of the Large-Scale Jet in Quasar PKS 1136-135*, The Astrophysical Journal, 2007, 661, 719–727

Vikhlinin, A., *Reducing ACIS Quiescent Background Using Very Faint Mode*, Chandra X-ray Center, Massachusetts, 2002, available at `cxc.harvard.edu/cal/Acis/Cal_prods/vfbkgrnd/index.html`

Wang, J., Fabbiano, G., Risaliti, G., et al., *A Deep Chandra ACIS Study of NGC 4151. I. The X-ray Morphology of the 3 kpc Diameter Circum-nuclear Region and Relation to the Cold Interstellar Medium*, The Astrophysical Journal, 2011, 729, 75

Wardle, J. F. C. & Kronberg, P. P., *The linear polarization of quasi-stellar radio sources at 3.71 and 11.1 centimeters.*, The Astrophysical Journal, 1974, 194, 249

Weisskopf, M. C., Aldcroft, T. L., Bautz, M., et al., *An Overview of the Performance of the Chandra X-ray Observatory*, Experimental Astronomy, 2003, 16, 1–68

Wilson, A. S. & Colbert, E. J. M., *The difference between radio-loud and radio-quiet active galaxies*, The Astrophysical Journal, 1995, 438, 62–71

Worrall, D. M., *The X-ray jets of active galaxies*, A&ARv, 2009, 17, 1–46

Xie, W., Lei, W.-H., Zou, Y.-C., et al., *A two-component jet model based on the Blandford-Znajek and Blandford-Payne processes*, Research in Astronomy and Astrophysics, 2012, 12, 817–828

Zweibel, E. G. & Yamada, M., *Magnetic Reconnection in Astrophysical and Laboratory Plasmas*, Annual Review of Astronomy & Astrophysics, 2009, 47, 291–332